



UNIVERSIDAD DE ANTIOQUIA  
FACULTAD DE CIENCIAS EXACTAS Y NATURALES  
INSTITUTO DE FÍSICA

# THE PLACE OF THE MILKY WAY AND ANDROMEDA IN THE COSMIC WEB

**Sebastian Bustamante Jaramillo**

Facultad de Ciencias Exactas y Naturales  
Instituto de Física

**Advisor:** Jaime E. Forero-Romero

**Co-advisor:** Jorge I. Zuluaga





UNIVERSIDAD DE ANTIOQUIA  
FACULTAD DE CIENCIAS EXACTAS Y NATURALES  
INSTITUTO DE FÍSICA

# THE PLACE OF THE MILKY WAY AND ANDROMEDA IN THE COSMIC WEB

**Sebastian Bustamante Jaramillo**

Facultad de Ciencias Exactas y Naturales  
Instituto de Física

**Advisor:** Jaime E. Forero-Romero

**Co-advisor:** Jorge I. Zuluaga

Student

Advisor

Co-advisor

Medellín, January 2014



*to my family, my girlfriend and my friends.*

*The place of the Milky Way and Andromeda in the cosmic web*

Author: Sebastian Bustamante

Advisor: Jaime E. Forero-Romero

Co-advisor: Jorge I. Zuluaga

In the next link it could be found updated information about this work and some topics related to it:

<https://github.com/sbustamante/Thesis>

Printed in Medellín, Colombia

First edition, january 2013

---

## Abstract

As it has been widely demonstrated from observations and cosmological simulations, the present universe harbours a complex large-scale structure of entangled filaments of clumped matter permeated by vast low-density regions. This structure is called cosmic web and is one of the mainly emergent features of the non-linear regime of the universe. Numerous studies have been performed aimed to quantify the effects of the cosmic web on different physical properties of systems like dark matter halos, galaxies and galaxy clusters. Some important correlations have already been found for some of those properties, such as the mass of the halos, the spin parameter and their shape. There is also a growing interest in studying the properties of the local group of galaxies (dominated gravitationally by the Milky Way and Andromeda galaxy) in a cosmological context as a test of the standard cosmological model.

Motivated to continue this line of research, the current work is pointed to study LG-like systems in a set of dark matter cosmological simulations in a cosmological context. It is used three constrained simulations (CLUES) aimed to mimic our local environment and an unconstrained simulation (Bolshoi) used for the statistic treatment. As one of the key proposals of this work is to introduce a new method for constructing LG-like systems in simulations by using the V-web scheme to classify the local environment in the constrained simulations. It is demonstrated that the LG-like sample constructed by this way is consistent and has biases in some physical properties with respect to the distribution of halos. Specially, it is found that unlike halos, which are formed in high-density regions, LG-like systems rather lie in low-density regions, like voids and sheets.



## **Agradecimientos**

Es bastante satisfactorio mirar en retrospectiva todo el proceso de formación que he recibido y darse cuenta que cada paso logrado ha contribuido de una u otra forma a culminar este logro. En especial, nada de esto hubiera sido posible sin el apoyo incondicional de mi familia, mi madre Gilma Jaramillo, mi padre Aníbal Bustamante y mi hermano Santiago Bustamante, a ellos muy especialmente va dedicado este trabajo.

Cito la frase de Isaac Newton, “Si he logrado ver más lejos, ha sido porque he subido a hombros de gigantes”. Con esto quiero aludir a todos los profesores que en algún grado contribuyeron a mi proceso de formación, especialmente Jaime Forero por permitirme trabajar en estos apasionantes temas, brindarme la oportunidad de realizar una pasantía que me ayudó enormemente en este proyecto, además por su infinita paciencia. Al profesor Jorge Zuluaga por su acompañamiento durante casi toda mi carrera y enseñarme la gran mayoría de mis conocimientos en programación. A Carlos Vera por introducirme en el fascinante mundo de la astrofísica y finalmente a los profesores Boris Rodríguez y Pablo Cuartas, que en un momento u otro de mi carrera aportaron valiosamente en este arduo proceso.

Quiero especialmente agradecer a mi novia Nataly Mateus por su apoyo permanente y acompañamiento, por su paciencia en los malos momentos y por escucharme y aportarme con ideas y correcciones de mi tesis. Con ella quiero compartir la alegría de culminar esta etapa y también

le dedico este trabajo. También agradezco a su familia por su gran apoyo y preocupación, por acogerme durante las maratónicas jornadas de estudio, que no fueron pocas.

Finalmente también dedico este trabajo a todos mis amigos, muy en especial aquellos de astronomía y física, por los momentos alegres que me han brindado y su preocupación en los malos momentos. Agradezco también a Cesar Uribe por escuchar tan pacientemente sobre temas de esta tesis y aportar con algunas ideas.

*Sinceramente,*

Sebastian Bustamante

February 2014

# Contents

<b>List of Figures</b>	<b>vii</b>
<b>1 Preliminaries</b>	<b>1</b>
1.1 Prehistory . . . . .	1
1.2 The Current Cosmology Picture . . . . .	4
1.3 Cosmological Observations . . . . .	8
<b>2 Theoretical Framework in Cosmology</b>	<b>11</b>
2.1 Isotropic and Homogeneous Universe . . . . .	11
2.1.1 Metric of Curved Spaces . . . . .	12
2.1.2 General Relativity and Friedmann's Equations . . . . .	16
2.1.3 Simple Solutions of the Universe . . . . .	18
2.2 Linear Regime of Structure Formation . . . . .	22
2.2.1 Newtonian Approximation . . . . .	23
2.2.2 Jeans Instability . . . . .	26
2.2.3 Statistical Properties and Transfer Function . . . . .	31
2.3 Non-Linear Regime of Structure Formation . . . . .	37
2.3.1 Zeldovich Approximation . . . . .	38
<b>3 Computational Methods in Cosmology</b>	<b>41</b>
3.1 N-body Simulations . . . . .	42
3.1.1 P-P Method . . . . .	43
3.1.2 PM Method . . . . .	44
3.1.3 P <sup>3</sup> M Method . . . . .	46

## CONTENTS

---

3.2	Types of Simulations . . . . .	48
3.2.1	Unconstrained Simulations (Bolshoi) . . . . .	49
3.2.2	Constrained Simulations (CLUES) . . . . .	51
3.3	Environment Characterization . . . . .	54
3.3.1	T-web Scheme . . . . .	54
3.3.2	V-web Scheme . . . . .	56
3.4	Detecting Halos and Defining the Samples . . . . .	58
3.4.1	FOF Method . . . . .	58
3.4.2	Definición de Muestras . . . . .	60
3.4.3	Método de Detección de Pares . . . . .	63
<b>4</b>	<b>El Entorno Cosmológico y el Grupo Local</b>	<b>65</b>
4.1	Propiedades de las Simulaciones . . . . .	65
4.1.1	Función de Masa de los Halos . . . . .	66
4.1.2	Distribución del Entorno Cosmológico . . . . .	68
4.2	Propiedades de la Muestra <i>CLG</i> . . . . .	73
4.2.1	Determinación del Entorno . . . . .	73
4.2.2	Masa de los <i>CLG</i> . . . . .	79
4.2.3	Distribuciones de Energía y Momentum Angular . . . . .	83
4.2.4	Alineación del Momentum Angular . . . . .	85
4.3	Conclusiones . . . . .	86
<b>Bibliography</b>		<b>89</b>

# List of Figures

1.1	William Herschel's model for our galaxy based upon a count of stars with the assumption of equal intrinsic luminosity. [14]. . . . .	2
1.2	Different geometries according to variations on Euclid's fifth postulate. . . . .	4
1.3	Cosmic background radiation. Taken from <a href="http://upload.wikimedia.org/wikipedia/commons/3/3c/I1c_9yr_moll4096.png">http://upload.wikimedia.org/wikipedia/commons/3/3c/I1c_9yr_moll4096.png</a> . . . . .	5
1.4	Local Group. Taken from <a href="http://commons.wikimedia.org/wiki/File:Local_Group.svg">http://commons.wikimedia.org/wiki/File:Local_Group.svg</a> . . . . .	7
1.5	Map of the large-scale universe according to the Sloan Digital Sky Survey. Taken from the official web page of the project <a href="http://www.sdss.org/">http://www.sdss.org/</a> . . . . .	9
2.1	Metric of a spherical surface. . . . .	12
2.2	Curved spaces according to the curvature parameter. . . . .	13
2.3	Different solutions of the universe according to the Friedmann's equations. . . . .	22
2.4	Evolution of the Jean mass for different stages of the universe. Coloured regions illustrate the typical mass range of some types of structures, since open stellar clusters to superclusters of galaxies. . . . .	29
2.5	Evolution of the normal modes of the density field. For the sake of the illustration, each solution has been normalized with respect to the initial conditions. . . . .	31
2.6	Initial distribution of perturbations for the density contrast field from the Gaussian distribution 2.57 and the Harrison-Zeldovich power spectrum $\sigma_k \propto k$ . . . . .	33

## LIST OF FIGURES

---

2.7	Transfer function for cold dark matter perturbations at the current epoch [26] (left panel). Comparison between the initial power spectrum, Harrison-Zeldovich spectrum and the processed power spectrum (right panel) . . . . .	36
2.8	Evolution of a dark matter numerical simulation in a comoving volume of $(40 \text{ Mpc}/h)^3$ , starting from a high homogeneity stage (upper left panel), until the present epoch with highly non-linear structures (lower right panel). Taken from <a href="http://www.astro.utu.fi/research/CosmoS/lss/lss_p1.shtml">http://www.astro.utu.fi/research/CosmoS/lss/lss_p1.shtml</a> . . . . .	37
2.9	Comparison of the evolution in non-linear regime between a N-body simulation (a) and the Zeldovich approximation (b). In both cases are used the same initial conditions. Taken from [26]. . . . .	39
3.1	Formulation of the N-body problem. . . . .	42
3.2	Illustrative diagram of the PM method. The map that is plotted over the distribution of particles corresponds to the density field evaluated in each cell of the grid. Dark cells corresponds to overdensity regions whereas white cells to lower values of the density field, which agrees with the amount of mass of the particles per cell. . . . .	44
3.3	Illustrative diagram of the P <sup>3</sup> M method. For the reference particle, shown in the center, interactions with distant particles is calculated through the PM method, whereas for close particles (gray and white regions), the interaction is calculated by using the PP method. . . . .	46
3.4	An illustrative example of the building of a tree code for a N-body simulation. Upper panels show the iterations for a 2D problem whereas lower panel illustrates the resultant tree built using each particle of the simulation.	47
3.5	Evolution of the Bolshoi simulation. It is illustrated the density field in a rectangular volume of $16 \text{ Mpc}/h$ of thick and $250 \text{ Mpc}/h$ of side for different stages of the evolution. $z = 9.5$ (upper left), $z = 3$ (upper right), $z = 1$ (lower left) y $z = 0$ (lower right). Taken from <a href="http://spectrum.ieee.org/aerospace/astrophysics/the-cosmological-supercomputer">http://spectrum.ieee.org/aerospace/astrophysics/the-cosmological-supercomputer</a>	50

---

## LIST OF FIGURES

3.6	Initial density and peculiar velocity field built by using constraints in order to reproduce the local environment at a scale of $160 h^{-1}$ Mpc. Some of the identified structures are: <i>Coma</i> , coma cluster, <i>PP</i> , Perseus-Pisces supercluster, <i>LS</i> , local supercluster, <i>GA</i> , the great attractor. The upper arrow indicates the scale of the peculiar velocities field as 1000 km/s. Taken from [22]. . . . .	51
3.7	Three constrained simulations of the CLUES project where it is possible to identify systems like the local group. It is illustrated the density field of each simulations along with the dark matter halos (black points), and the LG-like systems found (red points). . . . .	52
3.8	An example of a simulation of the CLUES project. In this figure it is shown the large-scale structures of the local universe and it can be appreciated clearly the most significant members of the Local Group. Taken from the official webpage of the project <a href="http://www.clues-project.org">http://www.clues-project.org</a> . . . . .	53
3.9	Classification scheme for the cosmological environment for both T-web and V-web schemes. The threshold value $\lambda_{th}$ is taken as free parameter. . . . .	56
3.10	It is illustrated for each one of the simulations (CLUES 1, CLUES 2, CLUES 3, Bolshoi) the difference between both classification schemes, T-web and V-web, and for different threshold values $\lambda_{th}$ (Black - Knot, Dark gray - Filament, Gray - Sheet, White - Vacuum). In the upper figures it is shown the visual impression obtained from the respective density fields ( $\log(\delta + 1)$ ), these impressions are used to calibrate the threshold value $\lambda_{th}$ . The resolution of the used grid in each simulation is approximately $1.0h^{-1}$ Mpc/cell and for each one it is performed a Gaussian softening of one cell size. The width of each slide is one cell. . . . .	57
3.11	Illustrative diagram of the FOF method. Gray circles around each particle represents the linking region and the red curve represents one of the bounded structures found by the method. . . . .	59
3.12	Halos detected by using the FOF scheme for one of the CLUES simulations. The color gradient indicates the deep respect to the $x$ axe, where black point are the nearest halos. . . . .	60

## LIST OF FIGURES

---

3.13 Entorno cosmológico a partir del esquema V-web (con $\lambda_{th} = 0.3$ ) para cada uno de los LG de las simulaciones CLUES, indicados por los puntos rojos. . . . .	62
3.14 Ilustración 2D del método para la detección de las muestras de pares. Distribución de halos de materia oscura (izquierda), definición de zonas (derecha). . . . .	64
4.1 Distribución espacial de los halos de materia oscura, reflejando la estructura de la red cósmica. El gradiente de color indica la profundidad respecto al eje $x$ , donde los halos negros son los más cercanos. . . . .	66
4.2 Funciones de masa integrada de halos de materia oscura (muestra GH) para cada simulación. . . . .	67
4.3 Distribución de los autovalores en el esquema V-web para cada una de las celdas de volumen (línea continua) y para los entornos de los halos de materia oscura en los catálogos FOF (línea discontinua). Las distribuciones están normalizadas tal que su área es la unidad. Resolución de $1.0h^{-1}$ Mpc/celda y suavizado Gaussiano de una celda. . . . .	68
4.4 Parámetro de densidad medio para diferentes tipos de regiones en función del valor umbral $\lambda_{th}$ (paneles izquierda). Fracciones de volumen normalizadas para diferentes tipos de regiones, también acorde al valor umbral $\lambda_{th}$ . . . . .	70
4.5 Comparación de la impresión visual obtenida con el método V-web para varios valores del parámetro $\lambda_{th}$ . Se usa el siguiente esquema de clasificación (Negro - Nudo, Gris oscuro - Filamento, Gris - Hoja, Blanco - Vacío). La resolución de cada malla es $1.0h^{-1}$ Mpc/celda, con un suavizado Gaussiano de una celda. El grosor de cada slide es de una celda. . . . .	71
4.6 Situación patológica respecto al entorno de los sistemas de pares de halos. . . . .	73
4.7 Comparación entre las distribuciones de los autovalores de la V-web para los dos halos en los sistemas de pares (muestras <i>LG</i> , <i>CLG</i> y <i>IP</i> ). . . . .	74

---

## LIST OF FIGURES

4.8	Distribuciones 2D del entorno cosmológico para diferentes muestras, $\lambda_1-\lambda_3$ (izquierda) y $\lambda_1-\lambda_2$ (derecha). El histograma de fondo, graficado en colores, corresponde a la distribución de entorno para todos los halos de Bolshoi (muestra <i>GH</i> ), su resolución es de $100 \times 100$ para el rango mostrado y están normalizados respecto a su área. Los puntos negros corresponden a la distribución de la muestra <i>IP</i> y finalmente los puntos blancos a la muestra <i>CLG</i> . . . . .	75
4.9	Fracciones de cantidad de objetos en diferentes regiones en función del valor umbral $\lambda_{th}$ . Para el caso de la muestra <i>GH</i> se cuentan número de Halos, mientras que para las muestras <i>IP</i> y <i>CLG</i> número de pares. . . . .	77
4.10	Histograma integrado del fraccional de anisotropía para las muestras de pares <i>IP</i> y <i>CLG</i> . . . . .	78
4.11	Funciones de distribución integrada para la masa total $M_A+M_B$ (izquierda) y la razón de las masas $M_B/M_A$ (derecha), de las muestras de pares en Bolshoi. . . . .	80
4.12	Diagrama de dispersión de los parámetros de masa definidos ( $M_{tot}, \chi$ ) para cada una de las muestras de pares. Las regiones cuadradas son construidas a partir del valor medio y la desviación estándar de la muestra del mismo color. La región gris en la parte inferior izquierda corresponde a un corte impuesto artificialmente con el rango mínimo de masa de los halos tomados $M_*$ para construir las muestras de pares. . . . .	81
4.13	Diagramas de dispersión para el fraccional de anisotropía respecto a los parámetros de masa. El mapa de fondo y las curvas de contorno corresponden a número de pares de la muestra <i>IP</i> . . . . .	82
4.14	Diagrama de dispersión para la energía total y el momentum angular orbital de los sistemas de pares. El mapa de fondo corresponde a la distribución de la muestra <i>P</i> , mientras las líneas de contorno a la distribución de la muestra <i>IP</i> , en ambos casos los valores corresponden al número de pares. . . . .	83
4.15	Diagramas de dispersión para el fraccional de anisotropía respecto a la energía y el momentum angular. El mapa de fondo y las curvas de contorno corresponden a número de pares de la muestra <i>IP</i> . . . . .	84

## **LIST OF FIGURES**

---

- 4.16 Histogramas integrados para el ángulo formado entre el momentum angular de los pares, el cual determina el plano orbital, y cada uno de los autovectores definidos por la V-web en el entorno cosmológico. Se realiza para cada las muestras de pares *CLG* y *IP*, mientras que los grupos locales de CLUES son ilustrados con las líneas rojas punteadas. . . . . 85

*“Equipped with his five senses, man explores the universe around him and calls the adventure Science”*

Edwin Hubble

CHAPTER

# 1

# Preliminaries

“What is our place in the cosmos?” This is one of the simpler and transcendental question that human beings have wondered from ancient times; furthermore, this, being powered by our innate curiosity, has led to a relatively understandable and structured picture of our Universe. Despite of that, this knowledge is very new regarding our whole history, so the astronomy can only be considered as a scientific rigorous discipline since the seventeenth century.

## 1.1 Prehistory

Almost in every scientific discipline, a significant theoretical development is accompanied by a technical and instrumental improvement. That is why at the beginning of the seventeenth century, Johannes Kepler could establish his three well-known empirical laws of the planetary movements based upon the very precise data of astronomical bodies compiled by Tycho Brahe. This event was very remarkable in the history of the astronomy since it was the first of many strikes against the well established anthropocentric notion of the cosmos. Although Kepler’s laws constituted the most crucial test to the Nicolaus Copernicus’s heliocentric model, it was only until 1685, when Isaac Newton formulated the law of universal gravitation (from which can be derived all the Kepler’s laws), when the astronomers could

## 1. PRELIMINARIES

---

count with enough powerful theoretical tools to start a depth and serious discussion about the real nature of our universe on scales bigger than the solar system, and thus inaugurating the *sciences of gravity* [26].

After the establishment of the law of universal gravitation, the next significant theoretical achievement in this area came in the centuries eighteenth and nineteenth with the development of classical mechanics, i.e. Hamiltonian and Lagrangian formalism, and powerful numerical tools. All those achievements propelled the study of key topics like the many body problem, chaotic phenomena, etc. Allowing a depth understanding of the dynamic of complex gravitational systems, such as planetary systems, star clusters, etc.

Parallel to the previous theoretical advances, on the observational branch was beginning to arise the idea of *island universe*, from which would evolve the concept of galaxy. All of this was powered by the development of the telescope, furthermore allowing understanding that galaxies are just a large collection of stars like our sun. It was also very remarkable the pioneer work of William Herschel, who tried to build a complete map of our galaxy determining distances from the assumption of stars with the same intrinsic luminosity and with the inverse square law for the intensity decay (see Figure 1.1). Although his results were very imprecise due to the incorrect assumption on which were based, the importance of his work lies on the recognition of some structure (disk-like) for our galaxy.

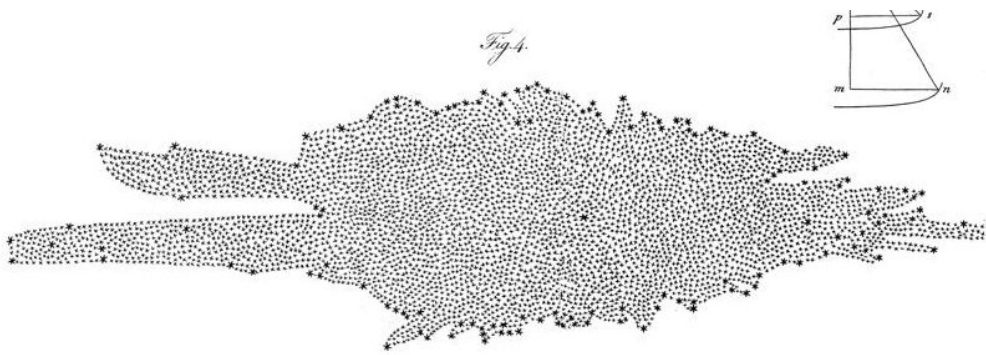


**Figure 1.1:** William Herschel's model for our galaxy based upon a count of stars with the assumption of equal intrinsic luminosity. [14].

## **1.1 Prehistory**

---

Another important observational question, that was emerging among scientists by that time, was the existence of *island universes* like ours. It was already well-known the existence of extended objects that do not fit to the definition of stars or planets, like nebulae, planetary disks and galaxies. Even, William Herschel and his son, John Herschel, contributed with the realization of a large (for the epoch) catalogue of extended bodies known as *Catalogue of Nebulae and Clusters of Stars* and a subsequent improved and expanded version finished by John Dreyer in 1888, *New General Catalogue of Nebulae and Clusters of Stars*, which together with *Index Catalogues* of 1895 and 1908 constitute a large collection of bodies widely used in current astronomy, referred with the abbreviations *NGC* and *IC* respectively [26]. Despite of those observational advances, the real nature of these objects was a complete mystery, specially if they lie within our own galaxy or are completely independent systems.

This question remained unsolved until the twentieth century, and together with the indetermination of the real size of the universe, were the two big issues treated on the well-known *Great Debate*, or also called the *Shapley-Curtis Debate*. In this important event in the history of astronomy, the astronomers Harlow Shapley and Herber Curtis discussed about these topics, giving, respectively, different arguments for and against if these objects are within our galaxy and if the Milky Way is our whole universe or not [4] [32]. Despite of that, their arguments were not very conclusive and the definitive solution to these issues had to wait until 1924, when Edwin Hubble measured the distance to Andromeda Galaxy (M31 or NGC 224) and demonstrated unquestionably the real extragalactic nature of this object, and in following years for other ones [18]. This achievement along with the observational verification of the expanding universe (also due to Hubble) were the beginning of the modern observational cosmology.

It also happened in the twentieth century a key event for the modern sciences of gravity, Albert Einstein formulated his theory of General Relativity [6], challenging and changing completely the previous conception of space and time and laying the foundation of current cosmology picture.

## 1. PRELIMINARIES

---

### 1.2 The Current Cosmology Picture

The theoretical basis on which are based the theory of general relativity began to arise with the zenith of non-euclidean geometries in the nineteenth century and the beginning of twentieth, when it was demonstrated that the Euclid's fifth postulate is not needed to build self-consistent geometries, thus giving rise to non-planar geometries (see Figure 1.2). In particular, it was highlighted the work of Nikolai Lobachevsky, father of non-euclidean geometries, and Bernhard Riemann, the founder of the Riemannian geometry.

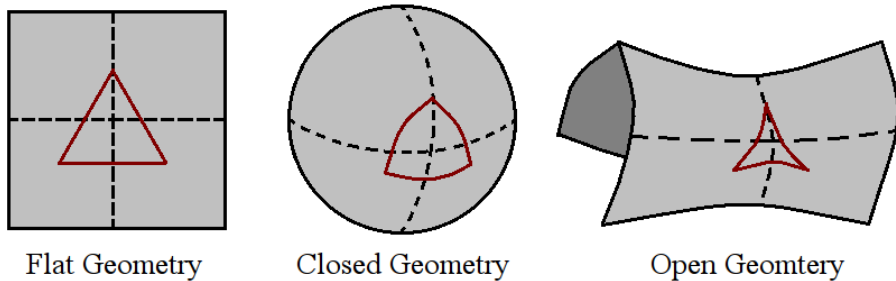


**Figure 1.2:** Different geometries according to variations on Euclid's fifth postulate.

In spite of these first developments contributed widely to the current cosmological paradigm, bringing forward discussions on what kind of geometry the universe has, the concepts of space and time were completely misunderstood yet, being interpreted as unrelated and absolute entities. That is why the foundation of the theory of general relativity opened the door to our whole current understanding.

Once obtained the equations of metric field of the general relativity, it was possible to build global and self-consistent models of the universe. A first rough attempt was also due to Einstein, who formulated, influenced by his own belief, a static and closed model of the universe. To achieve it, he must use the well-known cosmological constant in order to compensate the expansion/contraction obtained naturally by the theory.

Few years later, Aleksander Friedmann demonstrated on two articles a set of solutions for closed and hyperbolic universes' expanding from a singularity [10] [11].

## 1.2 The Current Cosmology Picture

---

These expanding solutions were in agreement with the observations made by Hubble for redshift of far galaxies. Because of that, the inclusion of the cosmological constant for stationary solutions it is historically known and recognized by Einstein himself as the biggest blunder of his life. This theoretical finding prompted a set of studies on the real nature of the universe in the light of those new solutions, like large-scale dynamics, global geometry and precise measurements of different cosmological parameters of those models.

The next important advance came with the formulation of the Big Bang theory by George Gamow. This theory proposes that early stages of the universe had been very dense and hot, starting from a singularity and reaching the current stage, a constantly cooling and expanding universe. All this is in agreement with the Friedmann's solutions. One of the first predictions of this theory was the early nucleosynthesis, which is responsible of the creation of heavy elements like helium and lithium through fusion reactions of primordial hydrogen. Because of the current abundances of helium and lithium cannot be given account by the standard nuclear processes in stars, this was the first of many achievement of the Big Bang theory; furthermore the early nucleosynthesis was later demonstrated by Ralph Alpher and Robert Herman and it has been observationally corroborated very precisely nowadays.



**Figure 1.3:** Cosmic background radiation. Taken from [http://upload.wikimedia.org/wikipedia/commons/3/3c/I1c\\_9yr\\_moll4096.png](http://upload.wikimedia.org/wikipedia/commons/3/3c/I1c_9yr_moll4096.png)

## 1. PRELIMINARIES

---

The next remarkable prediction of the Big Bang theory was the current existence of a residual black-body radiation from early stages, when, due to the conditions of high density and temperature, the universe was radiation-dominated. This remainder was verified observationally by Arno Penzias and Robert Wilson in 1965 with the discovery of the cosmic background radiation (CMBR). The spectrum of this residual radiation proved to be produced by an almost perfect black-body with a characteristic temperature of  $T = 2.725$  K. These predictions have made this theory being adopted as a fundamental part of the standard cosmological paradigm.

Although the discovery of the CMBR was certainly one the most important hits of the astronomy along the century twenty, as it has been established in many scientific disciplines, new answers lead to new questions. In this case, the horizon problem. This is originated by the high angular isotropy measured from the CMBR spatial spectrum (see Figure 1.3), which suggests a causal connection between regions of the universe very far apart from each other that, in theory, they should not be correlated. The widely accepted solution to this problem was proposed by Alan Guth in 1980, the inflationary theory. This postulates an exponential expansion of the early universe powered by a scalar field, the inflaton. During the time of expansion, vacuum quantum fluctuations of each field present in the universe was magnified by the expansion itself, producing small perturbations in the density field, from which would evolve current large-scale structures. According to this, the inflationary theory can explain satisfactorily the problem of small perturbations of the very early universe, becoming thus an essential part of the current paradigm.

The existence of dark matter was proposed since early 1930s, initially by Jan Oort in 1932 and then by Fritz Zwicky in 1933, in order to give account of non-luminous matter of galaxies and galaxy clusters, which is manifested through dynamical interactions of their single components, like stars or galaxies in the case of clusters. In spite of that, the real nature of this new type of matter remained as a complete mystery. In 1984 Joel Primack, George Blumenthal, Sandra Moore and Martin Rees proposed a model called cold dark matter (CDM), in which is postulated that dark matter is made of certain unknown type of non-relativistic particle which only interacts gravitationally and electromagnetically (more weakly). Under this scheme, it is possible to demonstrate that large-scale structure formation follows a *top-down* hierarchical process, in which the smallest structures are

## 1.2 The Current Cosmology Picture

formed first and the biggest, composed by the first, are formed later. This has been observationally verified through galaxy surveys (see section 1.3).

In the 1990s, some cosmological observations suggested an accelerated rate of expansion of the universe, which only can be explained (see subsection 2.1.3) with the inclusion of the cosmological constant in the field equations of the general relativity. Because this constant can be placed as an energy density term with negative pressure, the term of *dark energy* was quickly coined, even though its real nature is completely unknown. Very precise measurements have proved that our universe is currently vacuum-dominated, reaching 70% of all content of matter-energy of it. This last fact completes our overall picture of the current cosmological paradigm and it is called standard  $\Lambda$ CDM model or concordance model.



**Figure 1.4:** Local Group. Taken from [http://commons.wikimedia.org/wiki/File:Local\\_Group.svg](http://commons.wikimedia.org/wiki/File:Local_Group.svg)

The local group (LG) is a local system composed of 30 galaxies approximately, which interact gravitationally between them and evolve relatively isolated from other large-scale structures. The Milky Way and Andrómeda (M31) galaxies are

## 1. PRELIMINARIES

---

its more representative members and even in this work we shall simplify the local group just as systems of two galaxies similar to these (see Figure 1.4).

The importance of our local group in a cosmological context is because it is by far the best known large-scale structure, thereby allowing verifying some current predictions of the concordance model. Among the issues originated by these predictions, we highlight the over abundance of satellite galaxies in the Milky Way, the possible link between the flows of the Magellanic clouds and M31 galaxy, tidal forces in the local group, the kinematic of M31 and Milky Way galaxies in a cosmological context [9] and the influence of the cosmological environment on the formation properties of systems like the local group.

### 1.3 Cosmological Observations

The boom produced by the space age along with the significant technological development of measuring instruments and sensors have powered enormously observational research in cosmology, thereby allowing, together with the theoretical advances previously discussed, reaching the current cosmological picture. Next, we shall present some of the larger and more important observational projects in cosmology and which are widely used in current research.

#### 2DF Galaxy Redshift Survey

The 2DF Galaxy Redshift Survey (2DFGRS), or Two-Degree-Field Galaxy Redshift Survey<sup>1</sup>, is a galaxy redshift survey performed within an angular area of 1500 square degrees of regions near to the north and south galactic poles in order to avoid extinction produced by the galactic disk. This survey was made by the 3.9 m telescope of the Anglo-Australian observatory from 1997 to 2002. Among the main results of this survey are remarkable the mapping of the local structure of the large-scale environment around the local group of galaxies. This was achieved through photometric measurements of 382 323 objects within a redshift range of  $z = 0.3$  to  $z = 0.0$ . It is also remarkable the measuring of the density parameter of non-relativistic matter (dark + baryonic) of the standard cosmological model.

---

<sup>1</sup>Official web page of the project at <http://magnum.anu.edu.au/~TDFgg/>.

## Sloan Digital Sky Survey

The Sloan Digital Sky Survey (SDSS), like the 2DFGRS, is a redshift survey of the large-scale universe made by the 2.5 m telescope of the Apache Point observatory in New Mexico since 2000.

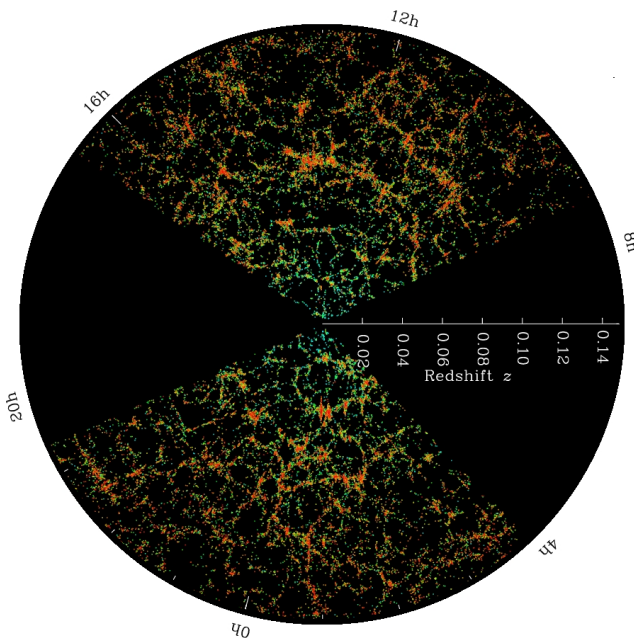


**Figure 1.5:** Map of the large-scale universe according to the Sloan Digital Sky Survey.

Taken from the official web page of the project <http://www.sdss.org/>

The survey covers an area significantly larger than 2DFGRS, approximately 7500 square degrees, and has catalogued around 2 million of objects, thereby allowing building a map of the large-scale universe in which it was first seen the structure of the cosmic web (see Figure 1.5).

## WMAP

The Wilkinson Microwave Anisotropy Probe (WMAP), is a NASA spacecraft launched in 2001 and placed in the lagrange point L2. Its main objective is to measure, with very high precision, small temperature contrasts and polarization of the cosmic background radiation (see Figure 1.3). Approximately every two years, NASA releases the accumulated results obtained, called as WMAP1, WMAP3, WMAP5,

## 1. PRELIMINARIES

---

WMAP7 and finally WMAP9 for data released in 2012. These results have been up to date the most reliable proof of the standard cosmological  $\Lambda$ CDM model. Specially it is remarkable the precise measuring of the age of the universe, the cosmological density parameters, the Hubble's constant, also the determination of the global geometry of the universe (flat geometry) and the confirmation of the inflationary model.

Parameter	Notation	Value	Unit
Age of universe	$t_0$	$13.75 \pm 0.13$	Ga
Hubble's constant	$H_0$	$71.0 \pm 2.5$	km/(Mpc s)
Hubble's parameter	$h$	$0.71 \pm 0.025$	–
Barion density	$\Omega_b$	$0.0449 \pm 0.0027$	–
Dark matter density	$\Omega_c$	$0.222 \pm 0.026$	–
Dark energy density	$\Omega_\Lambda$	$0.734 \pm 0.029$	–
Radiation density	$\Omega_r$	$8.24 \times 10^{-5}$	–
Amplitude of Fluctuations at $8h^{-1}$ Mpc	$\sigma_8^2$	$0.801 \pm 0.030$	–
Spectral index	$n_s$	$0.963 \pm 0.014$	–
Reionization optic depth	$\tau$	$0.088 \pm 0.015$	–
Total density of the Universe	$\Omega_0$	$1.080 +0.093/-0.071$	–

**Table 1.1:** WMAP7 cosmological parameters [20].

In Table 1.1 is tabulated all the results of the WMAP7 release [20], which are widely used in next chapters and specially in the different cosmological simulations presented below in the chapters 3 and 4.

*“The Cosmos is all that is or was or ever will be. Our feeblest contemplations of the Cosmos stir us: there is a tingling in the spine, a catch in the voice, a faint sensation, as if a distant memory, of falling from a height. We know we are approaching the greatest of mysteries”*

Carl Sagan

CHAPTER

# 2

# Theoretical Framework in Cosmology

The aim of this chapter is to cover, in a self-contained and summarized way, all the theoretical framework needed for the study of the large-scale universe. From the simplest models of the universe given by Friedman’s solutions, the theory of perturbations for the formation of complex structures like galaxies and galaxy clusters, until the schemes to quantify the cosmic web.

## 2.1 Isotropic and Homogeneous Universe

The two big pillars of the modern cosmology are the cosmological principle and the theory of the general relativity. The first one is a principle where it is assumed that the universe is isotropic and homogeneous at very large scales, while the second one gives the theoretical support needed in order to understand properly the relation between the matter content of the universe and the structure of the space-time.

As it has been evidenced by observations of large-scale structures and the CMB, the universe appears to be isotropic and homogeneous at large scales, which is in agreement with the cosmological principle. Moreover, this fact simplifies quite

## 2. THEORETICAL FRAMEWORK IN COSMOLOGY

---

enough the complex tensorial formulation of the general relativity, thereby allowing finally leading to the Friedmann's equations.

### 2.1.1 Metric of Curved Spaces

In the construction of an isotropic and homogeneous model of universe, it is necessary to establish an adequate metric which describes it properly. An illustrative example that could be generalized is a 2D spherical surface, which clearly satisfies the criteria of homogeneity and isotropy.

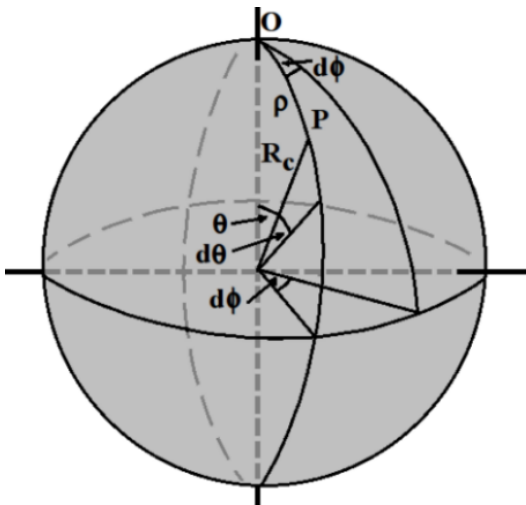


**Figure 2.1:** Metric of a spherical surface.

A line element over the surface shown in Figure 2.1 can be described as

$$dl^2 = d\rho^2 + R_c^2 \sin^2 \left( \frac{\rho}{R_c} \right) d\phi^2$$

where it have been introduced a new length coordinate over the surface, defined as  $\rho = \theta R_c$  and  $R_c$  is the curvature radius of the sphere. Another very convenient way to rewrite this expression, and that allowing a very useful generalization, it is reached defining the curvature parameter  $k$  and the coordinate  $r = \sin(\rho/a)$ , obtaining:

$$dl^2 = a^2(t) \left[ \frac{dr^2}{1 - kr^2} + r^2 d\phi^2 \right]$$

## 2.1 Isotropic and Homogeneous Universe

---

with  $k = -1$  and it is assumed a time-dependent curvature radius  $R_c = a(t)$ . The metric in this case is 3D and is obtained by replacing the differential element of angle  $d\phi^2$  by the solid angle differential  $d\Omega^2 = d\theta^2 + \sin^2 \theta d\phi^2$ .

$$dl^2 = a^2(t) \left[ \frac{dr^2}{1 - kr^2} + r^2(d\theta^2 + \sin^2 \theta d\phi^2) \right] \quad (2.1)$$

Finally, time is included, so the space-time interval for the metric of isotropic and homogeneous curved spaces is:

$$ds^2 = c^2 dt^2 - a^2(t) \left[ \frac{dr^2}{1 - kr^2} + r^2(d\theta^2 + \sin^2 \theta d\phi^2) \right] \quad (2.2)$$

The direct generalization of this expression consists in varying the different values of the curvature parameter  $k$  in order to obtain the metric of flat ( $k = 0$ ), spherical closed ( $k = -1$ ) or opened spaces ( $k = 1$ ), as it is shown in [26] or [27].

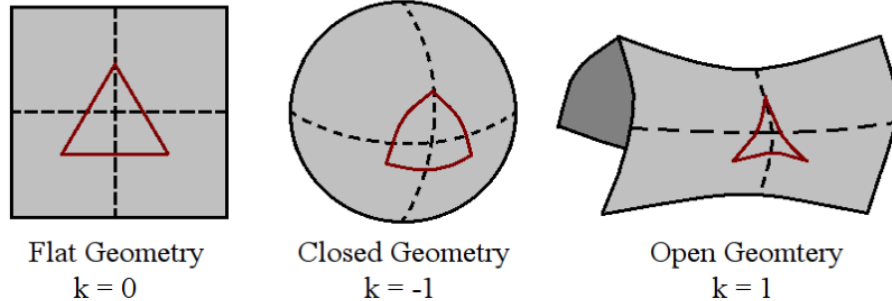


**Figure 2.2:** Curved spaces according to the curvature parameter.

An alternative way to rewrite the metric is introducing two changes of coordinates defined as

$$\chi = \int \frac{dr'}{\sqrt{1 - kr'^2}}$$

$$\tau = \int \frac{cdt'}{a(t')}$$

where each one is respectively interpreted as a length coordinate over the hyper-surface that defines the space ( $\chi$ ) and as the proper time measured locally ( $\tau$ ). It is obtained the next expressions for the metric

## 2. THEORETICAL FRAMEWORK IN COSMOLOGY

---

$$ds^2 = c^2 dt^2 - a^2(t) [d\xi^2 + f_k^2(\xi)(d\theta^2 + \sin^2 \theta d\phi^2)] \quad (2.3)$$

$$ds^2 = \bar{a}^2(\tau) [d\tau^2 - d\xi^2 - f_k^2(\xi)(d\theta^2 + \sin^2 \theta d\phi^2)] \quad (2.4)$$

where the function  $f_k(\chi)$  is defined according to the value of the curvature parameter.

$$f_k(\chi) = \begin{cases} \sin \chi & k = 1 \\ \chi & k = 0 \\ \sinh \chi & k = -1 \end{cases} \quad (2.5)$$

In spite of the derived expressions for the metric 2.2 2.3 and 2.4 are completely equivalent, the usage of one or another depends on the specific problem. Specially the expression 2.3 is usually more used and is defined as the Friedmann's metric.

It could be shown that in Riemannian manifolds <sup>1</sup>, the space-time interval is expressed in terms of the metric tensor as [33]

$$ds^2 = g_{\mu\nu} dx^\mu dx_\nu$$

where it has been introduced the cuadrvector  $x^\mu = (ct, r, \theta, \phi)$ .

Due to the assumption of isotropy and homogeneity, the metric tensor must be diagonal, furthermore, comparing with the expression 2.2, it is possible to obtain the next explicit form

$$g_{\mu\nu} = \begin{pmatrix} 1 & 0 & 0 & 0 \\ 0 & -a^2(t)(1 - kr^2)^{-1} & 0 & 0 \\ 0 & 0 & -a^2(t)r^2 & 0 \\ 0 & 0 & 0 & -a^2(t)r^2 \sin^2 \theta \end{pmatrix} \quad (2.6)$$

From this metric and the Einstein's field equations, it is possible to build simple models of the universe, such as it shall be shown in the subsection 2.1.2.

---

<sup>1</sup>A Riemannian manifold is a space where it can be defined (well-defined) a metric.

### Measuring Distances

Once defined the metric of curved spaces, it is very useful to introduce some concepts related with distances, which are used recurrently [26]. For the sake of simplicity it will be assumed a flat metric ( $k = 0$ ).

- **Comoving radial distance:** by definition, a light signal has an associated null interval, i.e.  $ds^2 = 0$ . Using the expression 2.2 for the metric, it is obtained

$$r = \int_t^{t_0} \frac{cdt'}{a(t')} = \int_a^1 \frac{cda}{a\dot{a}} \quad (2.7)$$

where the specific form of  $a(t)$  depends on the specific chosen cosmology (see subsection 2.1.3) and  $t_0$  is the reference time, which is taken as the current age of the universe.

Due to the assumption of an expanding metric, the distance between two objects depends on the time in which the measurement is performed. Moreover, the distance cannot be determined from a beam of light since light has a finite velocity <sup>1</sup>. Because of that, it must be performed a projection on the light-cone traced by the beam in the current time, such as it is made in the expression 2.8. The latter allows interpreting  $r$  as the distance to an object in the current time, and it is quite different to the apparent distance which corresponds to the time when the object in question emitted the observed light.

- **Proper radial distance:** by virtue of the definition of scale factor, to obtain the distance to an object in any time, it is enough to multiply the comoving distance by the scale factor evaluated in the same time, that is

$$r_{\text{prop}} = a(t) \int_t^{t_0} \frac{cdt'}{a(t')} = a \int_a^1 \frac{cda}{a\dot{a}} \quad (2.8)$$

- **Particle horizon:** considering a beam travelling through vacuum since the beginning of all time, at  $t = 0$ ; the maxim proper distance that could be travelled by the light in a time  $t$  is denominated particle horizon and determines

---

<sup>1</sup> $c = 299\,792\,458$  m/s

## 2. THEORETICAL FRAMEWORK IN COSMOLOGY

---

all regions in the universe that could have been causally connected in that time.

$$r_H = a(t) \int_0^t \frac{cdt'}{a(t')} = a \int_0^a \frac{cda}{a\dot{a}} \quad (2.9)$$

### 2.1.2 General Relativity and Friedmann's Equations

The Einstein's field equations of the general relativity play a fundamental role since they express explicitly the relation between the matter content of the universe and the local geometry of the space-time.

$$R_{\mu\nu} - \frac{1}{2}Rg_{\mu\nu} - g_{\mu\nu}\Lambda = \frac{8\pi G}{c^4}T_{\mu\nu} \quad (2.10)$$

or equivalently

$$R_{\mu\nu} + g_{\mu\nu}\Lambda = \frac{8\pi G}{c^4} \left( T_{\mu\nu} - \frac{1}{2}Tg_{\mu\nu} \right) \quad (2.11)$$

where  $T$  is the trace of the energy-momentum tensor (see 2.14),  $R_{\mu\nu}$  the Ricci curvature tensor and  $R$  the scalar curvature. The last two terms are calculated from different traces of the Riemann curvature tensor, as  $R_{\mu\nu} = R^\eta_{\mu\eta\nu}$  and  $R = R^\mu_\mu$ . For convenience, it has been introduced the term associated with the cosmological constant, which will be used below to calculate different models of the universe with dark energy contribution.

The Riemann curvature tensor quantifies deviations of the metric of curved space-times with respect to the Euclidean metric and allows to determinate completely the geometrical properties like the local curvature, different measures of distances and angles, etc. [33]. This tensor is built from the Levi-Civita connection as

$$R^\mu_{\nu\alpha\beta} = \Gamma^\mu_{\nu\alpha,\beta} - \Gamma^\mu_{\nu\beta,\alpha} + \Gamma^\mu_{\sigma\alpha}\Gamma^\sigma_{\nu\beta} - \Gamma^\mu_{\sigma\beta}\Gamma^\sigma_{\nu\alpha} \quad (2.12)$$

with the Levi-Civita connection defined from the metric as

$$\Gamma^\nu_{\alpha\beta} = \frac{1}{2}g^{\mu\sigma}(g_{\sigma\alpha,\beta} + g_{\sigma\beta,\alpha} - g_{\alpha\beta,\sigma}) \quad (2.13)$$

## 2.1 Isotropic and Homogeneous Universe

---

The right-hand side of the equation 2.10 contains the energy-momentum tensor  $T_{\mu\nu}$ , which characterizes the density and the matter-energy flux of the universe. By virtue of the cosmological principle, this tensor must also be diagonal and if, furthermore, it is assumed an ideal fluid model, the next form is obtained

$$T_{\nu}^{\mu} = \begin{pmatrix} c\rho^2 & 0 & 0 & 0 \\ 0 & -P & 0 & 0 \\ 0 & 0 & -P & 0 \\ 0 & 0 & 0 & -P \end{pmatrix} \quad (2.14)$$

Finally, using the equations 2.6, 2.11 and 2.14, it is possible to reduce the complex system of tensorial equations to two scalar coupled equations which are usually called Friedmann's equations [26]. These equations describe completely the evolution of an isotropic and homogeneous universe in terms of the scale factor  $a(t)$  (see equation 2.1)

$$\frac{\ddot{a}}{a} = -\frac{4\pi G}{3} \left( \rho + \frac{3P}{c^2} \right) + \frac{c^2 \Lambda}{3} \quad (2.15)$$

$$\frac{\ddot{a}}{a} + 2\frac{\dot{a}^2}{a^2} + 2\frac{c^2 k}{a^2} = 4\pi G \left( \rho - \frac{P}{c^2} \right) + c^2 \Lambda \quad (2.16)$$

In order to solve this equation system in terms of  $a(t)$  and thereby obtaining the evolution of the scale factor, it is necessary to know the explicit time-dependent expression of the density  $\rho$  and the pressure  $P$ , or equivalently, the dependence on the scale factor. This must be done for each type of energy-matter of the universe. A detailed derivation of these explicit expressions could be found in [26] and they are summarized in Table 2.1.

By convention, it has been taken the current scale factor as  $a_0 = a(t_0) = 1$  and the reference values are defined as  $\rho_0 = \rho(a_0)$ ,  $P_0 = P(a_0)$  and  $T_0 = T(a_0)$ . Using the Friedmann's equations, defining the Hubble parameter as  $H(t) = \dot{a}/a$  and the vacuum density as  $\rho_\Lambda = c^2 \Lambda / 8\pi G$ , it is obtained

$$\left( \frac{\dot{a}}{a} \right)^2 = H^2(t) = \frac{8\pi G}{3} \left[ \rho_m \frac{1}{a^3} + \rho_r \frac{1}{a^4} + \rho_\Lambda \right] - \frac{c^2 k}{a^2}$$

Evaluating this expression in the current epoch  $H(t_0) = H_0$ , with  $H_0$  the Hubble constant and defining the critical density  $\rho_c$  as the density that the universe must have in order to be flat.

## 2. THEORETICAL FRAMEWORK IN COSMOLOGY

---

Property	Density	Pressure	Temperature
<b>Matter</b> (baryonic + dark)	$\rho = \rho_0 a^{-3}(t)$	$p = p_0 a^{-5}(t)$	$T = T_0 a^{-2}(t)$
<b>Radiation</b> (+ relativistic matter)	$\rho = \rho_0 a^{-4}(t)$	$p = p_0 a^{-4}(t)$	$T = T_0 a^{-1}(t)$
<b>Vacuum</b>	$\rho = \rho_0$	$p = p_0$	—

**Table 2.1:** Dependence of some quantities on the scale factor  $a(t)$  [26].

$$\rho_c = \frac{3H_0^2}{8\pi G} \quad (2.17)$$

it leads to the equation of evolution for the Hubble parameter

$$H^2(t) = H_0^2 \left[ (1 - \Omega_0) \frac{1}{a^2} + \Omega_m \frac{1}{a^3} + \Omega_r \frac{1}{a^4} + \Omega_\Lambda \right] \quad (2.18)$$

where it has been introduced the density parameters  $\Omega_i$ , defined as the current density of the  $i$ -th specie in the current epoch, normalized with the critical density 2.17, and  $\Omega_0 = \sum_i \Omega_i$ . These density parameters along with the Hubble constant are part of the free parameters of the theory and must be determined by observations. This allows to characterize different particular cosmologies <sup>1</sup>

### 2.1.3 Simple Solutions of the Universe

Although in this stage it has not been introduced the complete formalism of small perturbations and structure formation, the set of equations 2.15, 2.16 and 2.18 leads to a first and rough understanding of the evolution of the Universe.

In this subsection, it will be presented some analytic solutions to the Friedmann's equations. In spite of the ideal assumptions on which are based, in some

---

<sup>1</sup>Cosmology must be understood in this context as a specific solution of the Friedmann's equations.

## **2.1 Isotropic and Homogeneous Universe**

---

cases, they can be used as approximations in some stages of evolution of the universe, thus allowing a physical understanding more adequate than exact numerical solutions.

### **Einstein - de Sitter Universe**

The Einstein-de Sitter Universe is a cosmological model with a flat metric and composed entirely of matter, this implies that  $\Omega_0 = \Omega_m = 1$  and  $k = 0$ . Applying this in equation 2.18, it is obtained the next expression

$$H^2(t) = \left(\frac{\dot{a}}{a}\right)^2 = H_0^2 \frac{1}{a^3} \quad (2.19)$$

Integrating, it leads to the explicit time-dependent solution for the scale factor

$$t(a) = \frac{2}{3H_0} a^{3/2} \quad (2.20)$$

Although in this case it is possible to obtain the explicit form of  $a(t)$ , most of the time it is only possible to have the implicit solution  $t(a)$ . Another very useful way to describe this solution is by using the redshift  $z$ , which is related with the scale factor as [26]

$$z + 1 = \frac{a_0}{a} \quad (2.21)$$

to finally obtain

$$t(a) = \frac{2}{3H_0} (1+z)^{-3/2} \quad (2.22)$$

This solution is quite close to the real behaviour of the universe in the matter-dominated epoch, between 70000 and 5 millions of years after the Big Bang [27].

### **Radiation-Dominated Universe**

In this case, it will be assumed that the universe is radiation-dominated, that is  $\Omega_0 = \Omega_r$ , but not necessarily flat. The Friedmann's equations lead to the next expression

## 2. THEORETICAL FRAMEWORK IN COSMOLOGY

---

$$H^2(t) = \left(\frac{\dot{a}}{a}\right)^2 = H_0^2 \left[ (1 - \Omega_r) \frac{1}{a^2} + \Omega_r \frac{1}{a^4} \right] \quad (2.23)$$

Integrating this expression, it is obtained the next implicit solution for the scale factor

$$t = \begin{cases} H_0^{-1}(\Omega_r - 1)^{-1} \left( \Omega_r^{1/2} - [a^2(1 - \Omega_r) + \Omega_r]^{1/2} \right) & \Omega_r \neq 1 \\ H_0^{-1}a^2/2 & \Omega_r = 1 \end{cases} \quad (2.24)$$

or in terms of redshift

$$t = \begin{cases} H_0^{-1}(\Omega_r - 1)^{-1} \left( \Omega_r^{1/2} - [(1+z)^{-2}(1 - \Omega_r) + \Omega_r]^{1/2} \right) & \Omega_r \neq 1 \\ H_0^{-1}(1+z)^{-2}/2 & \Omega_r = 1 \end{cases} \quad (2.25)$$

This solution is useful as an approximation for the radiation-dominated epoch, which happened from the big bang until the recombination epoch, approximately 380000 years after the big bang, or equivalently in a redshift of  $z = 1100$  [27].

### Vacuum-dominated Universe

This type of hypothetical universe is completely vacuum-dominated, or equivalently dominated by the cosmological constant. Making  $\Omega_0 = \Omega_\Lambda$  in the Friedmann's equations, it is obtained

$$H^2(t) = \left(\frac{\dot{a}}{a}\right)^2 = H_0^2 \left[ (1 - \Omega_\Lambda) \frac{1}{a^2} + \Omega_\Lambda \right] \quad (2.26)$$

Solving for  $t(a)$

$$t = \frac{1}{H_0^2 \Omega_\Lambda^{1/2}} \ln \left[ a \left( \frac{\Omega_\Lambda}{1 - \Omega_\Lambda} \right)^{1/2} + \left( 1 + \frac{\Omega_\Lambda}{1 - \Omega_\Lambda} a^2 \right)^{1/2} \right] \quad (2.27)$$

and using the redshift

$$t = \frac{1}{H_0^2 \Omega_\Lambda^{1/2}} \ln \left[ \frac{1}{1+z} \left( \frac{\Omega_\Lambda}{1 - \Omega_\Lambda} \right)^{1/2} + \left( 1 + \frac{\Omega_\Lambda}{1 - \Omega_\Lambda} \frac{1}{(1+z)^2} \right)^{1/2} \right] \quad (2.28)$$

## 2.1 Isotropic and Homogeneous Universe

---

This solution is very interesting because, unlike the previous solutions, is only valid for values of the density parameter within the range  $0 < \Omega_\Lambda < 1$ . This implies that it is not possible to have a universe with flat or hyperbolic geometry when it is vacuum-dominated. Another aspect equally remarkable is the concavity of the scale factor  $a(t)$  obtained from 2.27 (see Figure 2.3), which shows an accelerated expansion of the universe. This characteristic is only possible when there is a non-null term associated to the vacuum energy.

Finally and like the previous solutions, the expression 2.27 can be used as an approximation for the vacuum-dominated epoch of the universe, which lasts from the end of the matter-dominated epoch, 5 millions of years after the big bang, until nowadays [26].

### WMAP7 Universe

The set of parameters associated to the standard cosmological model has been measured on several occasions by different spacecraft missions (see section 1.3). Among those measurements it is notable the one conducted by WMAP. The data obtained after seven years of observation (WMAP7) are adopted in this work [20]. Among the cosmological parameters measured are the Hubble constant and the density parameters  $\Omega_i$ . Taking the values given in Table 1.1 and for simplicity assuming  $\Omega_0 = 1$  it is possible to integrate the Friedmann's equations

$$H^2(t) = H_0^2 \left[ \Omega_m \frac{1}{a^3} + \Omega_r \frac{1}{a^4} + \Omega_\Lambda \right] \quad (2.29)$$

to obtain

$$t = \frac{1}{H_0} \int_0^a \left[ \Omega_m \frac{1}{a'} + \Omega_r \frac{1}{a'^2} + \Omega_\Lambda a'^2 \right]^{-1/2} da' \quad (2.30)$$

It is possible to obtain an analytic solution of this integral in terms of elliptic functions, but for simplicity it is chosen the numerical solution. In Figure 2.3 is shown the solution for a WMAP7 universe and it is compared to other cosmologies, derived previously.

An interesting characteristic of the solution for the WMAP7 universe is the change of concavity (black curve in Figure 2.3), which indicates a transition from

## 2. THEORETICAL FRAMEWORK IN COSMOLOGY

---

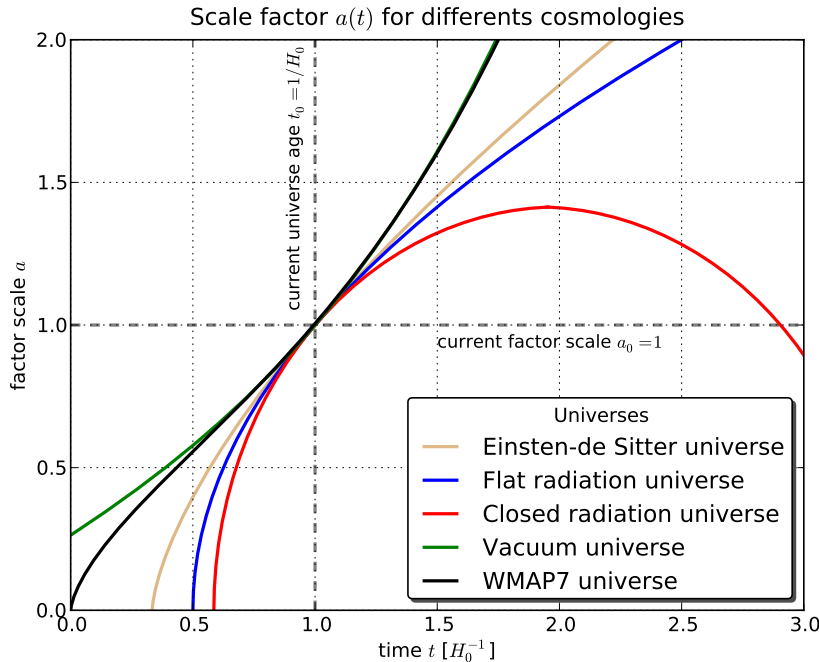


**Figure 2.3:** Different solutions of the universe according to the Friedmann's equations.

the matter/radiation-dominated epoch to an accelerated expanding regime associated to the vacuum energy. Another important aspect is the prediction of the age of the universe. Taking into account the previously defined normalization for the scale factor  $a(t_0) = a_0$ , it is straightforward to see that  $t_0 = H_0^{-1} \approx 13.75 \times 10^9$  years. Other cosmologies under the same normalization predict different ages, since larger values such as a vacuum-dominated universe, until smaller and even a collapse time (usually known as big crunch time) such as a radiation-dominated and closed universe.

## 2.2 Linear Regime of Structure Formation

The previous section deals about the universe as a whole, assuming as valid the condition of isotropy and homogeneity. Although the real universe has this asymptotic behaviour at very large scales, at smaller local scales the behaviour is quite different, being even completely anisotropic and highly non-homogeneous. Life is

## 2.2 Linear Regime of Structure Formation

---

certainly the most illustrative example of that, one of the highest non-linearities of the universe, and thus, planets, stars, galaxies, galaxy clusters, in the same decreasing order of inhomogeneity and anisotropy.

The standard way to introduce these local structures in the universe is by assuming as valid the solutions of the Friedmann's equations at very large scales, but considering inhomogeneities as perturbations of the model. First, in the linear regime, where the perturbations in the density field are much smaller than the background mean density ( $\delta\rho \ll \rho_b$ ), and after, in the non-linear regime, where the perturbations are comparable or even larger ( $\delta\rho \sim \rho_b$ ) (see section 2.3).

### 2.2.1 Newtonian Approximation

The frame of linear evolution can be presented in two ways. The first one is by considering a perturbative term in the energy-momentum tensor  $\delta T_{\mu\nu}$  and linearizing the Einstein's field equations 2.10 and finally solving for  $\delta R_{\mu\nu}$

$$\mathcal{L}(R_{\mu\nu}, \delta R_{\mu\nu}) = \frac{8\pi G}{c^2} (T_{\mu\nu} + \delta T_{\mu\nu}) \quad (2.31)$$

Although this method is, rigorously, more adequate, it has an inconvenience which makes it very complicated of applying. Non-perturbative terms are not necessarily small in all the coordinate systems, inclusively, they can reach values with the same order or even bigger than the background mean density [27].

The second method consists in assuming perturbations with a comoving size smaller than the Hubble radius ( $r_\delta \ll r_H \sim cH_0^{-1}$ )<sup>1</sup>, thereby being possible to neglect relativistic effects due to the curvature of the space-time. Once this is done, it is possible to use a Newtonian scheme to evolve perturbations of the background universe. This scheme assumes that the matter content of the universe is a fluid described by three basic equations of fluid mechanics. The first one is the continuity equation, which expresses mass conservation in a fluid

$$\frac{d\rho}{dt} = -\rho \nabla \cdot \mathbf{u} \quad (2.32)$$

---

<sup>1</sup>The Hubble radius  $r_H$  is a length unit that defines the order of magnitude of the size of the observable universe.

## 2. THEORETICAL FRAMEWORK IN COSMOLOGY

---

The second one, Euler's equation, characterizes the velocity field of the fluid, and physically it expresses the momentum conservation law

$$\frac{d\mathbf{u}}{dt} = -\frac{\nabla P}{\rho} - \nabla\varphi \quad (2.33)$$

And finally the Poisson's equation, which is the non-relativistic version of the Einstein's field equations and expresses the relation between the matter content of the universe and sources of gravitational field.

$$\nabla^2\varphi = 4\pi G\rho \quad (2.34)$$

In order to complete the Newtonian frame of perturbations is necessary to include in the previous system of equations (2.32, 2.33 and 2.34) the effect of the expansion of the universe by making a change of coordinates of the proper distance  $\mathbf{x}$  to comoving distance  $\mathbf{r}$

$$\mathbf{x} = a\mathbf{r}$$

this implies that

$$\mathbf{u} = \frac{d\mathbf{x}}{dt} = \frac{\dot{a}}{a}\mathbf{x} + \mathbf{v} = \dot{a}\mathbf{r} + \mathbf{v}$$

This way to rewrite  $\mathbf{u}$  allows separating the contribution of the expansion of the universe ( $\dot{a}/a\mathbf{x}$ ), also called Hubble's law, from the component due to the movement of the fluid, called peculiar velocity field and it is defined as  $\mathbf{v} = a\dot{\mathbf{r}}$ .

For the sake of simplicity it is decomposed the density field of the fluid into two parts, the background contribution and a perturbative term, that is  $\rho = \bar{\rho} + \delta\rho = \bar{\rho}(1 + \delta)$ , where  $\delta$  is called the density parameter and is dimensionless. In the case of the gravitational potential  $\varphi$ , it is defined a new field given by  $\Phi = \phi + \ddot{a}ar^2/2$  [26]. With these considerations it is finally obtained the final set of equations for describing a fluid in the Newtonian frame.

Continuity equation	$\frac{\partial\delta}{\partial t} = -\frac{1}{a}\nabla_r \cdot [(1 + \delta)\mathbf{v}] \quad (2.35)$
------------------------	--

## 2.2 Linear Regime of Structure Formation

---

$$\begin{array}{ll} \text{Euler's} & \frac{\partial \mathbf{v}}{\partial t} + \frac{\dot{a}}{a} \mathbf{v} + \frac{1}{a} (\mathbf{v} \cdot \nabla_r) \mathbf{v} = -\frac{\nabla_r P}{a \bar{\rho}(1+\delta)} - \frac{1}{a} \nabla_r \Phi \end{array} \quad (2.36)$$

$$\begin{array}{ll} \text{Poisson's} & \nabla_r^2 \Phi = 4\pi G \bar{\rho} a^2 \delta \\ \text{equation} & \end{array} \quad (2.37)$$

Until this stage it has not made explicit what type of matter-energy content is described by the above perturbative fluid equations (e.g. radiation, dark matter, dark energy). Taking into account the followed procedure to derive the previous system of equations, it can be noticed that no *a priori* assumption has been made about the explicit dependence of the state variables on the scale factor (see table 2.1), therefore they are valid for any of the different species<sup>1</sup> present in the universe. Bearing in mind that the structures of the current universe are completely composed of matter, it will be only used the Newtonian frame for this specie.

The physical quantities that must be determined by the fluid equations together with the Friedmann's equations are: the density parameter  $\delta$ , the peculiar velocity field  $\mathbf{v}$ , the effective potential  $\Phi$ , the pressure  $P$  and finally the scale factor  $a$ . It is then so clear that another extra equation is needed in order to get a completely self consistent problem. This is reached by introducing an equation of state for the pressure. For simplicity it is assumed a mono-atomic gas model for the matter, with an associated equation of state given by

$$\nabla_r P = c_s^2 \bar{\rho} \nabla \delta + \frac{2}{3} \bar{T} \rho \nabla s \quad (2.38)$$

where  $c_s$  is the velocity of sound in the medium,  $\bar{T}$  the background temperature and  $s$  the specific entropy. Using this expression along with 2.35 and 2.36, it is obtained the general equation for the evolution of the perturbations

$$\frac{\partial^2 \delta}{\partial t^2} + 2 \frac{\dot{a}}{a} \frac{\partial \delta}{\partial t} = 4\pi G \bar{\rho} \delta + \frac{c_s^2}{2} \nabla^2 \delta + \frac{2}{3} \frac{\bar{T}}{a^2} \nabla^2 s \quad (2.39)$$

In the linear regime,  $\delta \ll 1$ , the modes of the density field evolve independently from each other, thus allowing decoupling the perturbations at different size scales. A very standard way to solve this type of problems is by using Fourier transform because in the reciprocal space the modes of the field are decoupled naturally.

---

<sup>1</sup>Henceforth, each one of the different matter-energy contents that contributes to the momentum-energy tensor, will be called *specie*.

## 2. THEORETICAL FRAMEWORK IN COSMOLOGY

---

Since it has been assumed perturbations with characteristic lengths smaller than the Hubble's radius, the volume of the observable universe can be considered finite, and therefore decomposition of the fields in comoving coordinates becomes discrete, obtaining

$$\begin{aligned}\delta(\mathbf{r}, t) &= \sum_{\mathbf{k}} \delta_{\mathbf{k}} e^{i\mathbf{k} \cdot \mathbf{x}} & \mathbf{v}(\mathbf{r}, t) &= \sum_{\mathbf{k}} \mathbf{v}_{\mathbf{k}} e^{i\mathbf{k} \cdot \mathbf{x}} \\ s(\mathbf{r}, t) &= \sum_{\mathbf{k}} s_{\mathbf{k}} e^{i\mathbf{k} \cdot \mathbf{x}} & \Phi(\mathbf{r}, t) &= \sum_{\mathbf{k}} \Phi_{\mathbf{k}} e^{i\mathbf{k} \cdot \mathbf{x}}\end{aligned}\quad (2.40)$$

If adiabatic perturbations are assumed, that is, perturbations that cannot interchange heat with their environment (the background universe) while they are evolving, the specific entropy must remain homogeneous and therefore  $\nabla_r s = 0$  [26]. Considering this and using the previous decompositions of the fields, it is reached the next set of equations for evolving the modes of the density and peculiar velocity fields associated to the perturbations.

$$\frac{d^2 \delta_{\mathbf{k}}}{dt^2} + 2 \frac{\dot{a}}{a} \frac{d\delta_{\mathbf{k}}}{dt} = \left[ 4\pi G \bar{\rho} - \frac{c_s^2}{a^2} k^2 \right] \delta_{\mathbf{k}} \quad (2.41)$$

$$-k^2 \Phi_{\mathbf{k}} = 4\pi G \bar{\rho} a^2 \delta_{\mathbf{k}} \quad (2.42)$$

$$\mathbf{v}_{\mathbf{k}} = \frac{i a \mathbf{k}}{k^2} \frac{d\delta_{\mathbf{k}}}{dt} \quad (2.43)$$

### 2.2.2 Jeans Instability

Solutions to the equation 2.41 for the modes of the density field can be classified into two different families. The first one is a set of solutions where the amplitude of each mode oscillates over time and does not collapse. The second family is a set of solutions where each mode grows up over time, collapsing and becoming highly non-linear ( $\delta_k \gg 1$ ). A quite simple example that illustrates the above discussed and can be generalized, involves taking perturbations in a static universe, that is  $\dot{a} = 0$ . Taking this into account, the equation 2.41 is rewritten as

## 2.2 Linear Regime of Structure Formation

---

$$\frac{d^2\delta_k}{dt^2} - \omega_k^2 \delta_k = 0, \quad a = \text{cte} \quad (2.44)$$

where it has been defined the characteristic frequency  $\omega_k$  as

$$\omega_k^2 = \left[ \frac{c_s^2}{a^2} k^2 - 4\pi G \bar{\rho} \right] \quad (2.45)$$

Expression 2.44 is called Jeans equation and it has the form of a wave equation. Based upon this, solutions can be classified according to the value of  $\omega_k$ , such as it has been said initially.

- If  $\omega_k^2 > 0$ , the mode  $\delta_k$  behaves like an oscillator, while it maintains its oscillation amplitude constant over time. This solution is not of interest in the context of structure formation because it is not possible to lead gravitational collapse.
- If  $\omega_k^2 < 0$ , the amplitude of the mode  $\delta_k$  grows up over time, thereby allowing gravitational collapse and formation of non-linear structures.

Expression 2.45 for  $\omega_k$ , along with the previously defined criteria to determine the type of solution, allow to define the Jeans length  $\lambda_J$

$$\lambda_J = \frac{2\pi a^2}{k_J} = c_s \left( \frac{\pi}{G \bar{\rho}} \right)^{1/2} \quad (2.46)$$

This length can be interpreted as the minimal size in comoving coordinates that must have a perturbation in a homogeneous and static medium with a density value  $\bar{\rho}$ , in order to collapse gravitationally. In this same context it is possible to define the Jeans mass as the minimal mass value needed for the collapse.

$$M_J = \frac{4}{3} \pi \lambda_J^3 \propto \frac{c_s^3}{G^{3/2} \bar{\rho}^{1/2}} \quad (2.47)$$

In spite of the results previously derived are only strictly valid for static mediums, the importance of considering it lies in two reasons: the first one is the historic interest, just because the problem of perturbations that grow up in homogeneous mediums emerged initially in the context of stellar astronomy, where it is necessary

## 2. THEORETICAL FRAMEWORK IN COSMOLOGY

---

to calculate the minimal mass of a perturbation in a gas cloud needed for its collapse and subsequent formation of stars and planetary systems. The second reason is that the solution for static mediums allows evaluating the asymptotic behaviour and the validation of general solutions for expanding mediums.

Before to continue with the solutions for expanding mediums, it is convenient to use the definitions of the Jean mass and length as an approach for the general case. In order to obtain this, table 2.1 is used to evaluate the dependence on the scale factor of each physical property, furthermore the definition of the velocity of sound in a medium [28]

$$c_s^2 = \left( \frac{\partial P}{\partial \rho} \right)_s \quad (2.48)$$

- In the case of baryonic matter perturbations, it is used the equation of state for an ideal gas assumed of monoatomic hydrogen, and this leads the below expression for the Jeans mass

$$M_J \approx 9.97 \times 10^5 \left( \frac{a_{rc}}{a} \right)^{3/2} M_\odot \quad (2.49)$$

For convenience it has been introduced the scale factor that corresponds to the recombination epoch <sup>1</sup> $a_{rc}$ .

- For radiation and relativistic matter perturbations, it is used the equation of state for the radiation pressure of the electromagnetic field [19]  $P = c^2 \rho / 3$  and the Stefan-Boltzmann law  $\rho \propto T^4$ . It is obtained the next expression for the Jeans mass

$$M_J \approx 8.39 \times 10^{27} a^3 M_\odot \quad (2.50)$$

Both cases can be used as approximations for different stages of the universe. Before to the epoch of recombination, when matter and radiation were coupled via Compton scattering, perturbations collapse only if they have a mass value close

---

<sup>1</sup>Epoch in which matter and radiation got decoupled, it happened in a redshift of  $z_{rc} \approx 1000$ , approximately

## 2.2 Linear Regime of Structure Formation

to the Jean mass 2.50. After of this epoch, when matter evolves independently, expression 2.49 becomes valid.

In Figure 2.4 is illustrated how the Jeans mass changes with the scale factor. It is interesting to notice that before to the epoch of recombination, formation of low-mass structures was impeded due to the homogenization process produced by diffusion of photons in the medium. After of this epoch, when baryonic matter perturbations arises, it is possible to form low-mass structures (like globular clusters), what is in agreement with the theory of hierarchical large-scale structure formation.

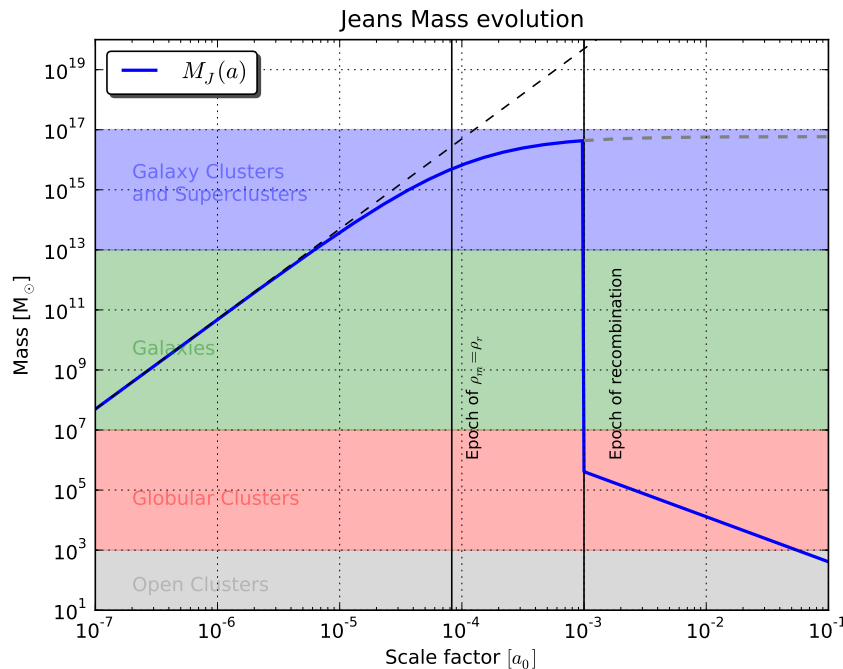


**Figure 2.4:** Evolution of the Jean mass for different stages of the universe. Coloured regions illustrate the typical mass range of some types of structures, since open stellar clusters to superclusters of galaxies.

The previous analysis has allowed to establish the minimal mass of a perturbation in order to collapse. Next it is studied the evolution of such perturbations in expanding mediums. For this it is used the models of the universe derived in the subsection 2.1.3 and the general equation 2.41 for evolving perturbations.

## 2. THEORETICAL FRAMEWORK IN COSMOLOGY

---

- **Einstein - de Sitter universe**

Bearing in mind that for this type of universe  $\Omega_m = \Omega_0 = 1$ , using the Hubble's function 2.19, the solution for the scale factor 2.20, the velocity of sound derived from 2.48 and the equation of state for an ideal gas, it leads to the below expression for the evolution of the perturbations

$$\delta_k(a) = \delta_{k,0} \left( \frac{a}{a_{\text{ref}}} \right)^1 \quad (2.51)$$

where  $\delta_{k,0}$  are the conditions of the field over the reference time  $t_{\text{ref}}$ . Another possible solution is  $\delta_k \propto a^{-3/2}$ , but because this solution does not decrease over time, it is not interesting.

- **Radiation-dominated universe**

For perturbations in a radiation-dominated universe with  $\Omega_r = \Omega_0 = 1$ , using the equation 2.24, it is obtained

$$\delta_k(a) = \delta_{k,0} \left( \frac{a}{a_{\text{ref}}} \right)^{1.22} \quad (2.52)$$

where  $\delta_{k,0}$  again represents the initial modes of the field, divergent solutions are ignored.

- **Vacuum-dominated universe**

For a universe with cosmological constant  $\Omega_\Lambda$ <sup>1</sup> it is obtained the next behaviour for the evolution of each mode

$$\delta_k(a) = \delta_{k,0} \left( \frac{a}{a_{\text{ref}}} \right)^{0.58} \quad (2.53)$$

Plotting each one of these solutions, Figure 2.5 is obtained. For simplicity and in order to illustrate in a better way the behaviour of the scale factor, it is normalized each solution with respect to their respective value in the reference time  $\delta_{k,0}$ .

---

<sup>1</sup> $\Omega_\Lambda < 1$  in order to guarantee the convergence of solutions to the Friedmann's equation (see subsection 2.1.3).

## 2.2 Linear Regime of Structure Formation

Initial conditions depend on the comoving wavenumber  $k$  and must be determined from the statistical properties of the density field (see subsection 2.2.3) and observational measurements, for instance the cosmic background radiation.

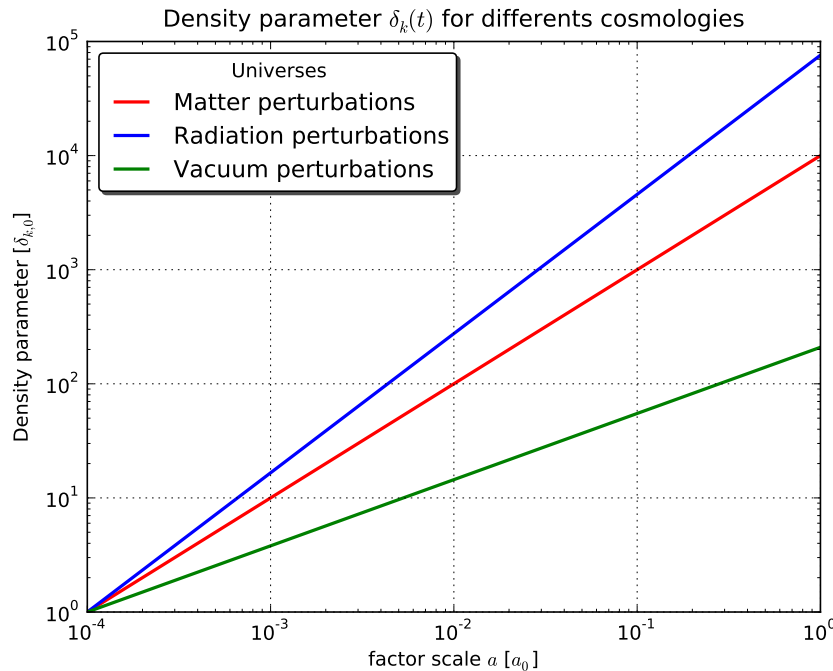


**Figure 2.5:** Evolution of the normal modes of the density field. For the sake of the illustration, each solution has been normalized with respect to the initial conditions.

### 2.2.3 Statistical Properties and Transfer Function

Once determined how each mode of the density field evolves, it is necessary to compare this with observations of the real universe. Due to the continuous nature of fields, it is infeasible to try to determine observationally the density distribution. Moreover, taking into account that most of matter is dark, which just can be measured by indirect methods, it is technically impossible, with the current instruments, carrying out this enterprise.

In spite of the above, it is still possible to measure the statistical properties of the density distribution of the universe and to compare them with theoretical predictions. In order to do this, it is introduced the concept of probability functional

## 2. THEORETICAL FRAMEWORK IN COSMOLOGY

---

of a continuous field  $P[\delta(\mathbf{r}, t)]$ , defined as the probability that a certain function has an explicit functional form  $\delta(\mathbf{r}, t)$ .

A computationally more convenient way to apply the formalism of probability functional is by discretizing the volume in a set of cells  $\Delta^3 \mathbf{r}_i$ , such that a certain explicit functional form of the density field  $\delta(\mathbf{r}, t)$  is equivalent to have simultaneously in each cell  $\mathbf{r}_i$  of the grid the value  $\delta_i = \delta(\mathbf{r}_i)$ , so the probability functional becomes equal to a joint probability function.

$$P[\delta(\mathbf{r}, t)] \longrightarrow \mathcal{P}_{\mathbf{r}}(\delta_1, \delta_2, \dots, \delta_N; t) \quad (2.54)$$

Taking into account the Fourier decomposition of the density field  $\delta(\mathbf{r}, t)$  introduced in the equations 2.40, it is possible to define a joint probability function in the reciprocal space  $\mathcal{P}_{\mathbf{k}}(\delta_{\mathbf{k}_1}, \delta_{\mathbf{k}_2}, \dots, \delta_{\mathbf{k}_N}; t)$  that completely characterizes the probability of a given distribution  $\delta_{\mathbf{k}}(t)$ .

The main motivation to work over the reciprocal space is because it is possible to use the approach of uncorrelated modes, where it is assumed that each mode evolves independently of the others. In the real space it is not possible to assume this since the long-range nature of the gravitational interaction couples strongly the density field between different locations. A direct consequence of the previous approach is to express the joint probability function as the product of  $N$  single distributions [27]

$$\mathcal{P}_{\mathbf{k}}(\delta_{\mathbf{k}_1}, \delta_{\mathbf{k}_2}, \dots, \delta_{\mathbf{k}_N}; t) = \prod_{\mathbf{k}_i} g_{\mathbf{k}_i}(\delta_{\mathbf{k}_i}; t) \quad (2.55)$$

where

$$\delta_{\mathbf{k}} = \int_V \delta(\mathbf{r}) e^{-i\mathbf{k}\cdot\mathbf{r}} d^3\mathbf{r} \quad (2.56)$$

$g_{\mathbf{k}_i}$  is the single distribution of each mode,  $V = L^3$  the normalization volume and  $\mathbf{k} = (2\pi/L)\mathbf{n}$ , with  $\mathbf{n}$  a vector of integer components that characterizes the specific mode.

Assuming that primordial perturbations of the density field were originated by the process of cosmic inflation, it is possible to demonstrate that the distribution of normal modes  $g_{\mathbf{k}_i}$  is a Gaussian function [27]. For convenience, it is decomposed

## 2.2 Linear Regime of Structure Formation

---

into complex polar coordinates the  $\delta_{\mathbf{k}}$  mode of the density field,  $\delta_{\mathbf{k}} = r_{\mathbf{k}} \exp(i\phi_{\mathbf{k}})$ , which leads to the next distribution

$$g_{\mathbf{k}}(r_{\mathbf{k}}, \phi_{\mathbf{k}}; t) = \frac{2(r_{\mathbf{k}} dr_{\mathbf{k}})}{\sigma_k^2} \left( \frac{d\phi_{\mathbf{k}}}{2\pi} \right) \exp \left( -\frac{r_{\mathbf{k}}^2}{\sigma_k^2} \right); \quad \sigma_k^2 = 2\mu_k^2 \quad (2.57)$$

where  $\mu_k^2$  is the variance of the distribution and  $\sigma_k^2$  is the power spectrum. Due to the assumption of isotropy and homogeneity for the background universe, both quantities only depends on the norm of the wave vector  $|\mathbf{k}| = k$ . Furthermore it is direct to demonstrate the below properties of the distribution of the field

$$\langle \delta_{\mathbf{k}} \rangle = 0; \quad \langle |\delta_{\mathbf{k}}|^2 \rangle = \sigma_k^2; \quad \langle \delta_{\mathbf{k}} \delta_{\mathbf{p}} \rangle = 0 \quad \text{si } \mathbf{k} \neq \mathbf{p} \quad (2.58)$$

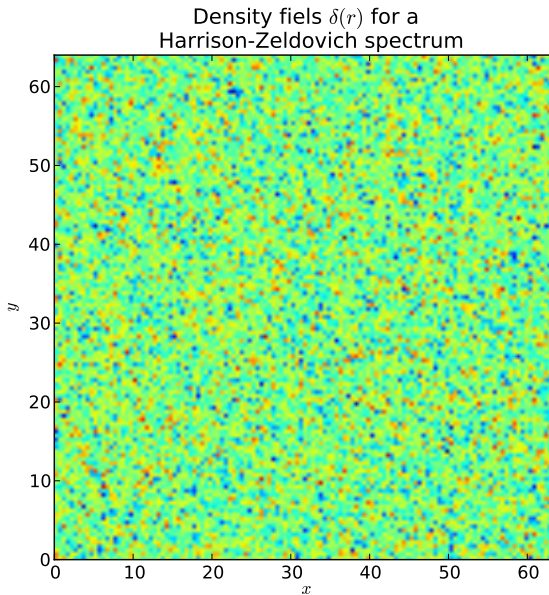


**Figure 2.6:** Initial distribution of perturbations for the density contrast field from the Gaussian distribution 2.57 and the Harrison-Zeldovich power spectrum  $\sigma_k \propto k$ .

A quantity that can be directly evaluated is the two-point correlation function  $\xi(\mathbf{r}) \equiv \langle \delta(\mathbf{r}' + \mathbf{r}) \delta(\mathbf{r}') \rangle$ , defined as the probability of a perturbation at a distance  $\mathbf{r}$  from another. It is a direct measurement of the anisotropy degree and the clustering properties of a certain distribution.

## 2. THEORETICAL FRAMEWORK IN COSMOLOGY

---

$$\begin{aligned}\xi(\mathbf{r}) = \langle \delta(\mathbf{r}' + \mathbf{r})\delta(\mathbf{r}') \rangle &= \frac{1}{V^2} \sum_{\mathbf{k}, \mathbf{p}} \langle \delta_{\mathbf{k}} \delta_{\mathbf{p}}^* \rangle \exp [i\mathbf{k} \cdot (\mathbf{r}' + \mathbf{r}) - i\mathbf{p} \cdot \mathbf{r}'] \\ &= \int \frac{V^{-1}}{(2\pi)^3} \sigma_k^2 e^{i\mathbf{k} \cdot \mathbf{r}} d^3 \mathbf{k}\end{aligned}\quad (2.59)$$

where in the last line has been performed the continuous approximation. The expression 2.59 shows that  $\sigma_k^2$  is the Fourier transform of the correlation function, that is

$$V^{-1} \sigma_k^2 = \int \xi(\mathbf{r}) e^{-i\mathbf{k} \cdot \mathbf{r}} d^3 \mathbf{r} \quad (2.60)$$

The previous relation along with the Gaussian distribution of the field show that both, the power spectrum and the correlation function, contain all the statistical information of the density field in the linear regime. If it is assumed a non-Gaussian distribution, it would be necessary to have more moments of the distribution, such as the three-point correlation function, etc.

### Harrison-Zeldovich Power Spectrum

A first approximation to the power spectrum of primordial perturbations and that can be demonstrated from the model of cosmic inflation [27] is the next power law expression

$$\sigma_k^2 = A k^{n_s} \quad (2.61)$$

where  $A$  is a normalization factor and  $n$  is the spectral index. In the specific case where this index is taken to be  $n_s = 1$ , it is called Harrison-Zeldovich power spectrum and is scale invariant<sup>1</sup>.

In order to determine the normalization factor, it is common to apply a filter to the normal modes that contributes to the density field, which leads to the next form of the correlation function

$$\xi(\mathbf{r}; R) = \int \frac{V^{-1}}{(2\pi)^3} \sigma_k^2 e^{i\mathbf{k} \cdot \mathbf{r}} \tilde{W}(k; R) d^3 \mathbf{k} \quad (2.62)$$

---

<sup>1</sup>The observed value is very close to 1,  $n_s = 0.963$  (see Table 1.1).

## 2.2 Linear Regime of Structure Formation

---

where  $R$  determines the maximum scale from which is applied the filter to the modes of the density field and  $\tilde{W}(k; R)$  is the Fourier transform of the filter function. Specially, it is defined the dispersion in the real space associated to a scale  $R$  as  $\sigma_R^2 = \langle \delta^2 \rangle = \xi(0; R)$ , this parameter can be determined observationally from galaxy surveys and the cosmic background radiation. The value measured by the WMAP7 release is  $\sigma_8^2 = \xi(0; R = 8 \text{ Mpc}/h) = 0.801$  (see Table 1.1), this leads to

$$\sigma_8^2 = A \int \frac{V^{-1}}{(2\pi)^3} k^{n_s} \tilde{W}(k; R = 8 \text{ Mpc}/h) d^3 k \quad (2.63)$$

thus, from the measured values of  $n_s$  and  $\sigma_8^2$ , it is possible to find the correct normalization of the power spectrum.

### Transfer Function

Finally for the linear regime, it is introduced the concept of transfer function  $T_k(t)$ , defined from the below expression

$$\delta_k(t) = T_k(t) \delta_k(t_i) \quad (2.64)$$

where  $t_i$  is a reference time, normally taken to be the recombination epoch for matter perturbations.

From the expression 2.64 can be inferred that the transfer function contains all the information about the dynamics of the perturbations, moreover, from the definition 2.58 for the power spectrum it is obtained

$$\sigma_k(t) = \sigma_k(t_i) |T_k(t)|^2 = A k^{n_s} |T_k(t)|^2 \quad (2.65)$$

where it has been assumed a Harrison-Zeldovich power spectrum for the reference time. With this, finally it is concluded that the transfer function also allows to obtain all the statistical properties of the density field during the time when the linear regime is valid.

Calculating the transfer function is generally a complex process and requires numerical computations <sup>1</sup>, furthermore, it depends on the specific properties of the

---

<sup>1</sup>CMBFAST is a widely known software for this purpose [http://lambda.gsfc.nasa.gov/toolbox/tb\\_cmbfast\\_ov.cfm](http://lambda.gsfc.nasa.gov/toolbox/tb_cmbfast_ov.cfm)

## 2. THEORETICAL FRAMEWORK IN COSMOLOGY

---

specie that composes the perturbation. For instance, in the case of dark matter perturbations, it must be specified what specific type of particles compose the perturbation, either relativistic lightweight particles (hot dark matter) or non-relativistic heavy particles (cold dark matter). In both cases the transfer function and the processed spectrum 2.65 are quite different due to the equations of state associated to each type.

In the case of adiabatic perturbations (isentropic) of cold dark matter, it can be used the next analytic approximation for the current epoch [26]

$$T_k \approx \frac{\ln(1 + 2.34q)}{2.34q} \left[ 1 + 3.89q + (1.61q)^2 + (5.46q)^3 + (6.71q)^4 \right]^{-1/4} \quad (2.66)$$

where  $q \equiv k/\Omega_0 h^2 \text{ Mpc}^{-1}$ .

The next Figure illustrates the transfer function 2.66 along with the processed power spectrum

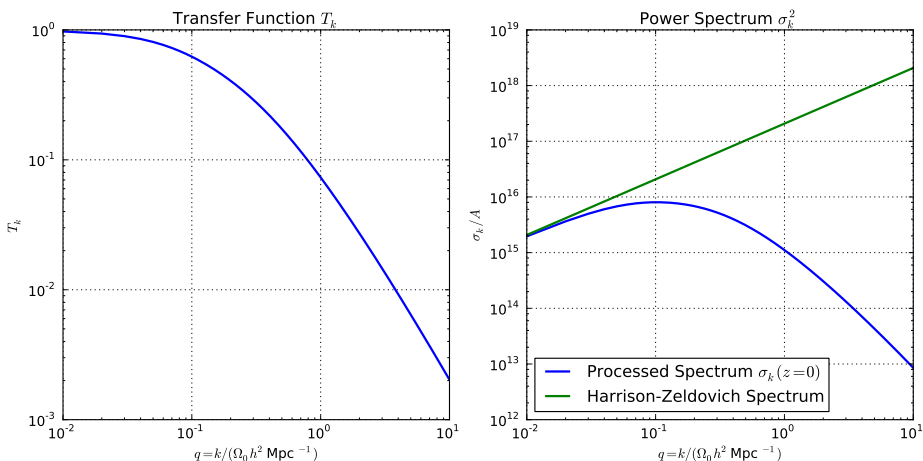


**Figure 2.7:** Transfer function for cold dark matter perturbations at the current epoch [26] (left panel). Comparison between the initial power spectrum, Harrison-Zeldovich spectrum and the processed power spectrum (right panel).

From all the formalism developed so far in this section, it is concluded that the final objective to characterize the linear regime is to obtain the transfer function, since it determines completely the evolution of the universe at early stages, where there were conditions of high isotropy and homogeneity at all the scales.

## 2.3 Non-Linear Regime of Structure Formation

In the linear regime, it is described the process of structure formation as perturbations within the isotropic and homogeneous background universe. When perturbations grow up such that  $\delta \gtrsim 1$ , the self-gravity of the modes couples strongly the local density field and invalidates the linear approximation. The physical processes associated to the non-linear regime are highly complex and even some of them are not currently well understood, this makes possible to tackle satisfactorily this problem only through numerical simulations (see chapter 3).

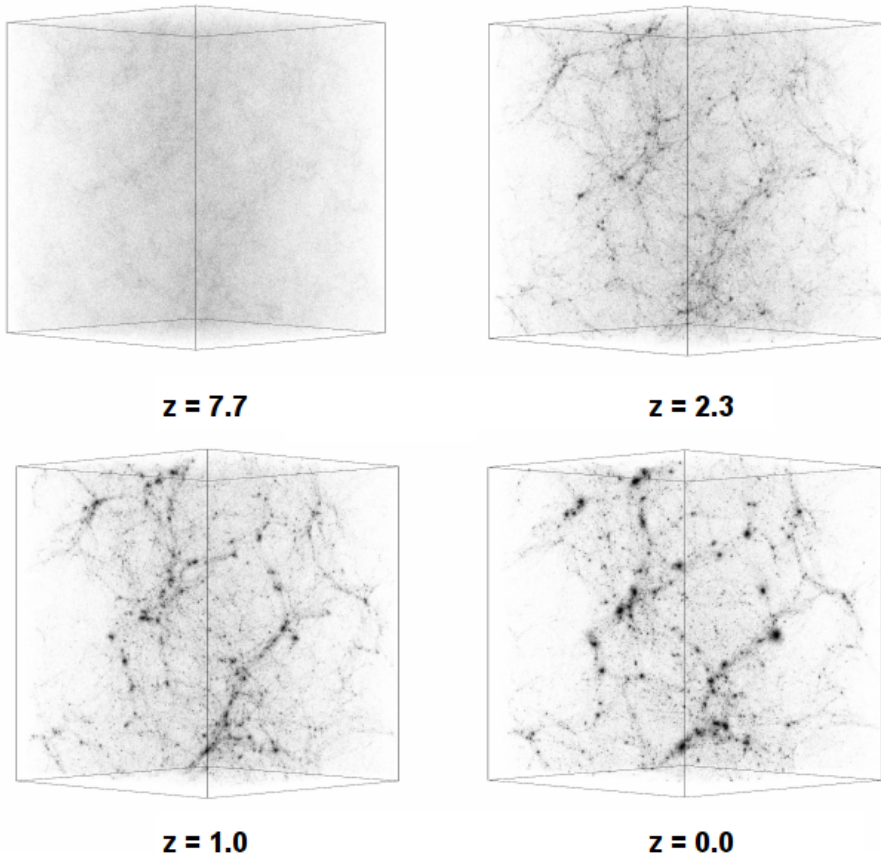


**Figure 2.8:** Evolution of a dark matter numerical simulation in a comoving volume of  $(40 \text{ Mpc}/h)^3$ , starting from a high homogeneity stage (upper left panel), until the present epoch with highly non-linear structures (lower right panel). Taken from [http://www.astro.utu.fi/research/CosmoS/lss/lss\\_p1.shtml](http://www.astro.utu.fi/research/CosmoS/lss/lss_p1.shtml)

## 2. THEORETICAL FRAMEWORK IN COSMOLOGY

---

Figure 2.8 corresponds to different stages of a dark matter numerical simulation for the non-linear universe. The Figure illustrates some emergent properties such as the anisotropy and inhomogeneity at small scales ( $\sim$  Mpc), formation and clustering of highly non-linear structures and the emergence of a web pattern at large scales (the cosmic web).

### 2.3.1 Zeldovich Approximation

In spite of the high complexity of the non-linear regime, when the perturbations of the density field are not much bigger than the background value, it is possible to perform an analytic approach to their evolution. This procedure is called the Zeldovich approximation and was developed by Yakov Zeldovich in 1970 [36]. In order to formulate this approximation, it is convenient to express again the contrast density field  $\delta(\mathbf{r})$  in terms of comoving coordinates instead of Fourier normal modes. That is because in this regime the Fourier modes are not longer independent from each other and using them does not simplify the problem, unlike the linear regime.

Using the Lagrangian frame of reference of a certain portion of the fluid, its trajectory  $\mathbf{r}_f$  can be described through the next expression

$$\mathbf{r}_f(t, \mathbf{q}) = a(t)\mathbf{r} = a(t)[\mathbf{q} + \Psi(\mathbf{q}, t)] \quad (2.67)$$

where  $\mathbf{r}$  is the comoving position of the portion of the fluid,  $\mathbf{q}$  its initial Lagrangian coordinate when the fluid is not perturbed and  $\Psi(\mathbf{q}, t)$  is the displacement function that accounts for the perturbations of the medium.

From the equation for the evolution of the contrast density field 2.39, it is possible to demonstrate that the displacement field  $\Psi(\mathbf{q}, t)$  satisfies [34]

$$\frac{\partial^2 \Psi}{\partial t^2} + 2H \frac{\partial \Psi}{\partial t} = \frac{3}{2} H^2 \Psi \quad (2.68)$$

from this, it is finally obtained

$$\Psi = \frac{3}{2} H_0^{-2} a(t) \nabla \Phi \quad (2.69)$$

### 2.3 Non-Linear Regime of Structure Formation

---

where  $\Phi$  is the effective gravitational potential associated to the density field through the Poisson's equation 2.37.

Rewriting the law of conservation of mass in terms of comoving coordinates and the initial Lagrangian coordinates, it must be fulfilled

$$\rho(\mathbf{r}, t) d^3 \mathbf{r} = \bar{\rho}(t) d^3 \mathbf{q} \quad (2.70)$$

now calculating the Jacobian  $\partial q_i / \partial r_j$  of the transformation  $\mathbf{r} \rightarrow \mathbf{q}$ , the perturbed density field can be rewritten as [27]

$$\rho(\mathbf{r}, t) = \frac{\bar{\rho}(t)}{(1 - a(t)\lambda_1(\mathbf{q})) (1 - a(t)\lambda_2(\mathbf{q})) (1 - a(t)\lambda_3(\mathbf{q}))} \quad (2.71)$$

where  $-\lambda_i(\mathbf{q})$  are the eigenvalues of the Jacobian and are sorted such that  $\lambda_1 \geq \lambda_2 \geq \lambda_3$ . Each one of these eigenvalues can be interpreted in a geometric way as an indicator of the collapse or the expansion of a portion of the fluid into the direction corresponding to the respective eigenvector, thus for example if  $\lambda_i > 0$ , that implies that the density field is collapsing locally into the direction of the eigenvector  $\mathbf{u}_i$ , whereas if  $\lambda_i < 0$  it implies an expansion into the same direction.

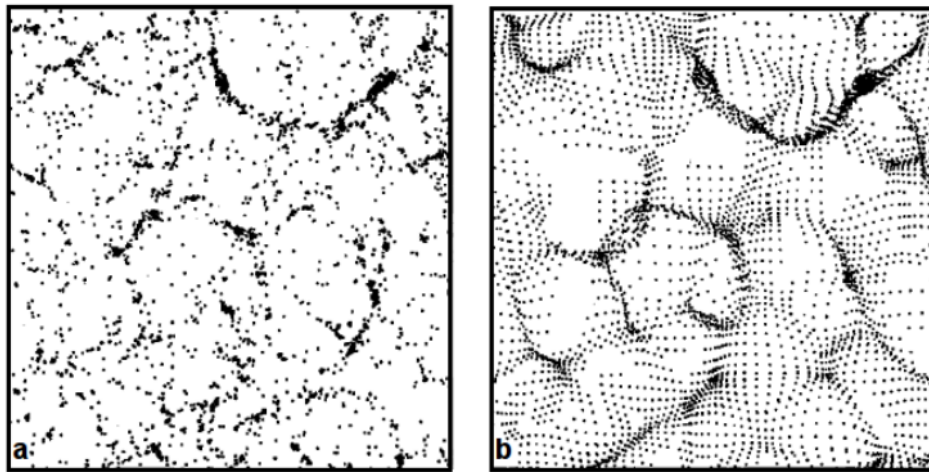


**Figure 2.9:** Comparison of the evolution in non-linear regime between a N-body simulation (a) and the Zeldovich approximation (b). In both cases are used the same initial conditions. Taken from [26].

## **2. THEORETICAL FRAMEWORK IN COSMOLOGY**

---

Finally, Figure 2.9 shows a comparison between a numerical N-body simulation and the Zeldovich approximation. It can be seen a high visual similarity of the obtained structures at the end of the evolution, thereby showing the high precision of the Zeldovich scheme. In section 3.3 it will be used the general idea proposed in the Zeldovich approximation regarding the eigenvalues of the Jacobian of the transformation, but for building classification schemes of the cosmological environment based upon the eigenvalues of other physical quantities that are more adequate for describing the local dynamics of the density field, such as the tidal tensor or the tensor of peculiar velocities.

*“All the effects of Nature are only  
the mathematical consequences of a  
small number of immutable laws”*

Pierre Simon Laplace

CHAPTER

# 3

## Computational Methods in Cosmology

In recent years, computational physics has acquired an important role in physics, allowing modelling many high-complexity systems without the necessity of recurring to experiments and/or observations. Among the methods covered by computational physics is highlighted the N-body problem since many phenomena require the computation of the interactions between a large number of bodies. Some illustrative examples of this are the modelling of molecular systems, plasma physics and specially gravitational problems in astrophysics. The development of specific methods to solve this type of problems precedes the advent of computer systems, even so, their development has powered enormously this discipline such that it is considered a new branch of physics.

In this chapter will be covered in detail some specific methods for solving gravitational problems in astrophysics, specially those related with simulations of the large-scale universe in the non-linear regime, ranging from basic algorithms to compute forces, methods to detect dark halos, to basic classification schemes for the cosmological environment.

### 3. COMPUTATIONAL METHODS IN COSMOLOGY

---

#### 3.1 N-body Simulations

Generally, the most suitable type of phenomena that can be modelled through N-body simulations is those where the interactions are strongly correlated between the constituent particles, such as long-range forces or non-local interactions. Figure 3.1 illustrates an arbitrary set of point particles which interact each other under the influence of a force field  $\mathbf{f}$ . Those conditions shape the classical formulation of the N-body problem.



**Figure 3.1:** Formulation of the N-body problem.

Assuming interactions that depends on the position<sup>1</sup>, it is obtained the below equation of movement of the  $i$ -th particle shown in the Figure 3.1 [29] [3]

$$\ddot{\mathbf{r}}_i = \sum_{j=1}^N \mathbf{f}(\mathbf{r}_i, \mathbf{r}_j) = -\nabla \phi(\mathbf{r}_i) \quad i = 1, 2, \dots, N \quad (3.1)$$

where it has been introduced the potential function  $\Phi(\mathbf{r})$ . For the case of gravitational interactions, the potential acquires the form

$$\phi(\mathbf{r}) = - \sum_{j=1}^N \frac{Gm_j}{|\mathbf{r} - \mathbf{r}_j|} \quad (3.2)$$

---

<sup>1</sup> In the generalized problem, interactions can depend on other parameters like the velocity or intrinsic degrees of freedom like the spin.

The general solution to the problem is obtained from the set  $\{\mathbf{r}_1(t), \dots, \mathbf{r}_N(t)\}$ , which is determined from the equations 3.1. For this it is necessary to implement numerical approximations due to the non-solvable (analytically) nature of the problem.

#### 3.1.1 P-P Method

The first approximation to find a solution of the equations of movement 3.1 is to compute all the  $N - 1$  interactions of the  $i$ -th particle with all of the others in a specific time  $t$  and this for  $i = 1, 2, \dots, N$ , then, from a numerical integration scheme it is calculated the positions in a discretized later time  $t + \Delta t$  and thus until a given maximum time  $t_{\max}$ . This method is called P-P (Particle to Particle) and is one of the three standard methods for solving the N-body problem.

When interactions present singularities, such as Coulombic potentials in electrostatic and gravitational problems (equation 3.2), the integration of the equation of movement is very sensitive to close encounters between particles and therefore the resolution of the time step must be increased, thereby implying a considerable increasing of the computing time. A standard solution is to introduce a softening parameter that removes these singularities, but at the cost of losing accuracy in the solution. For the gravitational potential 3.2, this leads to

$$\phi_s(\mathbf{r}) = - \sum_{j=1}^N \frac{Gm_j}{|\mathbf{r} - \mathbf{r}_j| + \epsilon_j^2} \quad (3.3)$$

where  $\epsilon_j$  is the softening parameter and can be interpreted as a measure of the physical dimension of the particle.

In spite of the high precision achieved by this method, the computing time scales as  $t_{\text{comp}} \propto N^2$ , what makes it highly non-viable to apply for a large number of particles (generally  $N \gtrsim 10^4 - 10^5$  [27]). For simulations of planetary systems, computation of orbits of minor bodies and studies of star clusters dynamics, this methods is good enough, but for cosmology and galaxy astrophysics, where the number of implicated particles must be the maximum possible in order to reproduce the real continuous nature of the matter distribution, it becomes necessary to develop methods lesser computational cost.

### 3. COMPUTATIONAL METHODS IN COSMOLOGY

---

#### 3.1.2 PM Method

A second scheme used for solving the N-body problem is the PM scheme (Particle Mesh) [5], this consists of determining a continuous distribution for the density field from the position and the mass value of each particle, for this it is divided the space of the simulation into a grid of  $M \times M \times M$  cells and then a count of particles per cell is made in order to associate a specific mass value and therefore a density to each cell. An illustrative diagram is shown in Figure 3.2

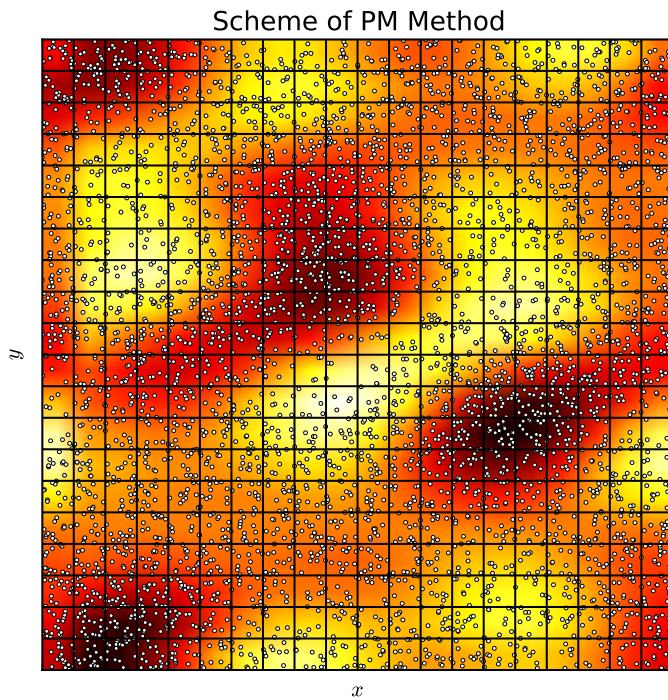


**Figure 3.2:** Illustrative diagram of the PM method. The map that is plotted over the distribution of particles corresponds to the density field evaluated in each cell of the grid. Dark cells corresponds to overdensity regions whereas white cells to lower values of the density field, which agrees with the amount of mass of the particles per cell.

### **3.1 N-body Simulations**

---

The method can be summarized into the next steps

1. From the grid established over all the simulation, it is calculated a continuous density field  $\rho(\mathbf{r})$ , interpolating the value between adjacent cells.
2. Once it is obtained the density field, it is calculated the potential of the equation of movement 3.1 by using the Poisson's equation

$$\nabla^2 \phi = 4\pi G \rho \quad (3.4)$$

In order to reach this, it is usually used integration schemes based upon Fourier transform, such as the Fast Fourier Transform (FFT).

3. Finally, using the previous potential field, it is calculated the position of each particle in the next discrete time  $t + \Delta t$ , and it is repeated over and over again until a given final time.

This method is less precise than the direct sum, but it is possible to demonstrate that the computing time scales as  $t_{\text{comp}} \propto N + M \log M$ , with an asymptotic behaviour as  $t_{\text{comp}} \propto N$  for high resolutions  $M$  of the grid and as  $t_{\text{comp}} \propto N$  for low resolutions [29]. In any case, its efficiency is much better than the PP method 3.1.1 when the number of particles of the simulation is large enough  $N \ll 10^4 - 10^5$ , which makes this method very useful to tackle problems with a large number of particles.

However, there are some pathological situations where this method can not be applied satisfactory [29].

- Highly non-homogeneous distributions of particles.
- Strongly correlated systems.
- Systems with non-trivial geometries.

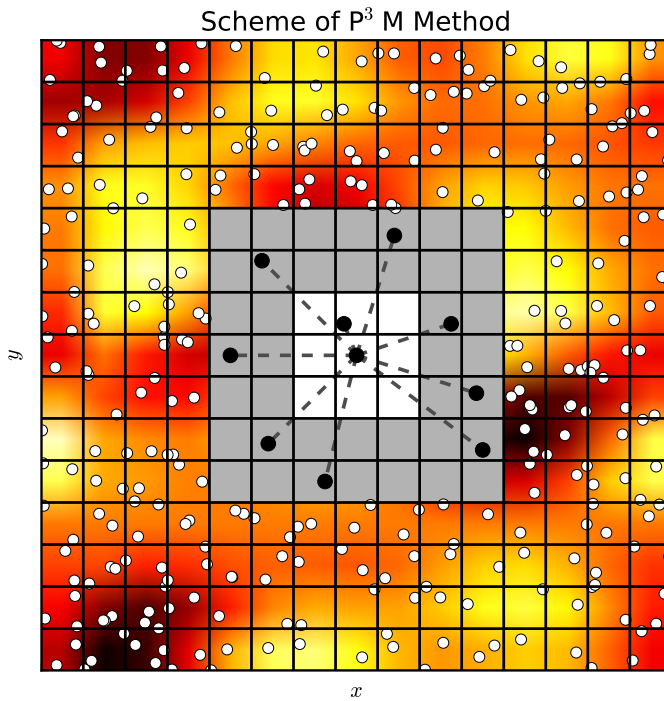
Because those conditions are satisfied in the non-linear universe, like strong gravitational couplings for modes of the density field after  $z \gtrsim 8$ , this methods is not very useful for solving the late universe.

### 3. COMPUTATIONAL METHODS IN COSMOLOGY

---

#### 3.1.3 P<sup>3</sup>M Method

The last of the three standard scheme for solving N-body simulations is the P<sup>3</sup>M method (PP + PM) [15]. This method can be thought as a combination of the previous methods, making the most of each one of them.



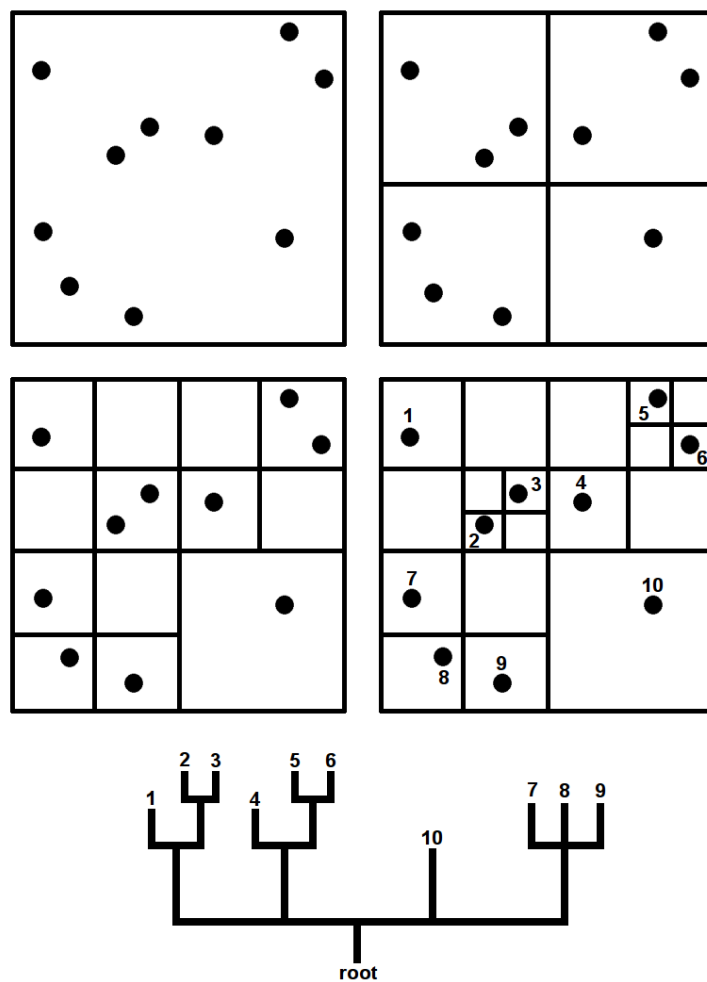
**Figure 3.3:** Illustrative diagram of the P<sup>3</sup>M method. For the reference particle, shown in the center, interactions with distant particles is calculated through the PM method, whereas for close particles (gray and white regions), the interaction is calculated by using the PP method.

Figure 3.3 illustrates the P<sup>3</sup>M method. For each one of the integration step of the system, it is calculated a hierarchical grid for each particle. Hierarchies are defined with respect to the relative distance between particles and they determines which approximation should be used for computing the equation of movement. For close particles (first hierarchy) it is used the PP method, what allows tackling strong local correlations and highly non-homogeneous regions. Interactions with

### 3.1 N-body Simulations

---

particles embedded into the next hierarchies are calculated by decomposing the potential field into its multipolar terms, i.e. the second hierarchy corresponds to the dipolar contribution of the potential (if applicable), and so on. Finally for more distant cells (last hierarchy), it is used the PM scheme, interpolating the density field and solving the Poisson's equation 3.4 for the potential.



**Figure 3.4:** An illustrative example of the building of a tree code for a N-body simulation. Upper panels show the iterations for a 2D problem whereas lower panel illustrates the resultant tree built using each particle of the simulation.

### 3. COMPUTATIONAL METHODS IN COSMOLOGY

---

One of the main disadvantages of this method lies in the building of the hierarchical structure for evaluating which scheme must be used. The original scheme, proposed simultaneously by [1] [21] and [30], has some inconsistencies produced by the lack of physical basis in the building of the hierarchical structure [29].

A better physically based method for constructing the hierarchical structure of a N-body simulation is the so-called octant tree code. It was initially developed by [2]. In this algorithm, the space of the simulation is embedded into a cubic volume denominated *root*, then this volume is divided into 8 regions of equal size which are denominated octant, these are the first hierarchy of the tree. This procedure is repeated recursively until each cell or octant has only one particle inside, thereby constructing a set of hierarchies that determines the neighbourhood of all the particles of the simulation. Figure 3.4 illustrates the iterations needed in order to construct the tree of a simulation (with the aim of simplicity, it is 2D). The lower panel of the same figure shows the structure of the tree. In this way it is possible to compute, for instance, the interaction between particles 7, 8 and 9 by using direct sum, because they are the closer neighbours each other, whereas the interaction with other particles that belong to other branches is calculated through multipolar expansion or the PM scheme.

## 3.2 Types of Simulations

Using the methods above described, it is possible to carry out simulations of the late universe in the non-linear regime and studying its behaviour numerically. Because in the non-linear regime all the large-scale astrophysical processes are dominated mainly by dark matter, it is usual not considering the contribution of other components like radiation or baryonic matter, furthermore, including the different physical processes dominated by these other contributions would increase considerably the computing time of the simulation without much profit regarding physical understanding. This specific type of simulations is called *dark matter simulations*.

In this subsection are shown the dark matter simulations that are used throughout this work, moreover they are classified with respect to the adopted criterion for setting the initial conditions, thus, simulations can be unconstrained when the initial conditions are set in a completely random way, or constrained when they are

## 3.2 Types of Simulations

---

chosen such that they satisfy some conditions fixed a priori like observational constraints or reproducing the very local structure ( $\sim 10 \text{ Mpc}/h$ ) of the real universe.

### 3.2.1 Unconstrained Simulations (*Bolshoi*)

Since the evolution of the universe in the linear regime is well-known through the transfer function (see section 2.2), dark matter cosmological simulations are only used for studying the non-linear regime, however it is necessary to establish a set of initial conditions in order to evolve the system properly. Generally these conditions are determined from computing the linear regime, so that it is required another set of primordial conditions for the homogeneous background density field. Because of that, the last set will be henceforth called simply the initial conditions.

As has been mentioned in the subsection 2.2.3, the statistical properties of the initial density field correspond to a Gaussian distribution of the Fourier modes with a Harrison-Zeldovich power spectrum, which agrees with the inflationary model and cosmological observations (see subsection 1.3). The modes of the density field  $\delta_{\mathbf{k}} = r_{\mathbf{k}} e^{i\phi_{\mathbf{k}}}$  follow then the distributions given by the equation 2.57

$$P_r(r_{\mathbf{k}})dr_{\mathbf{k}} = \exp\left(-\frac{r_{\mathbf{k}}^2}{\sigma_k^2}\right) \frac{2r_{\mathbf{k}}dr_{\mathbf{k}}}{\sigma_k^2} \quad (3.5)$$

$$P_{\phi}(\phi_{\mathbf{k}})d\phi_{\mathbf{k}} = \left(\frac{1}{2\pi}\right) d\phi_{\mathbf{k}} \quad (3.6)$$

The unconstrained nature of this type of simulations lies in the randomness of the phases  $\phi_{\mathbf{k}}$  according to the distribution 3.6, without any kind of observational constraint for the final stage of the simulation.

*Bolshoi* is a cosmological simulation of the large-scale universe with unconstrained initial conditions, the official website of the project is <http://hipacc.ucsc.edu/Bolshoi/>.

### 3. COMPUTATIONAL METHODS IN COSMOLOGY

---

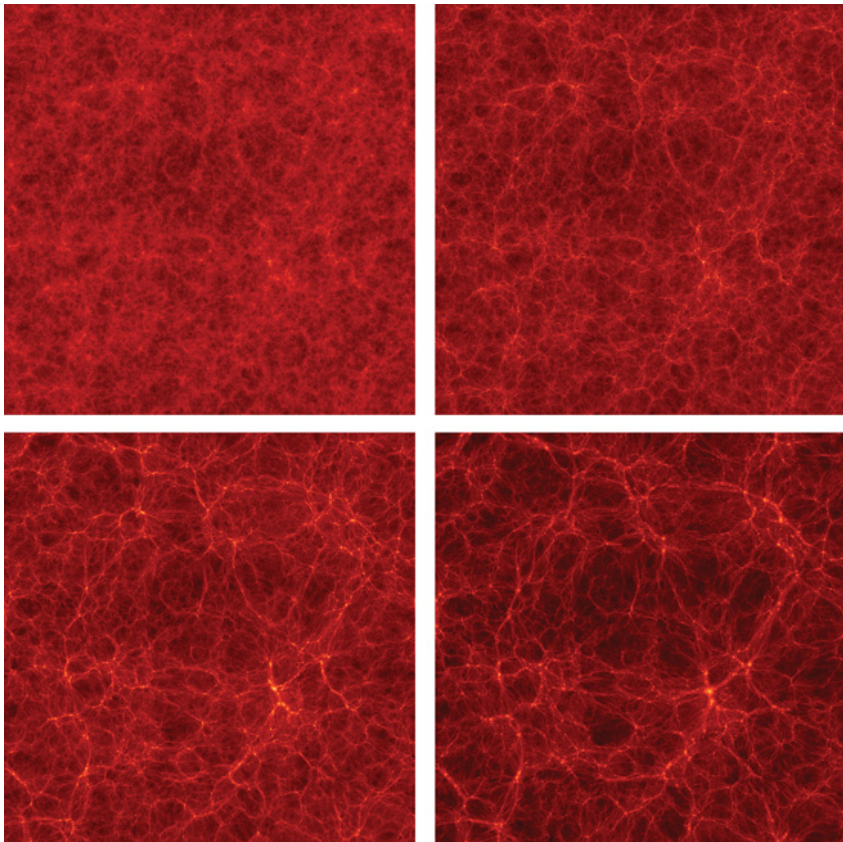


**Figure 3.5:** Evolution of the Bolshoi simulation. It is illustrated the density field in a rectangular volume of  $16 \text{ Mpc}/h$  of thick and  $250 \text{ Mpc}/h$  of side for different stages of the evolution.  $z = 9.5$  (upper left),  $z = 3$  (upper right),  $z = 1$  (lower left) y  $z = 0$  (lower right). Taken from <http://spectrum.ieee.org/aerospace/astrophysics/the-cosmological-supercomputer>

Due to its larger comoving size compared to constrained simulations (a cubic volume of  $250 \text{ Mpc}/h$ ), Bolshoi is used for obtaining the fine-grained statistics for the results computed in the chapter 4. The cosmological model used in this simulation is the WMAP7 universe (see table 1.1), the number of particles used is  $2048^3$ , what implies a mean mass per particle of  $1.35 \times 10^8 h^{-1} \text{ M}_\odot$ . More precise and technical information about can be consulted in [23].

#### 3.2.2 Constrained Simulations (CLUES)

As has been mentioned in the chapter 2, the standard way to compare the results produced by cosmological simulations and observations is through the statistical properties of the distributions, such as the two-point correlation functions or the power spectrum. In spite of that, some studies require more detailed description of the local universe in a cosmological context. Due to technical issues, like the direct measuring of the dark matter distribution or the lack of data in high redshifts, it is necessary to appeal to cosmological simulations that reproduce properly the local universe. One of the first work aimed to reproduce the local universe is [22]. Here it is reproduced our local group of galaxies along with the local supercluster and the Virgo cluster.

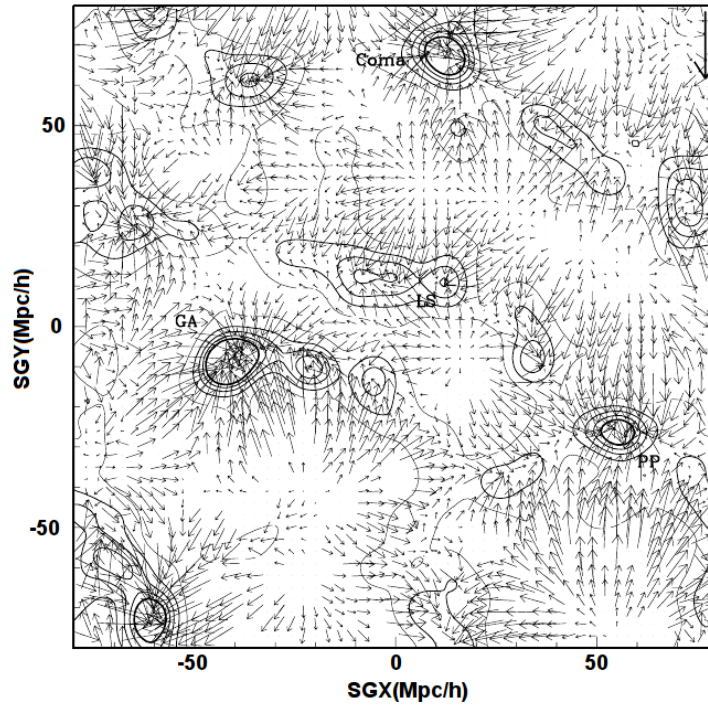


**Figure 3.6:** Initial density and peculiar velocity field built by using constraints in order to reproduce the local environment at a scale of  $160 h^{-1}\text{Mpc}$ . Some of the identified structures are: *Coma*, coma cluster, *PP*, Perseus-Pisces supercluster, *LS*, local supercluster, *GA*, the great attractor. The upper arrow indicates the scale of the peculiar velocities field as 1000 km/s. Taken from [22].

### 3. COMPUTATIONAL METHODS IN COSMOLOGY

---

The method proposed by [22] and [16] consists in building the initial density and peculiar velocities field from surveys of radial velocities and redshifts (see section 1.3). For the treatment and reduction of noise and measuring errors of data, it is used a Bayesian method, Wiener filters (for more detailed information, see [35]). At small scales, this method is limited because the applied filters suppress some modes in the initial power spectrum and therefore they must be generated randomly according to the Gaussian distribution 2.57 in order to guarantee consistency with the standard cosmological model. Figure 3.6 illustrates the initial conditions obtained by this method for the local universe at a scale of  $160 h^{-1}\text{Mpc}$ .

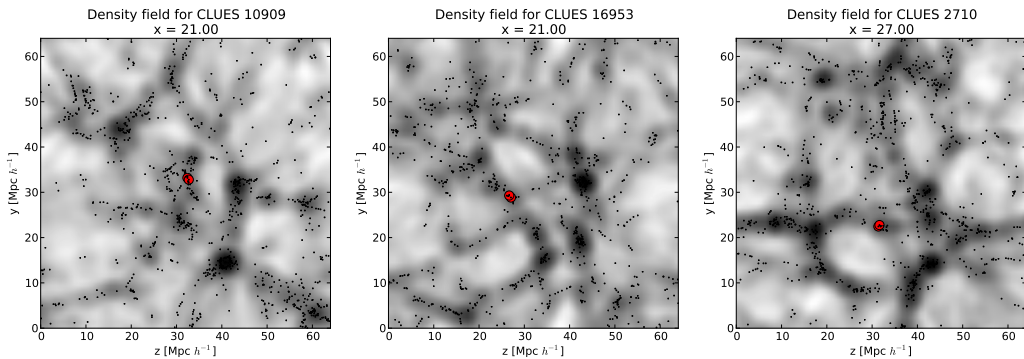


**Figure 3.7:** Three constrained simulations of the CLUES project where it is possible to identify systems like the local group. It is illustrated the density field of each simulations along with the dark matter halos (black points), and the LG-like systems found (red points).

**CLUES** (Constrained Local UniversE Simulations) is a project aimed to reproduce the local universe with the best resolution up to date. The official webpage of the project is <http://www.clues-project.org>. In this simulations, initial conditions are built by using the Hoffman-Ribak algorithm [16] for reproducing a comoving volume of  $(64 h^{-1}\text{Mpc})^3$ . Due to the unconstrained nature of initial conditions at small scales ( $\sim 5 h^{-1}\text{Mpc}$ ), it becomes necessary to carry out 200 different simulations, of which only 3 are successful regarding the imposed observational constraints (see Figure 3.7). For the evolution it is used the package

### 3.2 Types of Simulations

GADGET<sup>1</sup> with  $1024^3$  particles of dark matter and a cosmology consistent with the WMAP7 (see table 1.1). More technical details and further information of the project can be found in [12].

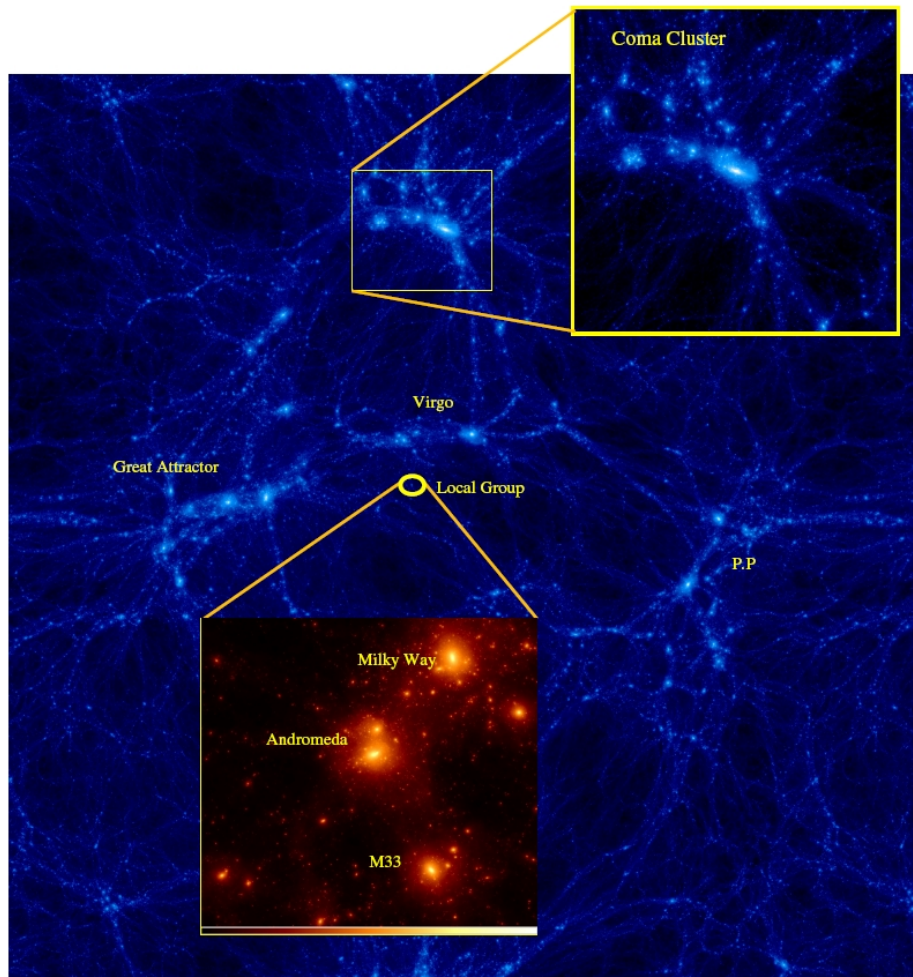


**Figure 3.8:** An example of a simulation of the CLUES project. In this figure it is shown the large-scale structures of the local universe and it can be appreciated clearly the most significant members of the Local Group. Taken from the official webpage of the project <http://www.clues-project.org>

<sup>1</sup> GADGET2 is a very popular code for N-body simulations developed by Volker Springel. It is available for free download in the official webpage of the project <http://www.mpa-garching.mpg.de/gadget/>

### 3. COMPUTATIONAL METHODS IN COSMOLOGY

---

## 3.3 Environment Characterization

Once obtained the numerical simulations for the evolution of the universe in non-linear regime, one of the main objectives is to characterize the emergent structures typical of this regime. Among these structures, it is highlighted the cosmic web, which is constituted by regions of different dimensionality, where vast void regions are limited by planar regions, these are, in turn, limited by one-dimensional filaments which joint to form high density point regions.

From cosmological observations, it has been possible to establish the relation between the properties of halos, such as the spin parameter, the concentration, the shape, etc. And the host environment. Because of this, it is important to quantify the structure of the cosmic web in cosmological simulations. One of the pioneer works in quantifying the cosmic web was the Zeldovich approximations discussed in subsection 2.3.1), later schemes use stratifications in the density field in order to quantify the environment, these schemes are called geometric methods, but due to their local nature, they cannot give account of global properties like large-scale matter streams or the influence of large neighbouring structures. In this section is shown two recently developed classification schemes.

### 3.3.1 T-web Scheme

The first of these methods was proposed by [13] and it consists in using the theory of dynamical systems in order to perform an analysis of the local stability of test orbits around dark matter halos, thereby quantifying their environment for a set time (or set redshift). For this, the Newtonian approximation is assumed to be correct (see subsection 2.2.1) and the equation of movement of a test particle embedded into a peculiar potential of the distribution is

$$\ddot{\mathbf{r}} = -\nabla\phi(\mathbf{r}) \quad \text{con} \quad \nabla^2\phi = 4\pi G\bar{\rho}\delta \quad (3.7)$$

It is reasonable to assume that in the center of mass  $\bar{\mathbf{r}}_i$  of each halo there is a minimum of the potential, i.e.  $\nabla\phi = 0$ , thereby forming a local potential well. This allows linearizing the equation of movement 3.7 around these points, obtaining

$$\ddot{r}_i = -T_{ij}(\bar{r}_i)(r_j - \bar{r}_{k,j}) \quad (3.8)$$

where it is defined the tidal tensor as the Hessian matrix of the peculiar potential

$$T_{ij} \equiv \frac{\partial^2 \phi}{\partial r_i \partial r_j} \quad (3.9)$$

According the theory of dynamical systems, a negative eigenvalue indicates an unstable point in the direction of the respective eigenvector, thereby implying an outward flux of matter. For positive eigenvalues, it is presented a completely analogous situation. Base upon the Zeldovich approximation (see subsection 2.3.1), it is proposed a classification scheme for the cosmological environment from the eigenvalues of the tidal tensor  $T_{ij}$  (see Figure 3.9).

- **Vacuum:** in this case, the three eigenvalues are positive, thereby indicating an expansion into all directions of space.
- **Sheet:** in this case  $\lambda_1 \geq \lambda_2 > 0$  and  $\lambda_3 < 0$ , thereby implying an one-dimensional collapse, and leading to a region with a planar local geometry.
- **Filament:** for this type of regions, only the value of  $\lambda_1$  is positive, implying a collapse into two directions and an expansion into the other one, thereby forming a region with a linear geometry.
- **Knot:** finally, for this type of region, the three eigenvalues are negative, so there is a collapse into all the directions, leading a highly compressed zone.

The most remarkable of this scheme compared to geometric methods is its dynamical nature, since it allows differentiating regions with the same density value but with different stability properties. In spite of the latter, assuming a local minimum is only justified in the center of each halo, therefore it is meaningless to generalize this scheme for any other region of the space. Another inconvenient is that, according to the original scheme, using the sign of each eigenvalue instead of using the threshold value, it is not reproduced the visual impression obtained from the dark matter distribution of the simulations (see Figure 3.10).

### 3. COMPUTATIONAL METHODS IN COSMOLOGY

---

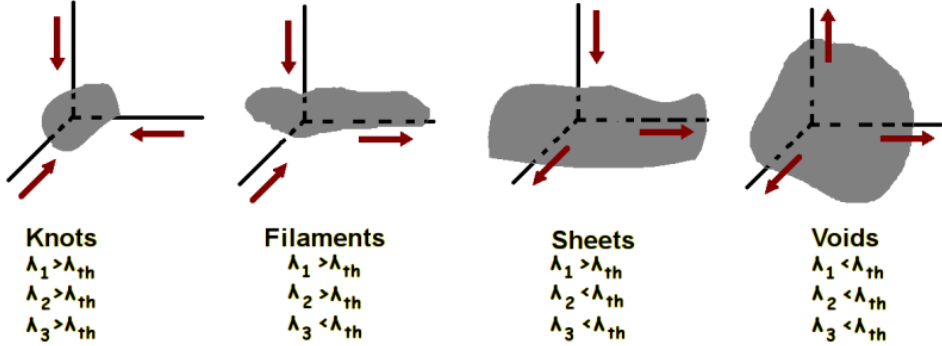


**Figure 3.9:** Classification scheme for the cosmological environment for both T-web and V-web schemes. The threshold value  $\lambda_{th}$  is taken as free parameter.

A significant improvement of this method is reached by generalizing the classification scheme respect to a certain threshold value  $\lambda_{th}^T$ , which is taken as a free parameter and is adjusted according to the visual impression obtained [7]. Specifically, the original scheme is recovery by setting  $\lambda_{th}^T = 0$ .

#### 3.3.2 V-web Scheme

The second dynamical scheme to classify the cosmic web presented in this chapter is due to [17] and it is based upon the peculiar shear velocity tensor

$$\Sigma_{ij} = -\frac{1}{2H_0} \left( \frac{\partial v_i}{\partial r_j} + \frac{\partial v_j}{\partial r_i} \right) \quad (3.10)$$

analogously to the T-web scheme, the eigenvalues of the tensor  $\Sigma_{ij}$  are calculated and the environment is defined according to a threshold value  $\lambda_{th}^V$  (see Figure 3.9).

As it has been demonstrated by [17], in the linear regime both tensors  $T_{ij}$  and  $\Sigma_{ij}$  are proportional, therefore both schemes are completely equivalent in this time. This fact is partially evidenced through the visual impression obtained for both schemes from the large-scale structure in the Bolshoi simulation (see Figure 3.10), and that is due to the linearity of individual Fourier modes at very large scales.

For small modes, where non-linear effects are more dominant, both schemes differ significantly, as it can be seen in the visual impression of the CLUES simulations. Specifically, the V-web scheme quantifies in a more precise way the fine

### 3.3 Environment Characterization



**Figure 3.10:** It is illustrated for each one of the simulations (CLUES 1, CLUES 2, CLUES 3, Bolshoi) the difference between both classification schemes, T-web and V-web, and for different threshold values  $\lambda_{th}$  (Black - Knot, Dark gray - Filament, Gray - Sheet, White - Vacuum). In the upper figures it is shown the visual impression obtained from the respective density fields ( $\log(\delta + 1)$ ), these impressions are used to calibrate the threshold value  $\lambda_{th}$ . The resolution of the used grid in each simulation is approximately  $1.0h^{-1}$  Mpc/cell and for each one it is performed a Gaussian softening of one cell size. The width of each slide is one cell.

### **3. COMPUTATIONAL METHODS IN COSMOLOGY**

---

structure of the cosmic web at small scales, thereby allowing defining a more appropriate environment for cosmologically small structures like dark matter halos or small groups of them.

Another advantage of the V-web scheme regarding the T-web is because the V-web is based upon the shear velocity field instead of the density field, thereby giving more information about the dynamic of the local environment and making possible to quantify more directly non-local effects, like fluxes of matter or the influence of neighbour structures. Because of this, this scheme will be adopted as standard for quantifying the environment of halos and pairs (Local Group-like systems) and statistical distributions of the cosmic environment in the chapter 4.

## **3.4 Detecting Halos and Defining the Samples**

Once the cosmological environment has been characterized, the next step is to find the structures formed in the simulations, specifically dark matter halos. Due to the continuous nature of the matter distribution of the universe, it is complicated and subjective to define discrete and spatially limited structures, like dark matter halos and the embedded galaxies within them. In spite of this, the rough nature of numerical solutions requires a priori discretization of the density field through point particles with an associated representative mass (generally in the order of  $10^7 \sim 10^9 h^{-1} M_\odot$ , though this depends specifically on the resolution of the simulation). The latter implies that the selection of discrete physical structures<sup>1</sup> is reduced to find clusters of particles which represents these systems.

### **3.4.1 FOF Method**

One of the most used methods for detecting structures in N-body simulations is the FOF (Friend of Friend method).

---

<sup>1</sup> In spite of the particles that maps the density distribution have also a discrete nature, their individuality lacks of physical sense and it is only a consequence of the used numerical schemes.

### 3.4 Detecting Halos and Defining the Samples

---

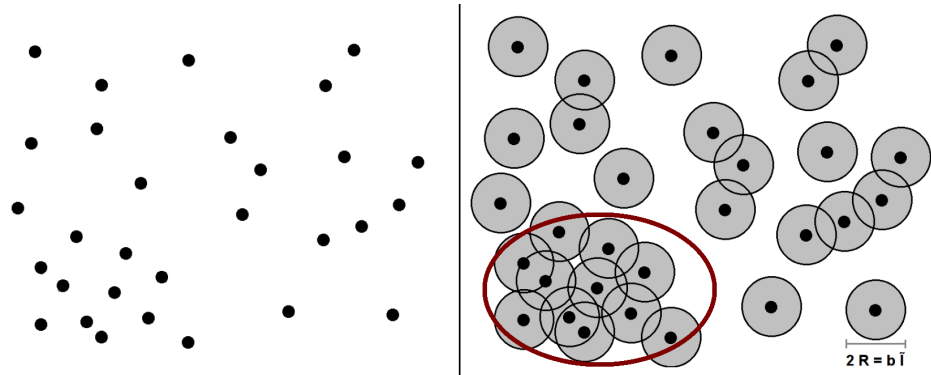


**Figure 3.11:** Illustrative diagram of the FOF method. Gray circles around each particle represents the linking region and the red curve represents one of the bounded structures found by the method.

In this method, it is associated a finite volume to each particle which is called the linking region. Once defined these volumes, the structures are found by detecting intersections between them. An illustrative example is shown in the Figure 3.11, where the structure enclosed by the red curve, corresponding to a dark matter halo, is made of the 11 adjacent linking regions which intercept each other. The geometry of the linking regions is generally spherical, with a radius  $R_i$  given by the next expression

$$R_i = \frac{1}{2}b \bar{l} \quad (3.11)$$

where  $b$  is the linking parameter and  $\bar{l}$  the mean free path of the particles of the simulation. The linking parameter  $b$  is free and depends on each simulation particularly, being given a priori before the construction of the catalogue of halos.

Figure 3.12 shows the result of applying the FOF method to construct a catalogue of halos for the CLUES 3 simulation. The distribution of the halos is in accordance with the density distribution (see Figure 3.10), following the same pattern of filaments and knots that the cosmic web. In the subsection 3.4.2 the defined samples of halos in each simulation are built by using this scheme, with a linking parameter  $b = 0.17$ .

### 3. COMPUTATIONAL METHODS IN COSMOLOGY

---

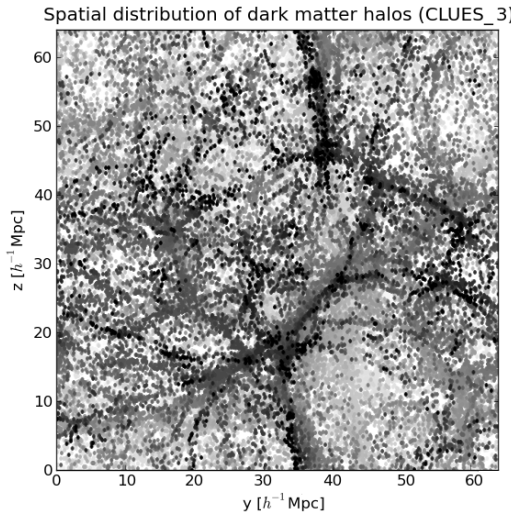


**Figure 3.12:** Halos detected by using the FOF scheme for one of the CLUES simulations. The color gradient indicates the depth with respect to the  $x$  axis, where black point are the nearest halos.

#### 3.4.2 Definición de Muestras

En esta subsección se presentan las diferentes muestras definidas que serán usadas en el capítulo 4 para la determinación de los efectos del entorno en los sistemas de grupos locales y la caracterización de cada simulación. Estas corresponde a una versión ampliada de las muestras definidas en [8].

- **Halos Generales (GH):** estos corresponden a todos los halos hallados en las simulaciones a partir del esquema FOF, independiente de su rango de masa.
- **Halos Individuales (IH):** son un subconjunto de la anterior muestra, y representan todos los halos de materia oscura que están en el rango de masas  $5.0 \times 10^{11} h^{-1} M_{\odot} - 5.0 \times 10^{12} h^{-1} M_{\odot}$ . Este rango de masa es escogido debido a que corresponde al rango en el cual se forman galaxias de disco, tal como los principales miembros del grupo local, Andrómeda y la Vía Láctea.
- **Pares (P):** esta es construida a partir de la muestra *IH* y está compuesta por pares de halos que satisfacen el criterio de ser mutuamente el halo más

### **3.4 Detecting Halos and Defining the Samples**

---

cercano al otro. Se construye como una muestra primigenia para encontrar sistemas de pares aislados y similares al grupo local.

- **Pares Aislados (*IP*):** esta muestra se construye a partir de los sistemas en la muestra de pares que además satisfacen las siguientes condiciones [8] [9].

- La distancia entre el centro de los halos debe ser menor a  $0.7h^{-1}$  Mpc, consistente con la distancia entre la Vía Láctea y Andrómeda.
- La velocidad radial relativa entre ambos halos debe ser negativa.
- No debe haber ningún objeto más masivo que alguno de los dos halos a una distancia menor que  $2.0h^{-1}$  Mpc de ambos.
- No debe existir ningún objeto más masivo que  $5.0 \times 10^{13}h^{-1} M_{\odot}$  a una distancia menor que  $5h^{-1}$  Mpc respecto a ambos halos.

Estas condiciones garantizan el aislamiento de los pares respecto a la influencia gravitacional de estructuras mayores y otros halos

- **Grupos Locales (*LG*):** esta muestra es definida en las simulaciones CLUES y corresponde a los pares de halos construidos a priori para la reproducción del grupo local. Por definición, solo existe un sistema *LG* por cada una de las tres simulaciones CLUES.
- **Grupos Locales Construidos (*CLG*):** con el objetivo de obtener una muestra de sistemas tipo *LG* en simulaciones no restringidas, se propone un método de construcción basado en el entorno cosmológico de la muestra *LG* en las simulaciones CLUES (ver figura 3.13). Para esto se calculan los 3 campos de autovalores del *shear velocity tensor* en una malla con resolución de  $1.0h^{-1}$  Mpc/celda y un suavizado Gaussiano de una celda. En la siguiente tabla se tabulan los valores obtenidos para los autovalores del entorno de los sistemas *LG*.

Finalmente, a partir de los autovalores extremos hallados se define la muestra *CLG* como aquellos pares *IP* cuyos autovalores de entorno asociados se encuentran en el intervalo fijado. Para garantizar autoconsistencia, esta muestra también es definida en las simulaciones CLUES.

### 3. COMPUTATIONAL METHODS IN COSMOLOGY

---

Descripción	$\lambda_1 [10^{-1}]$	$\lambda_2 [10^{-1}]$	$\lambda_3 [10^{-1}]$
CLUES 1 H1	1.82	1.20	-1.59
CLUES 1 H2	1.82	1.20	-1.59
CLUES 2 H1	1.78	$9.54 \times 10^{-1}$	$-8.85 \times 10^{-1}$
CLUES 2 H2	2.19	$4.45 \times 10^{-2}$	-1.29
CLUES 3 H1	3.23	$-6.29 \times 10^{-2}$	-1.98
CLUES 3 H2	3.49	1.21	-1.29
Valor mínimo	1.78	$-6.29 \times 10^{-2}$	-1.98
Valor máximo	3.49	1.21	$-8.85 \times 10^{-1}$

**Table 3.1:** Autovalores asociados al entorno de cada grupo local en las simulaciones CLUES.

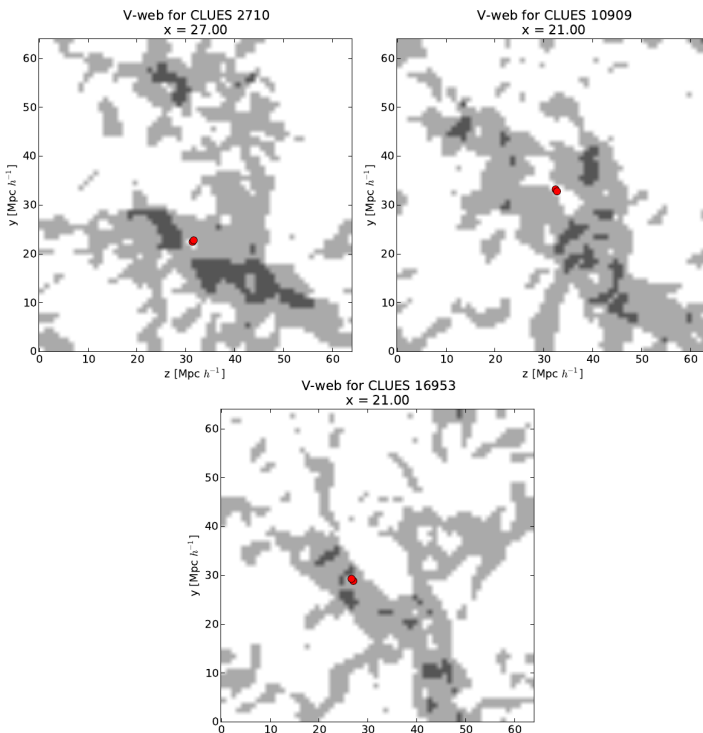


**Figure 3.13:** Entorno cosmológico a partir del esquema V-web (con  $\lambda_{th} = 0.3$ ) para cada uno de los LG de las simulaciones CLUES, indicados por los puntos rojos.

### 3.4 Detecting Halos and Defining the Samples

---

Muestra	CLUES 1	CLUES 2	CLUES 3	Bolshoi
<i>GH</i>	56632	57707	56799	432000
<i>IH</i>	1493	1490	1493	88068
<i>P</i>	386	380	387	23037
<i>IP</i>	20	12	18	1256
<i>LG</i>	1	1	1	–
<i>CLG</i>	1	2	3	30

**Table 3.2:** Tamaños de las muestras definidas para cada una de las simulaciones.

Para finalizar, en la tabla 3.2 se tabula el tamaño de cada una de las muestras definidas para cada simulación. Puede notarse que los tamaños escalan aproximadamente en la misma proporción que el volumen entre las simulaciones ( $1/60$  – CLUES /Bolshoi). En especial la muestra *CLG* para Bolshoi tiene un tamaño proporcional a la muestra *LG* de las CLUES, indicando que el esquema de construcción propuesto reproduce sistemas tipo LG en simulaciones no restringidas.

#### 3.4.3 Método de Detección de Pares

A continuación se describe el algoritmo desarrollado para la detección de cada una de las muestras de pares en cada simulación (*Pair Finder*)<sup>1</sup>.

- Se partitiona el espacio de la simulación en  $N \times N \times N$  celdas, luego para cada celda se realiza un indexado de los halos que están dentro de ella, almacenando los identificadores de cada uno de ellos.
- Posteriormente, para cada una de las celdas se identifican los primeros vecinos, teniendo en cuenta condiciones de frontera periódicas, tal como la celda  $i$  en la figura 3.14.
- Para un halo de una celda dada se calcula la distancia a todos los halos de la misma celda y de las celdas vecinas, luego se almacena la distancia al halo más cercano, la distancia al halo más cercano con una masa mayor y la distancia al halo más cercano con una masa mayor a  $5.0 \times 10^{13} h^{-1} M_{\odot}$ .

---

<sup>1</sup>Una versión actualizada del código puede encontrarse en [https://github.com/sbustamante/Thesis/tree/master/codes/Halo\\_Finder](https://github.com/sbustamante/Thesis/tree/master/codes/Halo_Finder)

### 3. COMPUTATIONAL METHODS IN COSMOLOGY

---

- Repitiendo el anterior paso para todos los halos, si dos halos son mutuamente los dos más cercanos, estos se catalogan como un par, construyendo así la muestra  $P$  definida en la subsección anterior 3.4.2.
- Finalmente, para cada uno de los sistemas de pares se evalúan las condiciones definitorias de los  $IP$ , determinando así esta muestra.

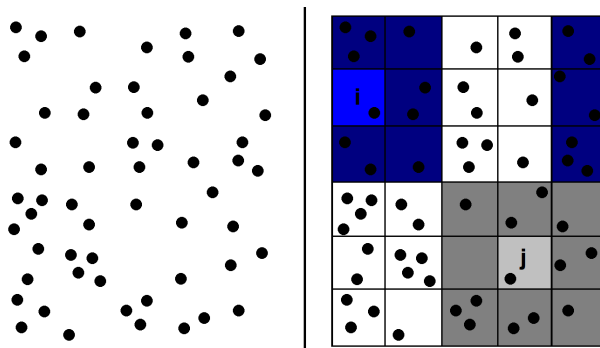


**Figure 3.14:** Ilustración 2D del método para la detección de las muestras de pares. Distribución de halos de materia oscura (izquierda), definición de zonas (derecha).

La eficiencia de este método radica en que evita evaluar distancias entre todos los halos de la simulación, siendo necesario solo para los vecinos cercanos. La estructura de celdas lo hace similar a un código de árbol (ver subsección 3.1.3), a excepción de la estructura jerárquica de este último. En principio, el código debe ser más eficiente a medida que se aumenta la resolución  $N$  de la malla, pero existen dos limitaciones que a esto. La primera tiene que ver con el número de halos por celda, este no puede ser demasiado grande, pero tampoco puede ser tal que solo hallan unos pocos halos por celda<sup>1</sup>. La segunda limitación tiene que ver con las condiciones de distancia usadas en la definición de la muestra  $IP$ , el tamaño físico de cada celda no puede ser menor a ninguna de estas distancias.

---

<sup>1</sup>Este umbral no es bien definido y depende de cada simulación, por ejemplo para las simulaciones usadas (Bolshoi y CLUES), un valor de  $N = 8$  es generalmente adecuado.

*“Lo más incomprendible de nuestro universo es que sea comprensible”*

Albert Einstein

CHAPTER

# 4

# El Entorno Cosmológico y el Grupo Local

A continuación son presentados los resultados obtenidos a partir de las simulaciones descritas en el capítulo anterior 3 para la dependencia de las propiedades de los sistemas tipo grupo local respecto al entorno cosmológico en el que están embebidos. Se caracteriza primero cada una de las simulaciones usadas (CLUES y Bolshoi) con el fin de garantizar concordancia entre las cosmologías que representan y entre las distribuciones de entorno (sección 4.1). Después de esto, en la sección 4.2 se determinan las propiedades físicas y estadísticas de cada una de las muestras definidas en 3.4.2 y se analizan las correlaciones existentes entre las propiedades calculadas y el entorno cosmológico de cada simulación.

## 4.1 Propiedades de las Simulaciones

Uno de los principales objetivos para determinar la influencia del entorno sobre sistemas tipo grupo local es construir una muestra *CLG* en simulaciones no restringidas y así obtener estadística significativa. Para garantizar la consistencia de esta muestra es necesario establecer la equivalencia entre las distribuciones

## 4. EL ENTORNO COSMOLÓGICO Y EL GRUPO LOCAL

---

de halos oscuros y analizar las distribuciones de entorno cosmológico para cada simulación.

### 4.1.1 Función de Masa de los Halos

La distribución espacial de los halos refleja la fina estructura de la red cósmica formada por la materia oscura, tanto en simulaciones (ver figura 4.1) como en observaciones cosmológicas (ver sección 1.3). Esto sugiere posibles correlaciones entre las propiedades de los halos y el entorno en el cual están embebidos, tal como es mostrado para la forma de los halos, el parámetro de espín y alineación de subhalos en [25], y para la masa de los halos [24]. En especial el trabajo de [25] demuestra que el esquema de clasificación V-web es el más apropiado para estudios de correlaciones con propiedades direccionales, tal como el momento angular de los sistemas *IP* o *CLG* en la sección 4.2.



**Figure 4.1:** Distribución espacial de los halos de materia oscura, reflejando la estructura de la red cósmica. El gradiente de color indica la profundidad respecto al eje *x*, donde los halos negros son los más cercanos.

## 4.1 Propiedades de las Simulaciones

Acorde a las condiciones definitorias de las muestras *IP* y *CLG* presentadas en la subsección 3.4.2, la principal propiedad de los halos necesaria para la construcción de estas muestras es la masa. Por esta razón es importante establecer la equivalencia entre las distribuciones de masa en cada simulación. En la siguiente figura 4.2 se calculan las funciones integradas de masa para la simulación Bolshoi y para las tres simulaciones CLUES.

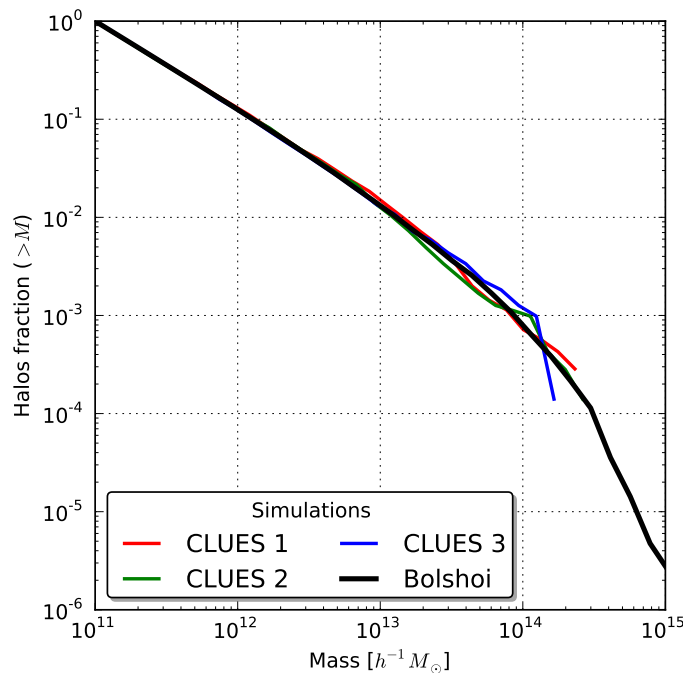


**Figure 4.2:** Funciones de masa integrada de halos de materia oscura (muestra GH) para cada simulación.

Para valores de masa altos las distribuciones son ligeramente diferentes debido a la menor cantidad de datos en las simulaciones CLUES, lo que hace menos significativa la estadística en este caso. A pesar de esto, en el rango masa donde son definidas las muestras *IH* ( $5.0 \times 10^{11} h^{-1} M_{\odot} - 5.0 \times 10^{12} h^{-1} M_{\odot}$ ) las distribuciones son consistentes con el formalismo Press-Schechter [31] para los parámetros cosmológicos WMAP7, indicando así la equivalencia de las muestras definidas entre las simulaciones.

## 4. EL ENTORNO COSMOLÓGICO Y EL GRUPO LOCAL

---

### 4.1.2 Distribución del Entorno Cosmológico

Como fue mostrado en la sección 3.3, la caracterización del entorno cosmológico se logra a partir de cantidades físicas que indiquen el carácter geométrico o dinámico local de una región de la distribución de materia. En especial el esquema V-web permite dar cuenta de la dinámica a pequeñas escalas de la estructura de la red cósmica, permitiendo definir un entorno adecuado para los halos y otros sistemas. En la siguiente figura son calculadas las distribuciones para cada uno de los autovalores de la V-web (distribuciones de entorno), tanto para las celdas de las simulaciones, como para los entornos de los halos de la muestra *GH*.

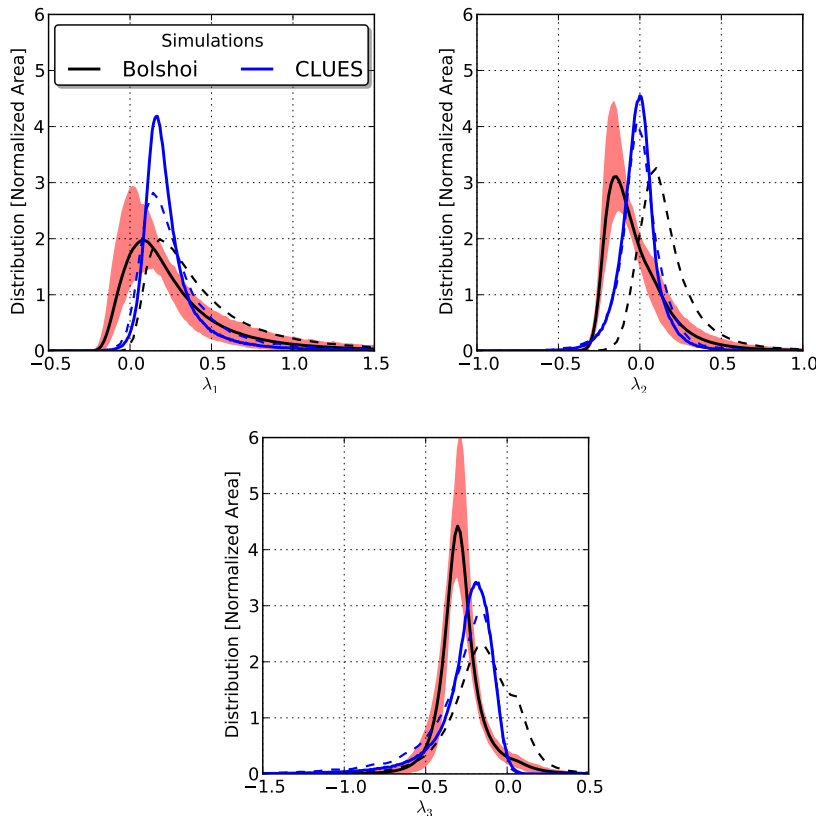


**Figure 4.3:** Distribución de los autovalores en el esquema V-web para cada una de las celdas de volumen (línea continua) y para los entornos de los halos de materia oscura en los catálogos FOF (línea discontinua). Las distribuciones están normalizadas tal que su área es la unidad. Resolución de  $1.0 h^{-1}$  Mpc/celda y suavizado Gaussiano de una celda.

## 4.1 Propiedades de las Simulaciones

---

El principal resultado de la figura 4.3 consiste en la diferencia de las distribuciones para las celdas de volumen (líneas continuas) entre la simulación Bolshoi y las simulaciones CLUES<sup>1</sup>. El efecto de varianza cósmica (regiones rojas) es incluido a partir del cálculo de distribuciones de entorno en 64 subvolúmenes de la simulación Bolshoi, con un tamaño similar a una simulación CLUES. A pesar de esto, las distribuciones de CLUES están por fuera de la región de varianza cósmica, indicando así una estructura cosmológica a gran escala que difiere entre ambas simulaciones.

Un segundo resultado importante de la figura 4.3 se obtiene a partir de las distribuciones de entorno para los halos (líneas discontinuas). En el caso de Bolshoi, se nota un importante sesgo entre la distribución de entorno de las celdas y de los halos, indicando así que la distribución espacial de los halos no es un buen trazador de la estructura a gran escala del campo de densidad. Este resultado es consistente con el trabajo de [25], donde hallan importantes sesgos en las distribuciones de entorno acorde a diferentes rangos de masa de los halos, también usando Bolshoi. En el caso de las simulaciones CLUES, las distribuciones de entorno de los halos son significativamente menos sesgadas respecto a las de celdas de volumen, indicando para este caso que los halos si se distribuyen espacialmente acorde al entorno cosmológico cuantificado por el esquema V-web.

Por último, en la figura 4.4 son calculadas las densidades medias y las fracciones de volumen para cada uno de los tipos de regiones (ver sección 3.3) acorde al valor umbral  $\lambda_{th}$ . Las funciones de fracción de volumen son diferentes entre las simulaciones CLUES y Bolshoi, en especial la región en torno a  $\lambda_{th} = 0.1$  para las regiones tipo hoja (sheet). Esto se debe al desplazamiento relativo entre los picos de las distribuciones de entorno para cada simulación (ver figura 4.3), lo que implica un comportamiento diferente al criterio de selección de regiones a partir del valor  $\lambda_{th}$ . A pesar de esto, las fracciones de volumen se mantienen más o menos consistentes para ambas simulaciones en el rango  $0.2 \leq \lambda_{th} \leq 0.4$ , que corresponde al rango donde mejor se reproduce visualmente la distribución global del campo de densidad.

---

<sup>1</sup>Debido a la alta semejanza entre las distribuciones de las tres simulaciones CLUES, y con el fin de obtener estadística más significativa, se han fusionado las distribuciones.

## 4. EL ENTORNO COSMOLÓGICO Y EL GRUPO LOCAL

---

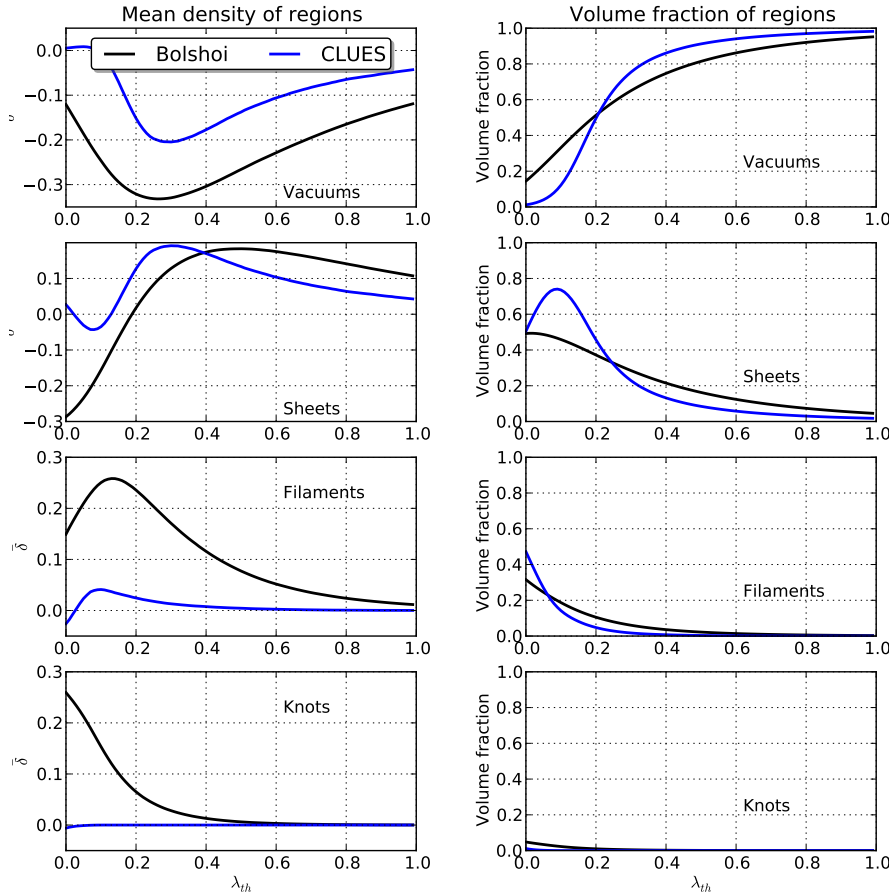


**Figure 4.4:** Parámetro de densidad medio para diferentes tipos de regiones en función del valor umbral  $\lambda_{th}$  (paneles izquierda). Fracciones de volumen normalizadas para diferentes tipos de regiones, también acorde al valor umbral  $\lambda_{th}$ .

Las gráficas de densidad media para cada tipo de región muestran importantes resultados respecto al entorno cosmológico. Lo primero que puede notarse es la diferencia entre las densidades medias de ambas simulaciones en cada una de las regiones. Por ejemplo para regiones de vacío, en Bolshoi estas corresponden a zonas con densidad promedio mucho menor a la densidad media de la simulación, mientras que para las CLUES estas zonas de subdensidad no son tan marcadas. Debido a la pequeña fracción de volumen de las regiones tipo nudo (knot) en ambas simulaciones, asociado a su dimensionalidad puntual, la estructura global del entorno puede entenderse bien solo en términos de la distribución espacial de vacíos,

## 4.1 Propiedades de las Simulaciones

hojas y filamentos, siendo los filamentos la contraparte de los vacíos respecto al parámetro de densidad. De esto se espera que la diferencia en la subdensidad de los vacíos entre cada simulación se extienda a una marcada diferencia entre las sobredensidades de los filamentos en cada simulación. Esto último es obtenido en la misma figura, donde puede verse que los filamentos de Bolshoi son notablemente más densos que aquellos de las CLUES. En el caso de las hojas, estas corresponden a regiones de densidad intermedias entre los filamentos y los vacíos, por tanto se espera que la diferencia de la densidad media de estas regiones no sea tan marcada entre ambas simulaciones, tal como se nota en la misma figura.



**Figure 4.5:** Comparación de la impresión visual obtenida con el método V-web para varios valores del parámetro  $\lambda_{th}$ . Se usa el siguiente esquema de clasificación (Negro - Nudo, Gris oscuro - Filamento, Gris - Hoja, Blanco - Vacío). La resolución de cada malla es  $1.0h^{-1}$  Mpc/celda, con un suavizado Gaussiano de una celda. El grosor de cada slide es de una celda.

## 4. EL ENTORNO COSMOLÓGICO Y EL GRUPO LOCAL

---

Un segundo resultado de la figura 4.4 consiste en la determinación de un parámetro  $\lambda_{th}$  óptimo para la reproducción visual de la red cósmica. Como se muestra en esta gráfica, las fracciones de volumen asociadas a vacíos y hojas son relativamente altas respecto a las de filamentos y nudos, esto para todo el rango barrido de valores de  $\lambda_{th}$ . De esto se espera que la impresión visual a gran escala del campo de materia sea completamente dominada por la distribución de vacíos y en menor medida por la distribución de hojas y filamentos. En el caso de un valor bajo del parámetro  $\lambda_{th}$ , por ejemplo  $\lambda_{th} < 0.2$ , el parámetro de densidad media de las hojas es negativo, indicando que posiblemente estas regiones están invadiendo zonas que deberían ser vacíos, tal como se ve en la figura 4.5 para  $\lambda_{th} = 0$  o  $\lambda_{th} = 0.1$ . En el caso de valores altos,  $\lambda_{th} > 0.4 \sim 0.5$ , el parámetro de densidad medio para los vacíos comienza a aumentar, indicando que estas regiones están invadiendo zonas que de mayor densidad, que en principio deberían ser hojas o filamentos. Esto puede ser notado en la figura 4.5 para  $\lambda_{th} = 0.5$ , donde todo el volumen es ampliamente dominado por vacíos, perdiendo la estructura característica de la red cósmica. Este análisis sugiere que el valor óptimo de  $\lambda_{th}$  podría ser aquel donde se minimice la densidad media de los vacíos, al ser estos el entorno dominante. Un resultado que apoya este criterio es que el  $\lambda_{th}$  encontrado es similar para ambas simulaciones  $\lambda_{th} \approx 0.3$ , y coincide con el valor obtenido a partir de un análisis cualitativo de la impresión visual del entorno.

Para concluir esta sección se discuten los resultados obtenidos para las distribuciones de entorno. A pesar de existir un notable sesgo entre la distribución de los halos y la del campo de densidad en la simulación Bolshoi, caso contrario a las simulaciones CLUES, y haber una marcada diferencia entre las densidades medias de las regiones en ambas simulaciones, la esencia de construir una muestra *CLG* en la simulación Bolshoi a partir de los grupos locales de las CLUES, como se menciona en el capítulo 3, es obtener una muestra de pares aislados más fiel que también reproduzcan el entorno local de los *LG*. Se espera entonces que la dinámica local cuantificada por la V-web se independiente del diferente resultado global de las distribuciones, manteniéndose así la validez del esquema de construcción de los *CLG*.

## 4.2 Propiedades de la Muestra *CLG*

Una vez determinada la consistencia entre las muestras definidas en CLUES y Bolshoi, el siguiente paso es determinar sus propiedades. Es de especial interés analizar la muestra *CLG* de Bolshoi, tomando como muestra de control la *IP* y como muestra de referencia la *LG* de las simulaciones CLUES.

### 4.2.1 Determinación del Entorno

Como fue definido en la subsección 3.4.2 del capítulo pasado, la muestra *CLG* en la simulación Bolshoi se construye imponiendo a la muestra *IP* la condición extra de reproducir el entorno cosmológico de los grupos locales de las simulaciones CLUES. La principal motivación de esto es encontrar una muestra en Bolshoi análoga a las muestras *LG*, tanto en sus propiedades físicas como en su abundancia. Respecto a esto último es natural asumir, considerando la ya determinada consistencia entre las simulaciones, que la abundancia escala aproximadamente como el volumen simulado. Esto puede ser considerado el primer logro de este esquema, ya que reproduce aproximadamente esta ley de escalamiento para el tamaño de las muestras en cuestión (ver tabla 3.2 para *CLG* de Bolshoi y *LG* de CLUES).

A pesar de lo anterior, este método de construcción no es más que corte de la muestra *IP* respecto a los autovalores de la V-web de la celda donde están embedidos, lo cual no implica la reproducción adecuada de las propiedades físicas ni el entorno cosmológico de los sistemas tipo grupo local. Por esta razón, a continuación son analizados posibles sesgos producidos en las distribuciones del entorno cosmológico para los sistemas *CLG*.



**Figure 4.6:** Situación patológica respecto al entorno de los sistemas de pares de halos.

## 4. EL ENTORNO COSMOLÓGICO Y EL GRUPO LOCAL

---

Una de las primeras consideraciones que debe tenerse en cuenta en la cuantificación del entorno para pares de halos (muestras *P*, *IP*, *CLG* y *LG*), es que cada uno de ellos puede estar embebido en celdas diferentes, tal como es mostrado en la figura 4.6. Esta situación patológica se presenta debido al carácter no puntual de este tipo de sistemas y el tamaño finito de la malla.



**Figure 4.7:** Comparación entre las distribuciones de los autovalores de la V-web para los dos halos en los sistemas de pares (muestras *LG*, *CLG* y *IP*).

Para cuantificar este efecto, en la figura 4.7 son graficadas las distribuciones de cada uno de los autovalores de la V-web para cada halo de las muestras de pares. La situación ideal, donde ambos halos comparten una misma celda, correspondería

## 4.2 Propiedades de la Muestra CLG

a un línea perfecta con pendiente de  $45^\circ$ , mientras las situaciones patológicas son responsables de dispersiones en las gráficas. Una manera de solucionar esto es disminuir la resolución de la malla tal que ambos halos estén embebidos en una misma celda, pero esto ocasiona una perdida de información del entorno local propio del sistema. Debido al suavizado Gaussiano de una celda ( $\sim 1h^{-1}$  Mpc) que es aplicado a priori a cada campo de autovalores, la variación de estos entre celdas vecinas es menor, tal como es mostrado para la mayoría de sistemas *IP* en la gráfica. Teniendo en cuenta esto último y que la dinámica local de los pares estará dominada por el halo más masivo, por convención será tomada la celda asociada a este halo para la cuantificación del entorno de todo el sistema.

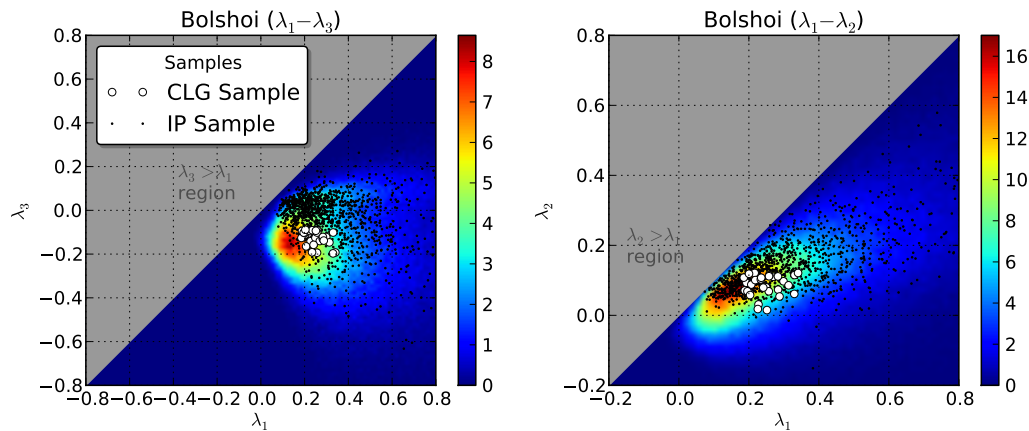


**Figure 4.8:** Distribuciones 2D del entorno cosmológico para diferentes muestras,  $\lambda_1 - \lambda_3$  (izquierda) y  $\lambda_1 - \lambda_2$  (derecha). El histograma de fondo, graficado en colores, corresponde a la distribución de entorno para todos los halos de Bolshoi (muestra *GH*), su resolución es de  $100 \times 100$  para el rango mostrado y están normalizados respecto a su área. Los puntos negros corresponden a la distribución de la muestra *IP* y finalmente los puntos blancos a la muestra *CLG*.

Una vez determinada la forma de cuantificar el entorno de los sistemas de pares, en la figura 4.8 se ilustra la distribución de las muestras *GH*, *IP* y *GCL*. Como fue mostrado en la subsección 4.1.2, la distribución de entorno de los halos en Bolshoi está considerablemente sesgada respecto a la distribución de las celdas de volumen. A pesar de esto y teniendo en cuenta que la construcción de los sistemas de pares

## 4. EL ENTORNO COSMOLÓGICO Y EL GRUPO LOCAL

---

se hace a partir de los halos, es más interesante realizar comparaciones con las distribuciones asociadas a los halos (histogramas de color en la misma figura). Como fue definido en la subsección 3.4.2, la muestra *IP* es construida de tal forma que se garantice su aislamiento gravitacional respecto a halos más masivos, por esta razón hay dos efectos que compiten en cuanto a la distribución de entorno de estos sistemas. En el primero se espera que la abundancia de pares sea más favorable en entornos donde la cantidad de halos es mayor, mientras en el segundo, precisamente la sobreabundancia de halos resulta desfavorable para los criterios de aislamiento gravitacional. El segundo efecto termina siendo dominante y produce un sesgo en la distribución de entorno de la muestra *IP* respecto a la de los halos, mientras que para en la muestra *P* el sesgo no se presenta<sup>1</sup>.

Para terminar el análisis de la anterior figura, se discute acerca de la distribución de entorno para los *CLG* de la simulación Bolshoi. A pesar de que esta distribución es construida de forma artificial por efecto de selección, es interesante notar que la región en el espacio de autovalores que delimita esta muestra es relativamente reducida, indicando que los tres grupos locales de las simulaciones CLUES comparten una dinámica de entorno local muy similar. Aunque esto último puede ser un efecto impuesto a priori por construcción debido al carácter restringido de las simulaciones CLUES, no deja de ser interesante el sesgo que esta característica produce en la distribución de entorno de los *CLG* respecto a los halos y a la muestra *IP*.

Para cuantificar los sesgos producidos en cada muestra respecto a un tipo de entorno específico (ver figura 3.9), en la siguiente figura 4.9 se grafican las fracciones de objetos en las diferentes regiones. En el rango óptimo del valor umbral  $0.2 \leq \lambda_{th} \leq 0.4$  definido en la subsección 4.1.2, se notan importantes diferencias entre cada una de las muestras, especialmente para la *CLG*. Como fue mencionado anteriormente, el efecto de aislamiento gravitacional produce un sesgo entre la distribución de entorno de los halos *GH* y de los sistemas *IP*, esto puede ser claramente notado para cada una de las fracciones en el rango óptimo de  $\lambda_{th}$ . En el caso de vacíos, la fracción dominante de estas dos muestras es la asociada a *IP*, pero en el caso de hojas ambas son comparables, y más aún, en la regiones tipo filamento y nudo domina la fracción de halos *GH*. Esto indica que los sistemas de pares aislados *IP* se presentan con mayor abundancia en regiones de media o baja densidad de

---

<sup>1</sup>Esto último no es mostrado en la figura 4.8, pero es fácilmente calculado.

## 4.2 Propiedades de la Muestra *CLG*

halos, aún así la considerable fracción de estos presentes en hojas y filamentos no permite asociar un tipo de región de entorno específica para estos sistemas. Finalmente, los sistemas *CLG* presentan un importante sesgo en comparación a las dos muestras anteriores, siendo de especial interés aquella producida respecto a la *IP* debido a que *CLG* es una submuestra de esta. De nuevo, apelando al rango óptimo de  $\lambda_{th}$ , es posible en este caso asociar tipos de regiones de entorno específicas a la muestra *CLG*, estando estos sistemas preferencialmente en hojas y vacíos.



**Figure 4.9:** Fracciones de cantidad de objetos en diferentes regiones en función del valor umbral  $\lambda_{th}$ . Para el caso de la muestra *GH* se cuentan número de Halos, mientras que para las muestras *IP* y *CLG* número de pares.

A pesar del esquema de clasificación de regiones usado, las conclusiones anteriores dependen de la elección del parámetro  $\lambda_{th}$ , que aunque ha sido razonablemente acotado en una región óptima que reproduce la impresión visual, no deja de ser un parámetro libre. Para solventar esto se introduce el fraccional de anisotropía (FA) con la normalización usada en [25]

## 4. EL ENTORNO COSMOLÓGICO Y EL GRUPO LOCAL

---

$$FA = \frac{1}{\sqrt{3}} \sqrt{\frac{(\lambda_1 - \lambda_3)^2 + (\lambda_2 - \lambda_3)^2 + (\lambda_1 - \lambda_2)^2}{\lambda_1^2 + \lambda_2^2 + \lambda_3^2}} \quad (4.1)$$

Esta cantidad cuantifica el grado de anisotropía del entorno cosmológico local, siendo  $FA = 1$  una región altamente anisotrópica, mientras  $FA = 0$  un régión con alta isotropía, además es independiente de la elección a priori de algún parámetro libre. Acorde al resultado obtenido por [25], regiones de baja anisotropía corresponden a nudos debido a su colapso isotrópico, mientras que regiones de alta anisotropía corresponden a vacíos debido a su expansión no uniforme. Para regiones filamentales y planas el fraccional de anisotropía está distribuido de forma extendida en valores intermedios, indicando que la dinámica de este tipo de entornos es más compleja. Aún así, hay una tendencia a valores bajos en el caso de filamentos y valores altos para hojas.

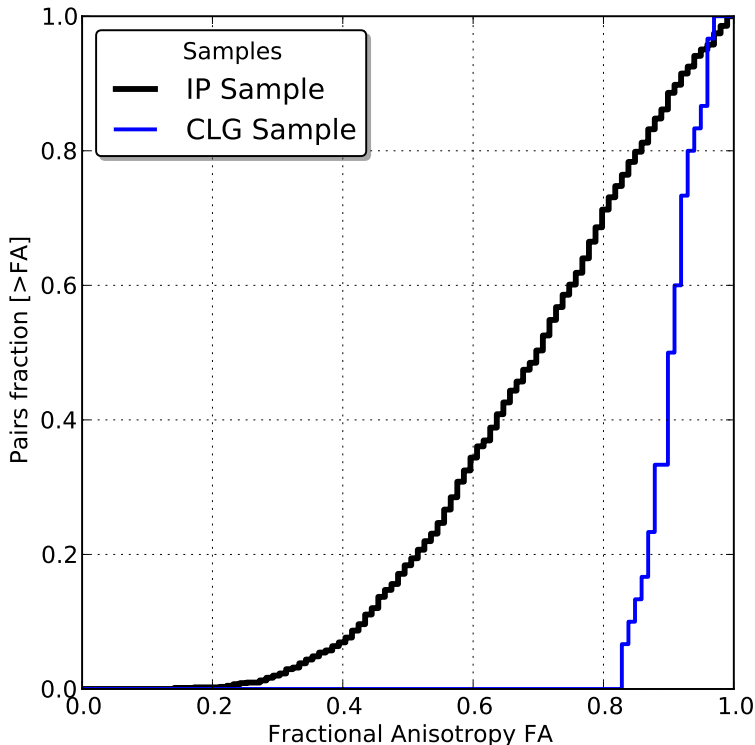


**Figure 4.10:** Histograma integrado del fraccional de anisotropía para las muestras de pares *IP* y *CLG*.

## 4.2 Propiedades de la Muestra *CLG*

---

En la figura 4.10 son calculados los histogramas integrados del fraccional de anisotropía para las muestras *IP* y *CLG*. El primer resultado está asociado a la distribución de los *IP*, la cual es altamente homogénea para rangos intermedios (aproximadamente  $0.4 < FA < 0.9$ ) como es evidenciado en la pendiente constante del histograma. Esto implica que los sistemas *IP* están distribuidos en zonas de media a alta anisotropía, en concordancia con las fracciones encontradas en regiones de vacío, hojas y filamentos. El segundo resultado es el sesgo obtenido en la distribución de FA de la muestra *CLG*. A diferencia de los *IP*, esta distribución se encuentra concentrada en regiones de alta anisotropía (aproximadamente  $0.8 < FA < 1.0$ ), lo que confirma finalmente que es posible asociar un tipo de entorno cosmológico a los sistemas *CLG* y el cual esta acorde con regiones vacías y planas, o en términos de las direcciones definidas en la V-web, regiones que se expanden en dos direcciones (asociadas a los autovalores  $\lambda_2$  y  $\lambda_3$ ), mientras que poseen un ligero colapso/expansión en la tercera dirección (asociada al autovalor  $\lambda_1$ ).

La principal ventaja de usar el fraccional de anisotropía radica en que esta cuantifica en un solo valor la dinámica del entorno cosmológico, permitiendo establecer un marco de estudio más natural y directo para correlaciones de entorno con cantidades físicas.

### 4.2.2 Masa de los *CLG*

Como fue demostrado en la subsección 4.1.1, la distribución de masa de los halos es consistente entre las diferentes simulaciones, por tanto se espera que todas las muestras, a excepción de *CLG* que requiere además del entorno cosmológico, sean también consistentes entre las simulaciones. Para el estudio de las masas de los sistemas de pares se propone el uso de dos cantidades, la primera es la masa total del sistema  $M_{tot} = M_A + M_B$  y la segunda es la relación de las masas  $\chi = M_B/M_A$ , donde por convención  $M_A$  es el halo más masivo.

En la siguiente figura 4.11 se calculan los histogramas integrados para la masa total y la razón de las masas. Se toma la muestra *IP* como muestra de control, además se muestran los valores obtenidos para cada uno de los grupos locales en CLUES.

## 4. EL ENTORNO COSMOLÓGICO Y EL GRUPO LOCAL

---

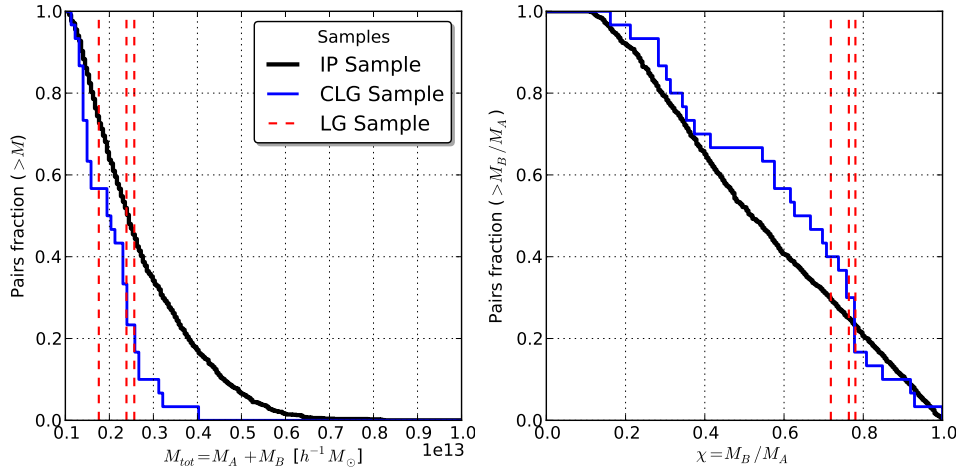


**Figure 4.11:** Funciones de distribución integrada para la masa total  $M_A + M_B$  (izquierda) y la razón de las masas  $M_B/M_A$  (derecha), de las muestras de pares en Bolshoi.

Una característica interesante de esta figura consiste en los rangos bien definidos asociados a la muestra *LG* de CLUES (líneas rojas verticales). Esto evidencia que los grupos locales *LG* no solo comparten una entorno cosmológico común sino también una distribución de masa local. Como posible explicación a esto puede considerarse un efecto de selección de las muestras en la construcción de las simulaciones restringidas, mientras que una alternativa optimista sería tomarlo como una evidencia de la correlación entre la distribución de masa y el entorno local.

Para responder la anterior cuestión se debe analizar la distribución de los parámetros de masa para las demás muestras. En el caso de la masa total de los *IP*, esta se encuentra distribuida acorde a la distribución de masa de los halos (ver figura 4.2), tal como es esperado al no existir ninguna restricción respecto al entorno y en el caso de la razón de masas, se obtiene una distribución completamente homogénea. Ahora, para la muestra *CLG*, la cual se espera que sea influenciada por los efectos del entorno, se obtiene una distribución de masa total sesgada respecto a la de *IP* y centrada aproximadamente en el rango definido por los *LG*. Para la distribución de la razón de masas de *CLG* también se encuentra un comportamiento uniforme teniendo en cuenta la escasez de datos, a pesar de esto hay una aparente sobreabundancia en torno al valor medio definido por los *LG*, pero nuevamente no hay suficientes datos para concluir una posible relación.

## 4.2 Propiedades de la Muestra CLG

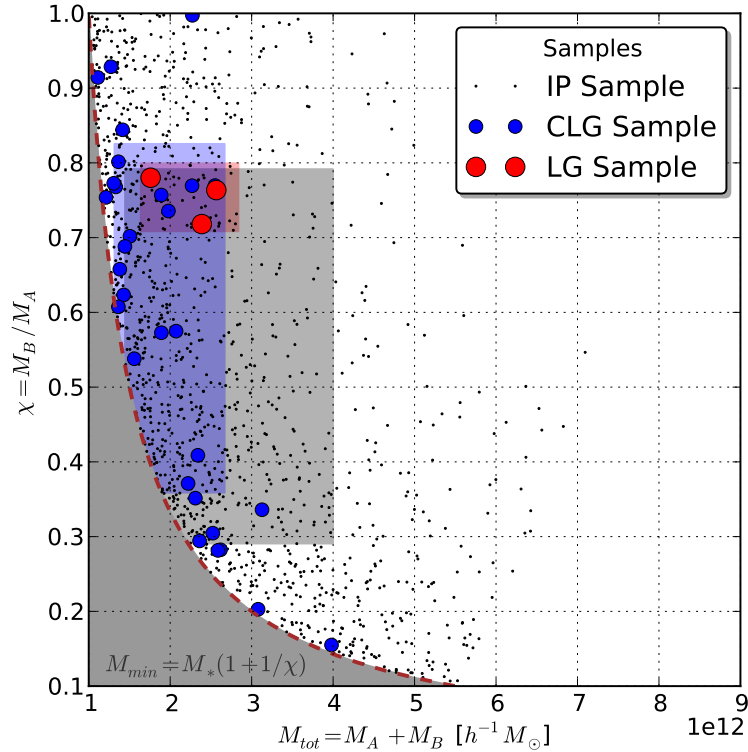


**Figure 4.12:** Diagrama de dispersión de los parámetros de masa definidos ( $M_{tot}, \chi$ ) para cada una de las muestras de pares. Las regiones cuadradas son construidas a partir del valor medio y la desviación estándar de la muestra del mismo color. La región gris en la parte inferior izquierda corresponde a un corte impuesto artificialmente con el rango mínimo de masa de los halos tomados  $M_*$  para construir las muestras de pares.

En la figura 4.12 se muestra un diagrama de dispersión para los parámetros de masa de las muestras de pares. Las regiones cuadradas representan el valor medio más o menos una desviación estándar para los parámetros marcados en cada eje, lo que permite comparar gráficamente las distribuciones. De esta comparación se confirma que el criterio de construcción de la muestra *CLG* selecciona masas de pares  $M_{tot}$  consistente con las masa de los *LG* en las simulaciones restringidas, mientras que no hace ninguna selección respecto a la razón de masas  $\chi$ .

Finalmente, con el objetivo de responder si existe un posible efecto de entorno en la selección de la masa total obtenida para la muestra *CLG*, se calcula en la siguiente figura 4.13 diagramas de correlación entre el fraccional de anisotropía y los parámetros de masa.

## 4. EL ENTORNO COSMOLÓGICO Y EL GRUPO LOCAL

---

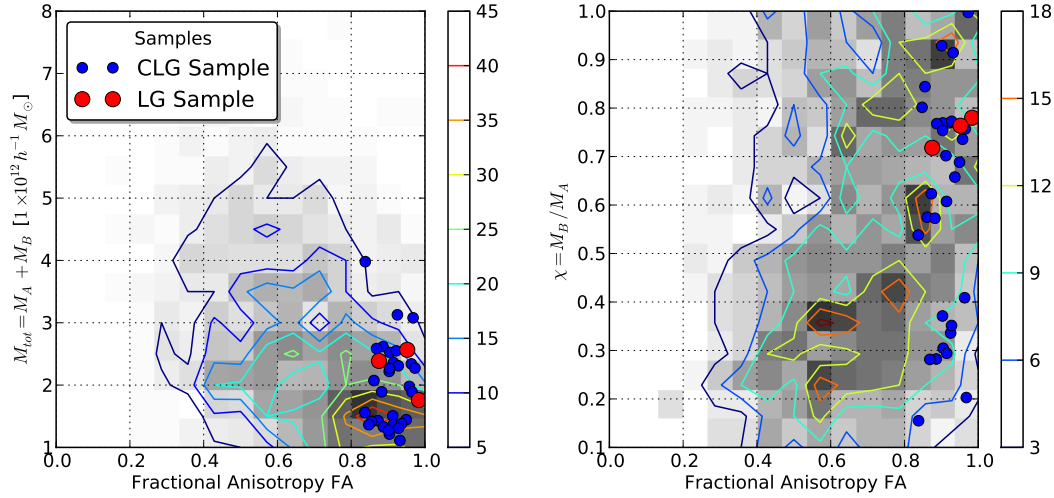


**Figure 4.13:** Diagramas de dispersión para el fraccional de anisotropía respecto a los parámetros de masa. El mapa de fondo y las curvas de contorno corresponden a número de pares de la muestra *IP*.

En el caso de la masa total  $M_{tot}$  de la muestra *IP*, puede notarse que pares con bajos valores de masa están preferencialmente en regiones de alta anisotropía, mientras que pares de masa más alta en regiones de anisotropía intermedia. Esto puede ser considerado como una correlación de entorno para la muestra *IP* respecto a la masa total, de lo cual se concluye que el criterio de selección de la muestra *CLG* a partir del entorno de los *LG* hace un corte para pares de baja masa.

Para la razón de las masas  $\chi$  se nota una distribución más dispersa para la muestra *IP*, a pesar de esto se nota una sobreabundancia de pares con valores de  $\chi$  bajos en zonas de anisotropía media, mientras que en regiones de alta anisotropía se presentan valores más altos de  $\chi$ . Esto es consistente con la selección realizada en la muestra *CLG*, para la cual aproximadamente el 66% de los pares tienen un valor  $\chi > 0.5$ . De esto puede intuirse una posible correlación entre el entorno y el valor  $\chi$  de los pares, aún así, debido a la alta dispersión de la distribución y la poca cantidad de datos, no puede concluirse nada al respecto.

### 4.2.3 Distribuciones de Energía y Momentum Angular

La energía y el momentum angular constituyen otras propiedades físicas de interés para los sistemas de pares, estas son definidas acá a partir de las siguiente expresiones

$$e_{tot} = \frac{1}{M_A + M_B} \left[ \frac{1}{2} (M_A v_A'^2 + M_B v_B'^2) - G \frac{M_A M_B}{|\mathbf{r}_A' - \mathbf{r}_B'|} \right] \quad (4.2)$$

$$\mathbf{L}_{orb} = \frac{1}{M_A + M_B} [M_A \mathbf{r}_A' \times \mathbf{v}_A' + M_B \mathbf{r}_B' \times \mathbf{v}_B'] \quad (4.3)$$

donde  $\mathbf{r}_i'$  es la posición comóvil del halo  $i$  y  $\mathbf{v}_i'$  es la velocidad total<sup>1</sup> respecto al centro de masa del par.



**Figure 4.14:** Diagrama de dispersión para la energía total y el momentum angular orbital de los sistemas de pares. El mapa de fondo corresponde a la distribución de la muestra  $P$ , mientras las líneas de contorno a la distribución de la muestra  $IP$ , en ambos casos los valores corresponden al número de pares.

<sup>1</sup>Velocidad total debido a que se incluye la velocidad peculiar y el flujo de Hubble respecto al centro de masa del sistema, así  $\mathbf{v}_i' = \mathbf{v}_{pec,i} + H_0 \mathbf{r}_i'$ .

## 4. EL ENTORNO COSMOLÓGICO Y EL GRUPO LOCAL

---

En la figura 4.14 se muestran las distribuciones de energía total específica y momentum angular orbital específico para las diferentes muestras. Lo primero que puede ser notado es un significativo sesgo entre la distribución de los *IP* respecto a los *P*, lo que demuestra que el criterio de aislamiento gravitacional definido en la subsección 3.4.2 selecciona un rango de energía y momentum angular más bajo que en los pares generales, siendo así estos sistemas gravitacionalmente más ligados. En el caso de la muestra *CLG*, su distribución parece seguir la de los *IP*, no habiendo así una aparente selección por la condición entorno. Por último, es interesante observar nuevamente que las propiedades asociadas a la muestra *LG* poseen valores muy cercanos, indicando así que representan un tipo de sistema bien definido, aunque como ha sido mencionado, esto puede ser efecto de selección en la construcción de CLUES.

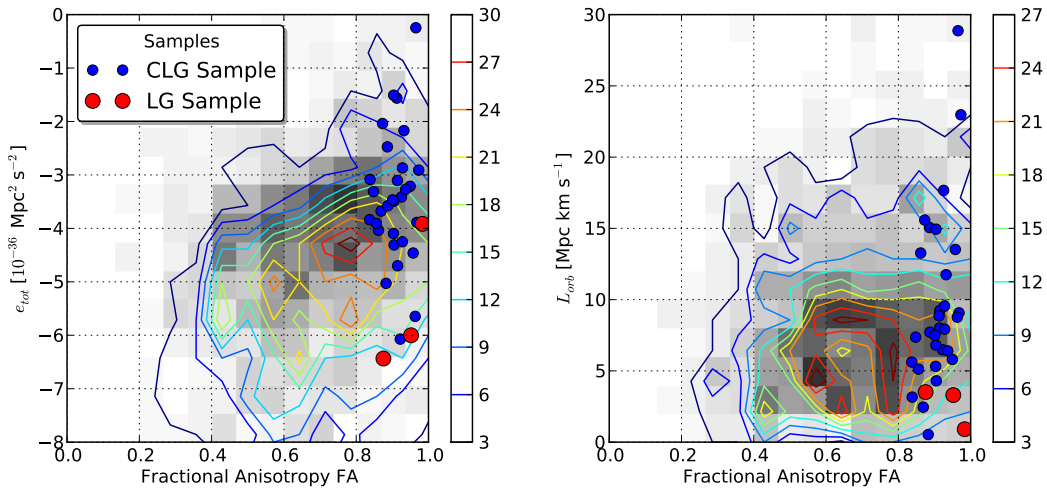


**Figure 4.15:** Diagramas de dispersión para el fraccional de anisotropía respecto a la energía y el momentum angular. El mapa de fondo y las curvas de contorno corresponden a número de pares de la muestra *IP*.

En la figura 4.15 se calculan diagramas de correlación de la energía y el momentum angular con el fraccional de anisotropía con el objetivo de determinar posibles correlaciones. En el caso de la energía específica, sistemas de pares *IP* con mayor energía (menos ligados) parecen estar mayoritariamente en zonas de alta anisotropía, mientras que sistemas de menor energía (más ligados) están en zonas

## 4.2 Propiedades de la Muestra CLG

de anisotropía media, lo que muestra una correlación entre estas dos cantidades. Para sistemas *CLG*, la selección a partir del entorno parece sesgar su distribución de energía a valores más altos que la distribución media de los *IP*, lo que es consistente con la correlación encontrada. En este caso, los sistemas *LG* parecen no seguir esta correlación, teniendo valores mucho más bajos de energía que lo esperado. Finalmente, para la distribución de momentum angular específico no existe ninguna correlación clara, siendo cualquier valor  $L_{orb}$  de los pares igualmente probable en el espectro de posibles entornos para estos sistemas.

### 4.2.4 Alineación del Momentum Angular

Finalmente la última propiedad analizada para los sistemas de pares es su alineación respecto al entorno cosmológico, para esto se define el ángulo  $\phi_i$  como el formado entre el autovector  $\mathbf{u}_{\lambda i}$  de la V-web y el momentum angular del par  $\mathbf{L}_{orb}$ .



**Figure 4.16:** Histogramas integrados para el ángulo formado entre el momentum angular de los pares, el cual determina el plano orbital, y cada uno de los autovectores definidos por la V-web en el entorno cosmológico. Se realiza para cada las muestras de pares *CLG* y *IP*, mientras que los grupos locales de CLUES son ilustrados con las líneas rojas punteadas.

En la figura 4.16 se calculan los histogramas integrados para cada uno de los angulos  $\phi_i$  definidos. Como puede notarse, las muestras *CLG* y *IP* son homogéneas respecto a los tres valores, indicando que no hay una alineación preferida respecto al entorno cosmológico. Esto también se evidencia en los valores calculados de los *LG* de las simulaciones restringidas.

## 4. EL ENTORNO COSMOLÓGICO Y EL GRUPO LOCAL

---

### 4.3 Conclusiones

Esta sección está dedicada a compilar los principales resultados obtenidos en este capítulo. Estos serán enumerados y discutidos acorde al órden en que fueron obtenidos.

1. La construcción de la muestra *IP* fue inicialmente propuesta en [8] con el objetivo de reproducir sistemas tipo grupo local. A pesar de esto, el número de estos sistemas encontrados en la simulación Bolshoi es mucho mayor al que se espera acorde a la abundancia de *LG* en simulaciones restringidas. El método propuesto para la selección de la muestra *CLG* en Bolshoi a partir del entorno cosmológico de los *LG*, produce un número de sistemas que concuerda con los encontrados en las simulaciones restringidas, escalando aproximadamente como el volumen de las simulaciones. Más aún, aplicando este mismo método en las simulaciones restringidas se halla una muestra con un tamaño similar a la *LG*.
2. A partir de los valores medios de densidad en las diferentes regiones del entorno cosmológico (figura 4.4) se propone un esquema para la elección de un rango óptimo del parámetro  $\lambda_{th}$  de la V-web con el objetivo de reproducir la apariencia visual de la red cósmica. Este está basado en la minimización de la densidad media en las regiones de vacío debido a que son las dominan la apariencia del campo de densidad a gran escala. Con esto se garantiza que las regiones vacías no invadan regiones de más alta densidad, que en principio deben ser clasificadas como hojas o filamentos. Este método da un rango de valores óptimos aproximadamente igual para todas las simulaciones usadas ( $0.2 \leq \lambda_{th} \leq 0.4$ ), además reproduce adecuadamente la apariencia visual (ver figura 4.5 para  $\lambda_{th} = 0.3$ ). A pesar de esto, este parámetro sigue siendo libre y no es viable usar un esquema de clasificación basado en este para determinar correlaciones con propiedades físicas, en vez de esto se introduce el fraccional de anisotropía con la normalización usada en [25].
3. La distribución del entorno cosmológico de las simulaciones Bolshoi y CLUES difieren, existiendo un cambio de densidad media muy pronunciado entre regiones de vacío y filamentos en Bolshoi, mientras que es mucho más suave

### **4.3 Conclusiones**

---

en las CLUES. A pesar de esto, las fracciones de volumen asociadas a cada tipo de entorno son aproximadamente iguales para ambas simulaciones en el rango óptimo determinado para  $\lambda_{th}$ . A pesar de esto, se espera que la dinámica local caracterizada por la V-web sea independiente de la estructura global de la distribución de entorno, lo cual valida el esquema de selección de la muestras *CLG* en Bolshoi.

4. El método de construcción de los *CLG* selecciona un entorno cosmológico común para estos sistemas, siendo preferidas zonas de vacío y hojas no muy planas. Estas regiones presentan una alta anisotropía, cuantificada por el fraccional de anisotropía FA. En el caso de los sistemas *IP*, estos se encuentran en zonas de media a alta anisotropía, asociadas a valores de baja densidad, contrario a los halos que están en zonas más densas y menos anisotrópicas como filamentos y nudos, aún así la distribución de entorno de los *IP* es amplia y no pueden ser asociados a un tipo de entorno específico. El sesgo producido entre los *IP* y los halos generales se debe al criterio de aislamiento gravitacional usado para construir los *IP*, esto hace que zonas con mayor densidad de halos sean menos aptas por la alta influencia gravitacional.
5. Se encuentra una correlación entre la masa total de los pares de la muestra *IP* y el fraccional de anisotropía del entorno, donde masas mayores son más abundantes en regiones de anisotropía media mientras masas menores se presentan con mayor frecuencia en zonas de alta anisotropía. Esto implica que la selección de entorno realizada en los *CLG* reproduce un rango de masa menor. En el caso de la razón de masa, no se encuentra ninguna correlación significativa con el entorno, aún así se nota una ligera sobreabundancia de razones de masa mayores en regiones más anisotrópicas, pero es necesaria más estadística para poder ser algo concluyente.
6. Se halla un correlación para la energía específica de los sistemas *IP* respecto al entorno, obteniendo valores más altos en regiones más anisotrópicas y valores bajos en regiones de anisotropía media. Esta correlación parece seleccionar un rango de energía para los sistemas *CLG*, aunque esta no es consis-

#### **4. EL ENTORNO COSMOLÓGICO Y EL GRUPO LOCAL**

---

tente con los valores obtenidos de los *LG*. Para el momentum angular no se encuentra ninguna correlación con el entorno.

7. Finalmente se encuentra que no existen alineaciones privilegiadas entre el momentum angular de los pares *CLG* (o de su plano orbital) y las direcciones de los autovectores de la V-web.

# Bibliography

- [1] A.W. Appel. *Undergraduate Thesis, Princeton University*. SIAM J. Sci. Stat. Comput. 6, 85, 1985. 48
- [2] J. Barnes and P. Hut. A hierarchical  $o(n \log n)$  force-calculation algorithm. *Nature*, 324:446–449, 1986. 48
- [3] J. Binney and S. Tremaine. *Galactic Dynamics*. Princeton University Press, USA, second edition, 2008. ISBN 978-0-691-13027-9. 42
- [4] H. Curtis. The scale of the universe. *Bull. Nat. Res. Coun*, 2:171, 1921. 3
- [5] J.M. Dawson. Particle simulation of plasmas. *Reviews of Modern Physics*, 55:403–447, 1983. 44
- [6] A. Einstein. Grundlage der allgemeinen relativitätstheorie. *Annalen der Physik*, 49(4):769–822, 1916. 3
- [7] J. Forero-Romero, Y. Hoffman, S. Gottlöber, A. Klypin, and G. Yepes. A dynamical classification of the cosmic web. *Mon.Not.Roy.Astron.Soc*, 396: 1815–1824, 2009. 56
- [8] J. Forero-Romero, Y. Hoffman, G. Yepes, S. Gottlöber, R. Piontek, A. Klypin, and M. Steinmetz. The dark matter assembly of the local group in constrained cosmological simulations of a lambda cold dark matter universe. *Mon.Not.Roy.Astron.Soc*, 417:1434–1443, 2011. 60, 61, 86

## BIBLIOGRAPHY

---

- [9] J.E. Forero-Romero, Y. Hoffman, S. Bustamante, S. Gottlöber, and G. Yepes. The kinematics of the local group in a cosmological context. *Accepted to publication in ApJ Letters*, 2013. 8, 61
- [10] A. Friedman. On the curvature of space. *General Relativity and Gravitation*, 31:1991, 1999. 4
- [11] A. Friedman. On the possibility of a world wih constant negative curvature of space. *General Relativity and Gravitation*, 31:2009, 1999. 4
- [12] S. Gottlöber, Y. Hoffman, and G. Yepes. Constrained local universe simulations (clues). *Proceedings of High Performance Computing in Science and Engineering*, pages 309–322, 2010. 53
- [13] O. Hahn, C. Porciani, M. Carollo, and A. Dekel. Properties of dark matter haloes in clusters, filaments, sheets and voids. *Mon.Not.Roy.Astron.Soc*, 375: 489–499, 2007. 54
- [14] W. Herschel. On the construction of the heavens. *Philosophical Transactions of the Royal Society of London*, 75(I):213–266, 1785. viii, 2
- [15] R.W. Hockney and J.W. Eastwood. *Computer Simulation Using Particles*. IOP Publishing Ltd, Great Britain, first edition, 1988. ISBN 0-85274-392-0. 46
- [16] Y. Hoffman and E. Ribak. Constrained realizations of gaussian fields: A simple algorithm. *ApJ*, 380:L5–L8, 1991. 52
- [17] Y. Hoffman, O. Metuki, G. Yepes, G. Gottlöber, J. Forero-Romero, N. Libeskind, and A. Knebe. A kinematical classification of the cosmic web. *Mon.Not.Roy.Astron.Soc*, 425:2049–2057, 2012. 56
- [18] E.P. Hubble. Extragalactic nebulae. *ApJ*, 64:321–369, 1926. 3
- [19] J.D. Jackson. *Classical Electrodynamics*. John Wiley & Sons, Inc., USA, third edition, 1999. ISBN 0-471-30932-X. 28

---

## BIBLIOGRAPHY

- [20] N. Jarosik et al. Seven-year wilkinson microwave anisotropy probe (wmap) observations: Sky maps, systematic errors, and basic results. *ApJS*, 192:14, 2011. 10, 21
- [21] J.G. Jernigan. Dynamic of star clusters. *IAU Symposium 113*, page 131, 1985. 48
- [22] A. Klypin, Y. Hoffman, A. Kravtsov, and S. Gottlöber. Constrained simulations of the real universe: the local supercluster. *ApJ*, 596:19–33, 2003. ix, 51, 52
- [23] A.A. Klypin, S. Trujillo-Gomez, and J. Primack. Dark matter halos in the standard cosmological model: Results from the bolshoi simulation. *ApJ*, 740:102, 2011. 50
- [24] G. Lemson and G. Kauffmann. Environmental influences on dark matter halos and consequences for the galaxies within them. *Mon.Not.Roy.Astron.Soc*, 302:111, 1999. 66
- [25] N. Libeskind, Y. Hoffman, J. Forero-Romero, S. Gottlöber, A. Knebe, M. Steinmetz, and A. Klypin. The velocity shear tensor: tracer of halo alignment. *Mon.Not.Roy.Astron.Soc*, 428:2489–2499, 2013. 66, 69, 77, 78, 86
- [26] M.S. Longair. *Galaxy Formation*. Springer, New York, second edition, 2008. ISBN 978-3-540-73477-2. viii, 2, 3, 13, 15, 17, 18, 19, 21, 24, 26, 36, 39
- [27] T. Padmanabhan. *Structure Formation in the Universe*. Cambridge University Press, Great Britain, first edition, 1995. ISBN 0-521-42486-0. 13, 19, 20, 23, 32, 34, 39, 43
- [28] R.K. Pathria. *Statistical Mechanics*. Butterworth-Heinemann, Great Britain, second edition, 1996. ISBN 0-7506-2409-8. 28
- [29] S. Pfalzner and P. Gibbon. *Many-Body Tree Methods in Physics*. Cambridge University Press, USA, first edition, 1996. ISBN 0-521-49564-4. 42, 45, 48
- [30] D. Porter. *PhD Thesis*. University of California, Berkeley, 1985. 48

## BIBLIOGRAPHY

---

- [31] W. Press and P. Schechter. Formation of galaxies and clusters of galaxies by self-similar gravitational condensation. *ApJ*, 187:425–438, 1974. 67
- [32] H. Shapley. The scale of the universe. *Bull. Nat. Res. Coun*, 2:164, 1921. 3
- [33] S. Weinberg. *Gravitation and Cosmology: Principles and Applications of the General Theory of Relativity*. John Wiley & Sons, Inc., New York, first edition, 1972. ISBN 0-471-92567-5. 14, 16
- [34] A. Yoshisato, M. Morikawa, N. Gouda, and H. Mouri. Why is the zel'dovich approximation so accurate? *ApJ*, 637:555–560, 2006. 38
- [35] S. Zaroubi, Y. Hoffman, and A. Dekel. Wiener reconstruction of large-scale structure from peculiar velocities. *ApJ*, 520:413–425, 1999. 52
- [36] Y.B. Zeldovich. Gravitational instability: an approximate theory for large density perturbations. *Astronomy and Astrophysics*, 5:84–89, 1970. 38